JOURNAL OF MATERIALS SCIENCE 22 (1987) 3041–3086

Review
Relationships between processing, microstructure and properties of dense and reaction-bonded silicon nitride

G. ZIEGLER, J. HEINRICH*, G. WÖTTING,
Deutsche Forschungs- und Versuchsanstalt für Luft- und Raumfahrt, Institut für Werkstoff-Forschung, Postfach 90 60 58, D-5000 Köln 90, FRG

Some aspects of processing, microstructure and properties of the various types of silicon nitride are discussed. Special emphasis is placed on the relationships between powder properties, process conditions, densification and microstructure, as well as the interdependence between microstructure and properties. After summarizing the areas of crystal structure and thermodynamic properties, and processing of the different types of Si_3N_4, the state-of-the-art of dense and reaction-bonded silicon nitride is given. For both types the formation mechanisms and microstructure, relationships between powder properties, additives (in the case of dense Si_3N_4), process conditions, and densification and microstructure, as well as data and microstructural effects of various mechanical, thermal and thermo-mechanical properties, are outlined. Advanced processing techniques, such as sintering, gas-pressure sintering, post-sintering, and the different routes of hot-isostatic pressing (starting with powder compacts, reaction-bonded Si_3N_4 or pre-sintered Si_3N_4), and the resulting properties, are discussed.

1. Introduction

During recent years, significant progress has been made in the development of engineering ceramic materials. A new generation of ceramics has been developed which are expected to find wide use in structural applications at high temperatures. Because of the good combination of mechanical, thermal and thermo-mechanical properties, silicon nitride (Si_3N_4) is one of the most promising materials in this class (see Table I). In particular, Si_3N_4 has high strength at high temperatures, good thermal stress resistance due to the low coefficient of thermal expansion, and relatively good resistance to oxidation compared to other high-temperature structural materials. This combination of properties can be used to increase operating temperatures. Moreover, the low density of Si_3N_4 of $3.2\,g\,cm^{-3}$ (about 40% of the density of high-temperature superalloys) may offer components of lower weight and therefore is sometimes an important advantage over other high-temperature materials. Potential applications of Si_3N_4 which may be cited are the all-ceramic gas turbine or in the replacement of metallic components in internal combustion engines. Moreover, other engineering applications are also under consideration, such as energy conversion systems, industrial heat exchangers, as wear-resistant material in metals processing and as material for ball and roller bearings [1–4].

During the last 10 years, the technological know-how in the area of Si_3N_4 has been greatly developed, particularly because of its planned application in the vehicle gas turbine. Technological investigations have mainly been concentrated during this time on two types of Si_3N_4: (i) dense Si_3N_4, which can be produced by hot-pressing, sintering or hot-isostatic pressing, and (ii) porous Si_3N_4 produced by reaction-bonding of silicon powder compacts. As a consequence of processing, the two forms of Si_3N_4 are different in density, both in pore and grain structure, and in resulting mechanical, thermal and thermo-mechanical properties [4–14].

After summarizing the state-of-the-art briefly, some aspects of processing, microstructure and properties of the various types of Si_3N_4 are discussed. Emphasis is especially placed on the relationships between powder properties, processing conditions, densification and microstructure as well as the interdependence between microstructure and properties. Here it should be mentioned that in this review literature had to be selected from the large number of publications on the subject. For more literature, the reader is referred to the original papers cited in this contribution, and to the bibliography of Messier on Si_3N_4 [15].

2. Crystal structure and thermodynamic properties of silicon nitride

2.1. Crystal structure

Silicon nitride crystallizes in the two hexagonal modifications α and β [16] which differ in that the lattice

*Present address: Hoechst Ceram TecAG, Wilhelmstrasse 14, D-8672 Selb, FRG.

0022–2461/87 $03.00 + .12

TABLE I Properties of silicon nitride ceramics

Crystal structure:	
α-phase, hexagonal	*a*-axis 0.775–0.777 nm *c*-axis 0.516–0.569 nm $c/a \sim 0.70$
β-phase, hexagonal	*a*-axis 0.759–0.761 nm *c*-axis 0.271–0.292 nm $c/a \sim 0.37$
Decomposition temperature (°C)	1900
Theoretical density ($g\,cm^{-3}$):	
α-phase	3.168–3.188
β-phase	3.19–3.202
Density ($g\,cm^{-3}$):	
dense Si_3N_4	90–100% th.d.*
reaction-bonded Si_3N_4	70–88% th.d.
Coefficient of thermal expansion (20–1500° C) ($10^{-6}\,°C^{-1}$)	2.9–3.6
Thermal conductivity (RT) ($W\,m^{-1}\,K^{-1}$):	
dense Si_3N_4	15–50
reaction-bonded Si_3N_4	4–30
Thermal diffusivity (RT) ($cm^2\,sec^{-1}$):	
dense Si_3N_4	0.08–0.29
reaction-bonded Si_3N_4	0.02–0.22
Specific heat ($J\,kg^{-1}\,°C^{-1}$)	700
Electrical resistivity (RT) (Ωcm)	$\sim 10^{13}$
Microhardness (Vickers, $MN\,m^{-2}$)	1600–2200
Young's modulus, (RT) ($GN\,m^{-2}$):	
dense Si_3N_4	300–330
reaction-bonded Si_3N_4	120–220
Flexural strength (RT) ($MN\,m^{-2}$):	
dense Si_3N_4	400–950
reaction-bonded Si_3N_4	150–350
Fracture toughness ($MN\,m^{-3/2}$):	
dense Si_3N_4	3.4–8.2
reaction-bonded Si_3N_4	1.5–2.8
Thermal stress resistance parameter $R = \sigma_F(1-\nu)/\alpha E$ (°C) and $R' = R\lambda$ ($10^3\,W\,m^{-1}$):	
dense Si_3N_4	R = 300–780 R' = 7–32
reaction-bonded Si_3N_4	R = 220–580 R' = 0.5–10

*Theoretical density is dependent on the type and composition of consolidation aids (th.d. of pure $Si_3N_4 = 3.2\,g\,cm^{-3}$).

distance in the direction of the crystallographic *c*-axis is for α-Si_3N_4 about twice as large as for the β-modification (see Table I). The silicon atoms are located in the centre of irregular nitrogen tetrahedra, each nitrogen atom belonging to three tetrahedra. The Si_6N_8 unit cell of the β-phase is derived from the phenakit type (Be_2SiO_4) with the beryllium atoms being replaced by silicon and the oxygen atoms by nitrogen [17, 18]. The structure consists of Si_3N_4 layers which alternate in the sequence AB, forming hexagonal tunnels in the direction of the crystallographic *c*-axis.

In the $Si_{12}N_{16}$ unit cell of the α-phase, the layers known from the β-structure alternate with mirror-inverted layers in the sequence ABCD, resulting in a *c*-direction lattice distance which is about twice as large as for the β-modification (Table I). The hexagonal tunnels in the *c*-direction are not present in the α-phase.

According to older views, the α-Si_3N_4 phase is stabilized by further constituents, e.g. oxygen [18, 19]. However, current opinion is that α-Si_3N_4 is a more energy-rich, metastable form. The formation of α-phase seems to be associated with certain reaction routes during nitridation of silicon, like gas-phase reaction of silicon vapour or SiO with nitrogen [20–22]. With increasing temperature, the α-phase becomes increasingly unstable with respect to β-Si_3N_4. The transformation, however, is reconstructive and can occur with solution-precipitation by means of a liquid phase. Additionally, α–β transformation has been observed during annealing of RBSN [23, 24]; nevertheless, the mechanism of this reaction has not been clarified. A change in the reverse sequence β–α has once been reported in literature [25] but has yet to be confirmed.

In addition to the pure α- and β-phases, there exist some solid solutions of Si_3N_4 with certain compounds, both of the α- and β-Si_3N_4 structure [26]. As far as is known today, solid solutions based on the β-structure are formed only with aluminium and beryllium by a limited substitution of Si^{4+} and N^{3-} by Al^{3+} and Be^{2+},

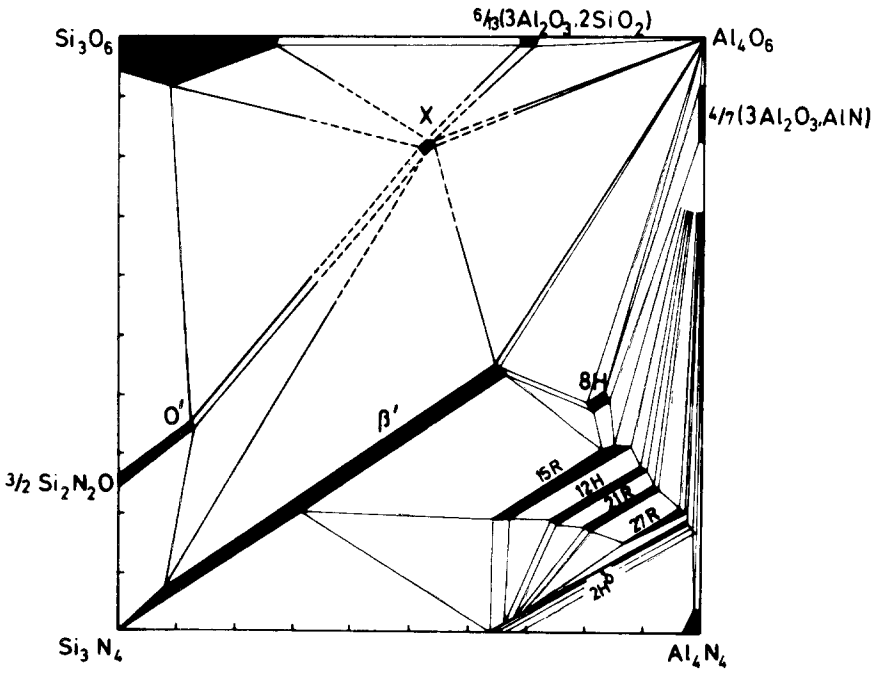

Figure 1 Phase relationships in the Si_3N_4–SiO_2–Al_2O_3–AlN system at 1700° C [27].

and O^{2-}. Thus, the cation/anion ratio of 3/4 remains constant and no constitutional vacancies are incorporated. In the case of aluminium substitution, this may be represented by $Si_{6-x}Al_xO_xN_{8-x}$ with a limit for $x \leqslant 4$, 2 (β'-SiAlON), in the case of beryllium it can be described by $Si_{6-x}Be_xO_{2x}N_{8-2x}$ with $x \leqslant 2$ (β'-SiBeON). As can be seen from the corresponding phase diagrams (Figs 1, 2), β'-SiAlONs are actually solid solutions between Si_3N_4 and $Al_2O_3 \cdot AlN$, β'-SiBeONs between Si_3N_4 and Be_2SiO_4. The formation of solid solutions results in a linear change of the lattice constants both in the crystallographic *a*- and *c*-directions up to the solubility limit. Deviations of the starting compositions from the stoichiometric ratio of solid solutions leads to the additional formation of amorphous or crystalline phases such as O', X or several AlN-based polytypes in the case of SiAlONs and wurtzite-based Be_3N_2-rich polytypes in the case of SiBeONs, as can be seen from Figs 1 and 2. All these polytypes show certain regions of solid solutions [27–29].

In addition to the β-Si_3N_4-based solid solutions, α-Si_3N_4-based structures have been detected with certain additives [30]. These α'-solid solutions are formed by partial replacement of Si^{4+} by Al^{3+}. Valency compensation occurs by incorporation of additional cations (e.g. lithium, calcium, magnesium, yttrium) which occupy interstices in the (Si, Al)–N structure. Using oxides as additives, nitrogen can also partly be replaced by oxygen. Therefore, these SiAlONs can be described by $Me_xSi_{12-(m+n)}Al_{(m+n)}O_nN_{16-n}$, which means a replacement of m(Si–N) units by m(Al–N) and n(Al–O) units. The Me incorporation seems to be limited to $x \leqslant 2$. With increasing substitution, the lattice constants increase, depending on the type of Me-cation.

It is rather difficult to give phase diagrams for these so-called α'-SiAlONs. Fig. 3 shows their occurrence in

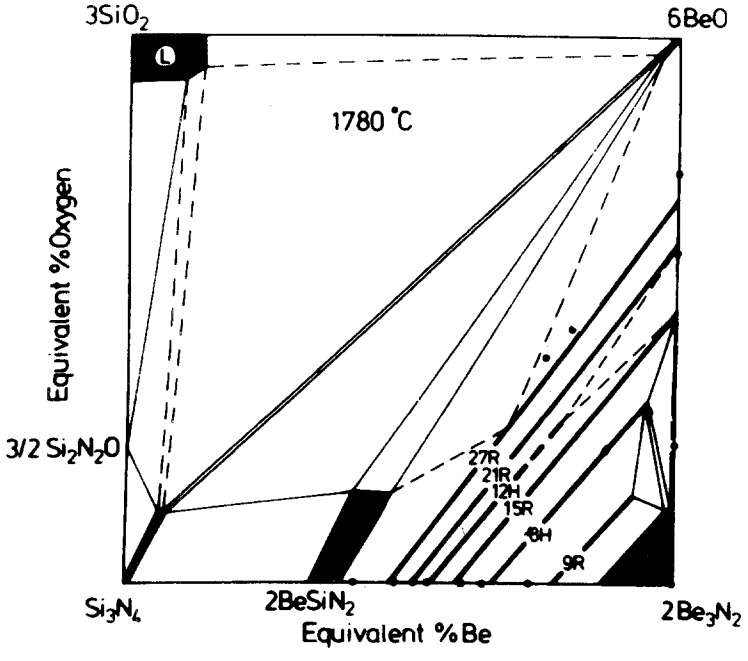

Figure 2 Phase relationships in the Si_3N_4–SiO_2–BeO–Be_3N_2 system at 1780° C [27].

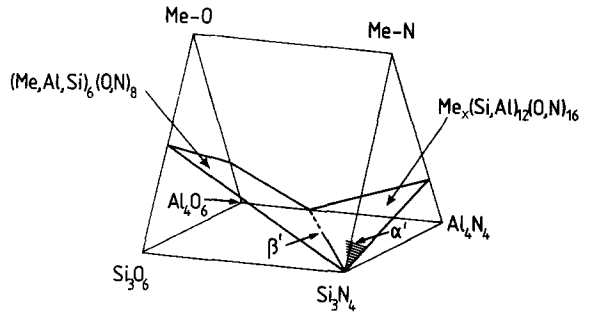

Figure 3 Phase relationships in the Me–Al–Si–O–N system [32].

a Me–Al–Si–O–N prism [31, 32]. As the substitution range of α'-solid solutions is usually smaller than for β'-solid solutions, the formation of single-phase α'-SiAlON is rather difficult. Deviations from the stoichiometry may lead to the simultaneous formation of other phases, e.g. β'-SiAlONs, as can be seen from Fig. 3. This, however, offers the possibility to produce pure two-phase α'–β' mixtures without the formation of amorphous residuals [31, 32]. Thus, these materials are thought to be promising candidates for high-temperature applications. The development of these materials, however, is still in an early stage.

2.2. Thermodynamic properties

Silicon nitride does not have a real melting point but decomposes under 0.1 MPa N_2 at 2173 K. The reaction during decomposition according to the formula

$$Si_3N_4(s) \rightleftharpoons 3Si(l) + 2N_2(g),\ \Delta G_f \qquad (1)$$

is of increasing importance above 1500° C (Fig. 4). Over the resulting liquid silicon the equilibrium partial pressure, p_{Si}, is set up

$$Si(l) = Si(v),\ \Delta G_v \qquad (2)$$

For the vapour pressures over Si_3N_4, the following equation is obtained

$$p_{Si}^3 \times p_{N_2}^2 = K \qquad (3)$$

with K, the equilibrium constant, being given by

$$K = \exp - \frac{\Delta G_f + 3\Delta G_v}{RT} \qquad (4)$$

This relationship is illustrated in Fig. 4. The lines from bottom right to top left are isotherms. The coexistence limit between silicon and Si_3N_4 runs from bottom left to top right. It represents nitrogen pressures above which Si_3N_4 exists as solid if there is an equilibrium partial pressure of silicon. This condition implies that Si_3N_4 will also decompose at high nitrogen pressures if silicon vapour is not prevented from escaping from the system and if, as a result, the silicon equilibrium partial pressure cannot build up. This means that an increased nitrogen pressure causes the silicon equilibrium pressure according to Equation 3 to fall below the equilibrium pressure value over liquid silicon and that a spontaneous decomposition of Si_3N_4 is thus suppressed [33]. In addition to gaseous silicon, Si_3N_4 is also in equilibrium with other gaseous substances such as SiN, Si_2N, Si_2, etc. (Fig. 5) [34]. In order to reduce decomposition of Si_3N_4, the partial pressures of these substances must be established and loss of these gaseous substances has to be impeded or prevented.

This decomposition reaction is of importance as, because of the high degree of covalent bonding in silicon nitride, very high sintering temperatures must be selected. This extensive covalent bonding means great bonding strength and hence low self-diffusion coefficients (Fig. 6). Diffusion of nitrogen in α- and β-Si_3N_4 (see nos 11, 12 in table of Fig. 6), which is assumed to be the slowest and rate-controlling step during sintering of Si_3N_4 for reasons of steric arrangement and electron neutrality, is about four orders of magnitude below the self-diffusion coefficients of oxygen and aluminium in polycrystalline Al_2O_3 (see nos 6, 7 in the table of Fig. 6) [36, 37]. As a consequence, Si_3N_4 cannot be highly densified without any additional measures. The difficulties and problems outlined above have led to the development of different approaches for the production of components from silicon nitride.

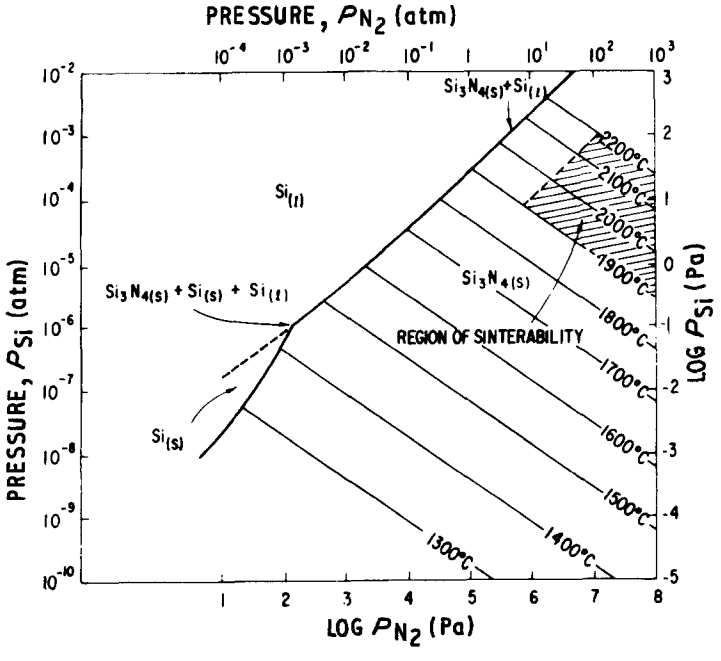

Figure 4 Silicon vapour pressure in equilibrium with silicon nitride as a function of nitrogen pressure and temperature [33].

TABLE II Overview of processing techniques of silicon nitride-ceramics: respective abbreviations used

Reaction-bonded silicon nitride	RBSN
Dense silicon nitride:	
Hot-pressed Si_3N_4	HPSN
Sintered Si_3N_4	
starting material Si_3N_4 powder	SSN
starting material RBSN	SRBSN
Hot-isostatically pressed Si_3N_4	
starting material Si_3N_4 powder	HIPSN
starting material RBSN	HIPRBSN
starting material SSN	HIPSSN
starting material SRBSN	HIPSRBSN

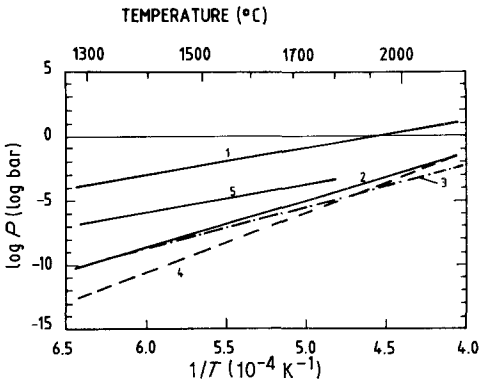

Figure 5 Vapour pressures of different species in equilibrium with silicon nitride and silicon [34]. Curves 1 to 4: N_2, Si, SiN and Si_2N, respectively, over Si_3N_4. Curve 5: Si over Si.

3. Processing of Si_3N_4 ceramics

Because of the high degree of covalent bonding, classical sintering is not applicable to produce pure dense Si_3N_4 ceramics. As a consequence, alternative techniques have been developed and/or supplementary means have been used, such as nitridation of silicon compacts or the addition of sintering aids to Si_3N_4 powders to create liquid-phase sintering with or without the application of pressure to assist the sintering process. These techniques comprise (see Tables II and III and Fig. 8): reaction-bonding (RBSN), hot-pressing (HPSN), sintering (SSN, SRBSN) and hot-isostatic pressing (HIPSN, HIPRBSN, HIPSSN, HIPSRBSN). Reaction-bonding results in a still porous material. Dense Si_3N_4, however, can only be produced on a technologically interesting scale by hot-pressing, sintering and hot-isostatic pressing, with the use of different oxide or non-oxide sintering additives, such as the frequently used MgO, Y_2O_3 or $Y_2O_3 + Al_2O_3$. In these cases, densification and microstructure are controlled by a liquid-phase sintering process. The processing steps and typical processing conditions of these techniques are summarized in Table III. Characteristics of each processing technique are also given in this table.

3.1. Reaction-bonding

In the case of reaction-bonding, the starting material is silicon powder which is consolidated by techniques such as isostatic pressing, injection moulding or slip casting. Before nitriding to convert silicon to Si_3N_4, a pre-sintering step in an inert atmosphere is often

TABLE III (a) Overview of the processing steps and typical processing conditions of the various production techniques for Si_3N_4 ceramics, and (b) characteristics of the processing techniques

	Reaction-bonding RBSN	Hot-pressing HPSN	Sintering SSN	Sintering SRBSN	Hot-isostatic pressing
(a)					
Starting materials	Si-powder	Si_3N_4-powder + additives	Si_3N_4-powder + additives	Si-powder + additives	→ ① Si_3N_4 (powder + additive)-compacts (HIPSN)
Processing steps	Moulding		Moulding	Moulding	
			→HIP ①		→ ②
	Nitridation ≤ 1420° C, ≥ 72 h	Hot-pressing ≥ 1700° C, ≥ 0.5 h ~ 30 MN m^{-2}	Sintering ≥ 1750° C, ≥ 1 h p_{N_2} ≥ 0.1 MPa	Nitridation ≤ 1420° C, ≥ 72 h	RBSN-parts with additives (HIPRBSN)
				→HIP ②	→ ③ Pre-sintered Si_3N_4-parts (HIPSSN)
			→HIP ③	Sintering ≥ 1750° C, ≥ 1 h p_{N_2} ≥ 0.1 MPa	
				→HIP ④	→ ④
Final product	Final part	Machining of the final part	Final part	Final part	Post-sintered RBSN (HIPSRBSN)
(b)					
Shrinkage (%)	0		~ 15	~ 5	~ 15
Post-machining	None	Intensive	Low	Low	Low
Final porosity (%)	≥ 20	~ 0	< 3	< 5	~ 0
Flexural strength (MN m^{-2})	~ 300 (RT–1400° C)	≥ 700 (RT–1000° C)	≥ 700 (RT–1000° C)	≥ 700 (RT–1000° C)	> 700 (RT–1000° C)

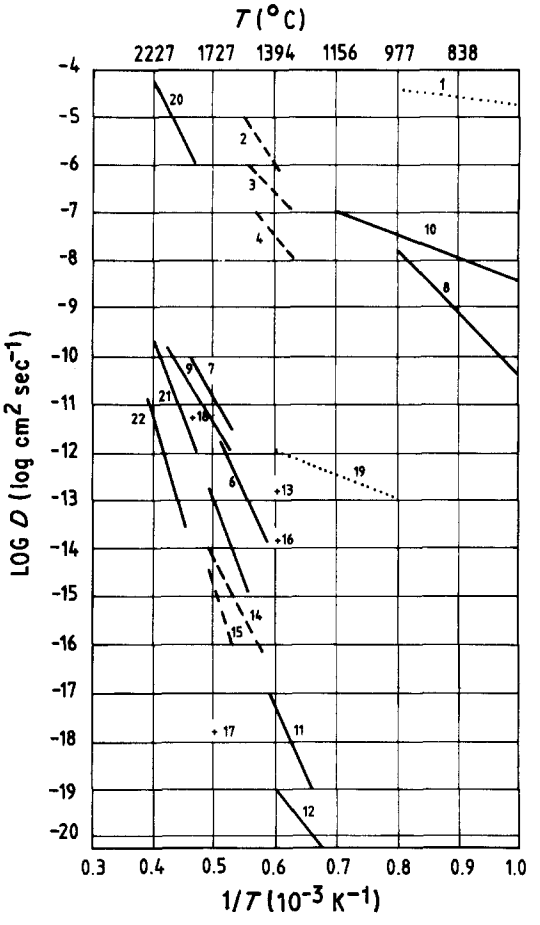

No.	Diffusing particle (ion or atom)	Medium	Activation energy (kJ mol^{-1})
1.	He	Fused silica	28
2.	O	CaO–Al_2O_3–SiO_2 liquid (40 : 20 : 40 wt %)	398
3.	Ca	CaO–Al_2O_3–SiO_2 liquid	293
4.	Si	CaO–Al_2O_3–SiO_2 liquid	335
5.	O	Al_2O_3 single crystal	635
6.	O	Al_2O_3 polycrystal	460
7.	Al	Al_2O_3 polycrystal	440
8.	Cu	Copper	
9.	Zr	ZrO_2, stab. (15 mol% CaO)	390
10.	O	ZrO_2, stab. (15 mol% CaO)	113
11.	N	β-Si_3N_4	778
12.	N	α-Si_3N_4	235
13.	Si	Si_3N_4, 1400° C	
14.	Si/N	In grain-boundary phase of: HPSN (+ 10 wt% Y_2O_3)	448 (T < 1550° C) 695 (T > 1550° C)
15.	Si/N	HPSN (+ 5 wt% MgO)	645
16.	C	SiC, 1400° C	
17.	N, Al	SiC	
18.	Si, Al	SiAlON	
19.	O	Fused silica	
20.	C	Grain-boundary diffusion in polycrystal β-SiC	563
21.	C	Lattice diffusion in polycrystal β-SiC	841
22.	Si	Lattice diffusion in polycrystal β-SiC	911

Figure 6 Diffusion coefficients in different materials [35]. (···) glass; (– – –) melt; (——) crystalline solid.

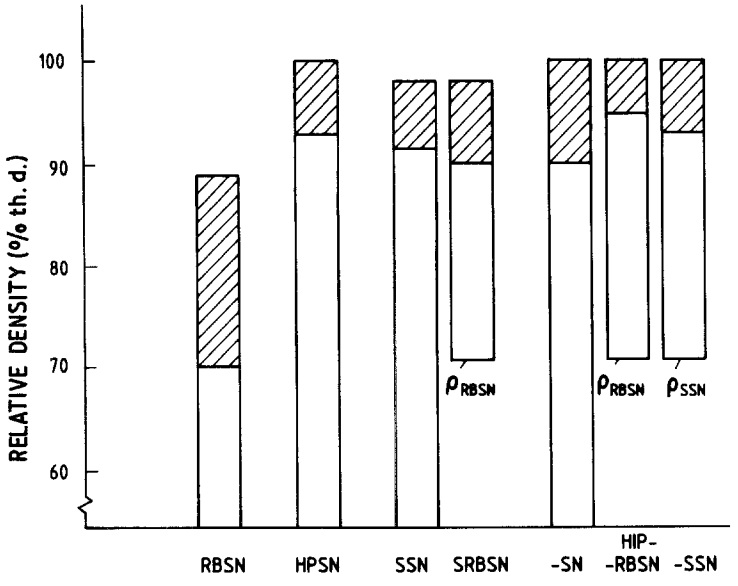

Figure 7 Density values of various types of Si_3N_4 [39].

inserted to provide sufficient strength to allow the powder compact to be machined to approximately the final required size. During the subsequent nitridation process only small dimensional changes occur (linear about $\pm 0.1\%$). The nitridation or reaction-bonding process is carried out under a nitrogen atmosphere in the temperature range up to 1420° C over several days. Because of the dimensional consistency, it is possible to produce complex components requiring no or only little subsequent machining. Thus, the reaction-bonding process is well suited for mass production with low costs. At present, density values of up to $2.8\,g\,cm^{-3}$, i.e. 12 vol % porosity, (see Fig. 7) and fracture strength data of up to about $350\,MNm^{-2}$ with a Weibull modulus $m = 20$ are achieved [4, 7, 8, 11–14, 38].

3.2. Hot pressing

Using hot-pressing, fully dense (see Fig. 7) and high-strength materials can be produced capable of being used at temperatures up to 1000 or 1100° C without a decrease in strength. Above these temperatures, a drop in strength occurs due to the softening of the mainly amorphous grain-boundary phase. The main limitation of hot-pressing, however, is the processing of components, as the extremely hard and strong HPSN is difficult to machine and the components made from this material are rather costly. Although during the last few years progress has been made in hot-pressing to form not only billets but also simple shaped parts, which reduces the high cost associated with diamond machining of HPSN to produce components of complex shape, HPSN is acceptable only for limited applications [4–8, 14, 40, 41].

Hot-pressed Si_3N_4 typically exhibits a certain amount of grain texture, i.e. it has a preferred orientation of the elongated β-crystals perpendicular to the hot-pressing direction. These orientated grains are responsible for differences in properties, e.g. strength, thermal conductivity, parallel and perpendicular to the hot-pressing direction, of up to 20% [42, 43].

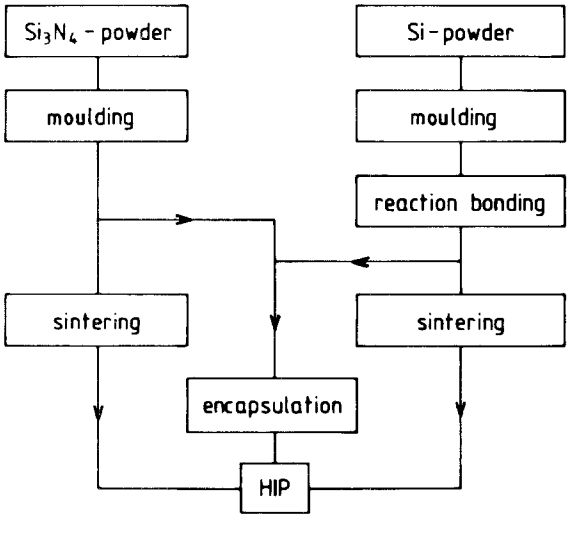

Figure 8 Different processing routes for HIPed Si_3N_4.

3.3. Sintering

3.3.1. Sintering of Si_3N_4-powder compacts

In order to produce complex-shaped components from dense, high-strength Si_3N_4 without substantial machining and therefore within a reasonable cost limit, the new techniques of sintering and hot-isostatic pressing have been developed. In particular, sintered Si_3N_4 is expected to offer a good combination of high strength and the possibility of forming almost the exact shape required for components on a larger scale.

Pressureless sintering of Si_3N_4 occurs, as in the case of hot-pressing, by a liquid-phase sintering process. Thus, in general for sintering and hot-pressing the variables affecting densification behaviour are similar. Nevertheless, in the case of pressureless sintering, two more factors have to be considered: first, the requirements for the starting powders are much higher (see Section 4.2.1) because both the thermodynamic driving force for sintering can be increased and diffusion distances for sintering can be decreased by using ultrafine powders. Second, control of the partial pressures of reactants in the sintering atmosphere can be used to avoid the dissociation of Si_3N_4. This can be realized in two ways: based on thermodynamic considerations by

sintering under high nitrogen pressure (see Section 2.2) and/or by embedding the composite Si_3N_4-additive to be sintered in a powder bed with a composition similar to the compact. This creates a local gas equilibrium in the immediate surroundings of the compact, minimizing decomposition and vaporization. With the use of high nitrogen pressure, higher sintering temperatures can be employed. At the present time, density values of higher than 97% th.d. (see Fig. 7) are routinely achievable, in some cases densities higher than 99% th.d. have been obtained [5, 6, 8, 33, 35, 44–50].

Development work in the USA and in Japan has shown that sintering of Si_3N_4 under high nitrogen pressure is a suitable technique to produce components from dense Si_3N_4 in an economical way. In particular in Japan, during the last few years progress has been made in improving this technique. Typical examples are components produced by injection moulding or isostatic pressing with subsequent sintering, such as rotors for gas turbines, pistons and turbochargers for Diesel engines, piston caps for motorcycles, and large parts for metal processing.

3.3.2. Post-sintering of reaction-bonded Si_3N_4

Because of the low green density, sintering of Si_3N_4-powder compacts to high densities involves relatively high shrinkage values within the range of 15 to 20% (linear shrinkage). As a consequence, in various cases the production of exact shapes of complex bodies may become difficult; thus, diamond machining of the densified components may also be required. These facts led to the consideration of using RBSN as the starting material for sintering [51] which usually exhibits higher starting densities (ϱ = 2.2 to 2.8 g cm^{-3}) than the compacted Si_3N_4-powder bodies (ϱ = 1.6 to 2.1 g cm^{-3}). As a result, full densification is accompanied only by a linear shrinkage of about 5 to 10%. As in the case of Si_3N_4-powder compacts, sintering aids have to be employed, causing densification by a liquid-phase sintering process. The sintering aids used are similar to those applied in sintered and hot-pressed Si_3N_4.

For component fabrication, the usual processing techniques for RBSN, for example isostatic pressing, slip casting or injection moulding, can be used (see Table III). This "green" compact is then nitrided to form the RBSN pre-form. The resultant RBSN material (which contains sintering additives) can be sintered in a nitrogen atmosphere under similar conditions to those used for Si_3N_4 powder compacts. Up to now high densities of 98.5% th.d. have been achieved (see Fig. 7) accompanied by a shrinkage of only 5 to 10% [8, 48, 51–53].

Sintering of RBSN is a relatively new processing technique for the production of sintered Si_3N_4. There are two main advantages of this technique. First, the high "green" density of RBSN which results in low sintering shrinkage. Thus, this process is thought to enable the production of complex shaped components with close dimensional tolerances and with good mechanical properties, maybe similar to those of HPSN. Second, the fabrication technology of RBSN as starting material, such as slip casting and injection moulding, is relatively well developed. For example, components, such as rotors, have been produced by post-sintering of RBSN using the slip-casting technique [52, 53]. The economic advantage of this technique (based on relatively cheap silicon starting powders compared to expensive highly sinterable Si_3N_4 powders in sintering of powder compacts), however, is partly compensated by the use of two thermal processing steps, the nitridation and subsequent post-sintering cycle.

3.4. Hot-isostatic pressing

Another technique which combines good mechanical and thermo-mechanical properties of Si_3N_4 with the possibility of producing complex shaped components is hot-isostatic pressing. Up to now, hot-isostatic pressing has been used for processing metals, hard metals, and also ceramics like piezoelectric materials, ferrites, other oxides (Al_2O_3, ZrO_2, BeO), nitrides (TiN, BN) and carbides (SiC) as well as several composites [8]. Many of these applications showed that physical and mechanical properties of ceramic parts can be improved, reliability increased and cost was reduced compared with conventional processes. Based on these results, it was thought that hot-isostatic pressing would also be a suitable method for the production of high-temperature structural ceramic parts made from Si_3N_4. For this reason during the past few years special HIP equipment has been developed to enable HIP densification at temperatures higher than 1700° C. HIP densification of high-temperature structural materials such as Si_3N_4 promises no machining of the densified material, except for surfaces with extremely close tolerances. Thus, this nearly accurate shape-processing technique is thought to offer a potential for the production of advanced ceramic components. Advantageous material properties of Si_3N_4 are mainly expected, compared to today's best HPSN materials, in three respects. First, the uniform way of applying the high pressure results in fully isotropic material properties. Second, the use of pressures up to about 300 MPa, which are more than one order of magnitude higher than in uniaxial hot-pressing, enhances the densification of Si_3N_4. As a result, dense Si_3N_4 parts can be produced from powders of lower sintering activity and powder compositions with smaller amounts of consolidation aids or with more refractory additives. Third, the use of high pressure is thought to yield, under optimized conditions, a more uniform and fine-grained microstructure which may lead to a further increase in strength. Therefore, the HIP process offers a good possibility of an improvement in high-temperature properties (due to the reduction of additives), improvement of the strength level and reduction in the scatter of strength values.

During hot-isostatic pressing, high pressure is applied via a gas to consolidate a powder compact or to remove residual porosity from pre-sintered materials. Three different routes can be followed in order to produce fully dense ceramic parts via the HIP

technique (Fig. 8): (i) HIP densification of Si_3N_4-powder compacts, pre-densified by any appropriate moulding technique to the final shape; (ii) HIP densification of reaction-bonded Si_3N_4, also pre-formed to final shape; (iii) HIP treatment of pre-sintered Si_3N_4, with SSN or SRBSN as starting materials.

The starting materials for all three techniques still contain, in most cases, a certain amount of consolidation aids. Generally the shrinkage during HIP densification is uniform and can be predicted from the density of the starting material. Using the first two techniques a barrier for the high-pressure gas has to be applied before hot-isostatic pressing, because the starting material contains open porosity. The starting material for the third technique is usually pre-sintered Si_3N_4 without any open porosity, which makes encapsulation unnecessary. If sintering and HIPing is carried out in one step, the process is called sinter–HIP.

Here it should be mentioned that additionally it is possible to combine Si_3N_4 parts produced by different techniques by means of HIPing. This process is called diffusion bonding or gas-pressure bonding. Using this technique, encapsulation is necessary.

Using the first two routes, fully dense materials have been obtained adding only low amounts of additives (see Fig. 7 [54, 55]. Following these routes, parts of cylindrical, conical and flat sections, and also components for gas turbines have been fabricated to final shape without any machining of the densified material. It has been reported [56] that the tolerances of the finished products are rather good and that shaped parts can be processed with tolerances and surface qualities acceptable for turbine blades.

Up to now only a few results have been reported on HIPing pre-sintered Si_3N_4 [57]. This technique will be studied in future in combination with the further development of the sintering technique. Density increase was only observed if the density of pre-densified Si_3N_4 prior to HIPing was higher than 93% th.d., that is, when complete closure of the open porosity had been achieved. Besides further densification, an improvement of properties is expected by this technique due to the healing of flaws and cracks under the simultaneous action of temperature and high pressure. The HIPing post-treatment of pre-sintered materials is thought, therefore, to be a promising technique for improving strength and reducing the scatter of the strength values for parts of complicated shape.

4. Dense silicon nitride

4.1. Formation mechanisms and microstructure of dense Si_3N_4 ceramics

4.1.1. Formation mechanisms

From the discussion in Sections 2 and 3, it appears that nearly complete densification of Si_3N_4 is only possible by utilizing the following steps, in most cases in combination: (i) use ultrafine powders, (ii) apply external pressure, (iii) increase the sintering temperature (simultaneously an increase of nitrogen pressure is necessary), (iv) establish the equilibrium partial pressures of the various silicon compounds by using a Si_3N_4 powder bed, and (v) particularly add sintering aids to form a liquid phase. As the first four steps do not result in a sufficient densification, the addition of sintering aids, forming a suitable liquid, is the most important step in the densification of Si_3N_4 [5, 6]. During densification it is also necessary to make sure that the equilibrium partial pressures over the additives and the SiO_2 (in the form of SiO), which are built up at high sintering temperatures, are established. If the liquid phase fulfils the conditions of good wettability and solubility of Si_3N_4, densification can be described according to the mechanisms of liquid-phase sintering formulated by Kingery: rearrangement, solution–diffusion–precipitation, and coalescence [58]. On the basis of these mechanisms the formation of dense Si_3N_4 can be described in the following way (see Fig. 9):

The sintering additive reacts with the phases containing oxygen, SiO_2 or oxinitride, which are always present on the particle surfaces of commercially available Si_3N_4 powders, to form the liquid phase. Impurities in the starting powder are often also incorporated in this

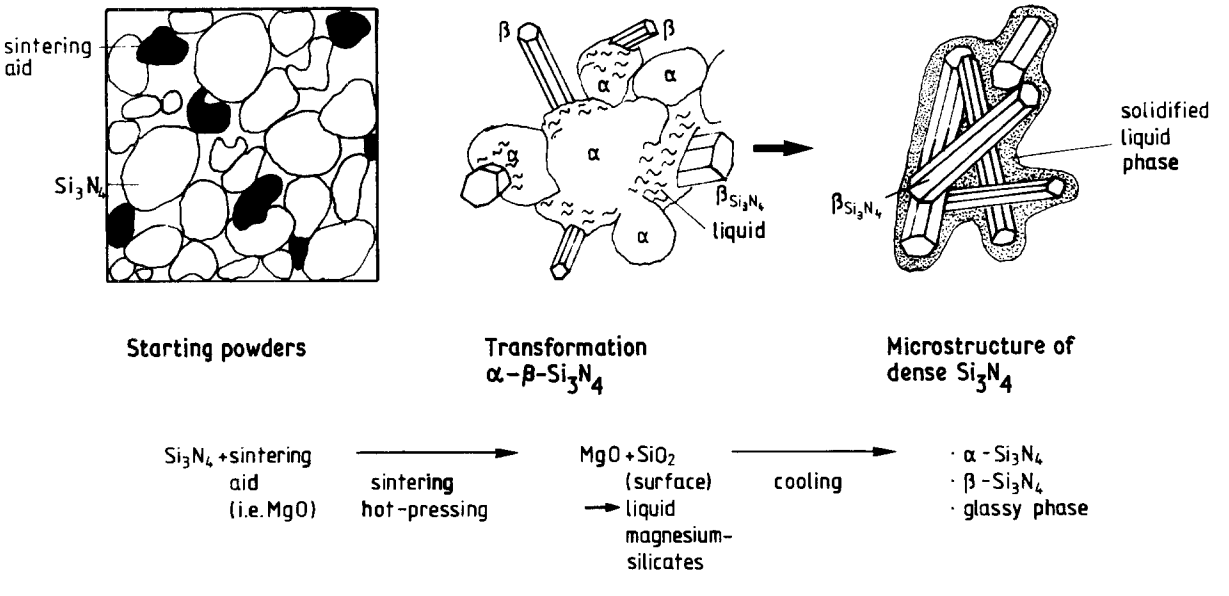

Figure 9 Solution–precipitation model for the liquid phase sintering of Si_3N_4 (schematic drawing).

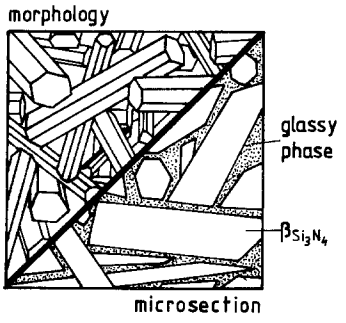

Figure 10 Microstructure of dense Si_3N_4 (schematic drawing).

silicate melt. If the amount of liquid phase is high enough and the viscosity at sintering temperature is sufficiently low, rearrangement processes will occur induced by capillary forces. The degree of densification in this first stage is mainly dependent on the particle size and shape and the amount and viscosity of the secondary phase [35, 39].

With increasing temperature, the solution–diffusion–precipitation process starts and is superimposed on the rearrangement process. The driving force in this second stage is the higher solubility at the contact points of the particles caused by capillary forces as well as the differences in the chemical potentials between small and large particles, which leads to an enhanced solution of small particles. As a result of the accelerated diffusion of the dissolved species in the silicate liquid compared to that of self-diffusion in Si_3N_4 (the diffusion rate is increased by about ten orders of magnitude), the densification rate is essentially increased. In addition, these processes can be accelerated by the simultaneous application of external pressure, as in the case of hot-pressing and hot-isostatic pressing [8, 41, 60].

For pressureless or pressure-assisted sintering, starting powders with high α-amount ($\geqslant$ 95%) are usually employed. The reason for this is that the α-phase becomes thermodynamically unstable at temperatures $\geqslant 1400^\circ$C and exhibits the tendency to transform into the stable β-phase. This instability of the α-phase causes an enhancement of the solution and therefore of the densification process. Moreover, precipitation of the dissolved material from the liquid phase is affected by the phase composition of the starting material. If the starting powder contains a large number of β-particles, the fine particles start to dissolve due to their higher chemical potential. The dissolved species continuously precipitate on the coarser original β-particles under nearly equilibrium conditions in such a way that their surface energy is minimized. This leads to large spherical or equiaxed grains. If, however, the starting powder contains only a low concentration of β-grains, high supersaturation in the liquid phase (with respect to β-Si_3N_4) is created locally due to the lack of sufficient β-nuclei. This is thought to result in a spontaneous nucleation and crystallization of idiomorphic rod-like β-grains, far from the thermodynamic equilibrium. This type of elongated β-morphology is typical of dense Si_3N_4 prepared from α-Si_3N_4-rich starting powders, and is very important for the mechanical properties (see Section 4.3) [41, 60–65].

The third stage of the liquid-phase sintering process is coalescence, which gives nearly no contribution to further densification. In this stage, however, grain coarsening takes place which – due to the effort to minimize the surface energy – is in many cases accompanied by an unfavourable change in morphology from the idiomorphic rod-like to a more equiaxed grain structure.

The liquid silicates solidify during cooling mostly to amorphous or partially crystalline phases which are arranged at the grain boundaries in thin layers or at the grain-boundary triple junctions. Only in some special cases (discussed in Section 4.2.2), is the liquid phase (at least partially) dissolved in the Si_3N_4 lattice to form solid solutions. The resulting microstructure is schematically shown in Fig. 10.

This description seems to be valid for all techniques to produce dense Si_3N_4. The technique employed affects the contribution and the kinetics of the different densification mechanisms.

4.1.2. Microstructure

As a result of the liquid-phase sintering process, the microstructure of dense Si_3N_4 can consist mainly of the two hexagonal phases α and β, and a mostly amorphous silicate or oxinitride grain-boundary phase (5 to 20 vol%), Fig. 10, which is arranged in thin grain-boundary layers of about 1 to 5 nm thickness and in larger concentrations at grain-boundary triple junctions.

This grain-boundary phase strongly affects the high-temperature properties (see Section 4.4.3.2). In all Si_3N_4 materials produced by a liquid-phase sintering process, such an intergranular phase has been found. With β'-SiBeON's however, some controversy exists in literature as to whether these materials contain a continuous amorphous intergranular phase [33, 66–68]. The thickness of these layers seems to depend on the type of additives, but not on the amount of liquid. An increase of the amount of liquid phase primarily leads to an increase of the volume at the triple points [31, 68]. All the impurities and additives are concentrated in this intergranular phase, with the exception of those which are able to form solid solutions with Si_3N_4 (see Section 2.1). It is considered that by careful choice of the starting composition, the whole liquid phase may be absorbed by the formation of solid solutions, and thus, a residual amorphous phase may be avoided. However, attempts to achieve this have not yet been completely successful. Although the intergranular phase contains some nitrogen (4 to 18 at %), it behaves like a silicate glass and its softening behaviour determines, to a certain extent, the high-temperature strength. Therefore, all constituents which reduce the viscosity of the glassy phase, e.g. calcium, aluminium, iron, must be avoided. It is therefore necessary to use highly pure Si_3N_4 starting powders to obtain good high-temperature properties. Attempts to modify the intergranular glassy phase in order to improve its properties include the increase of the N/O ratio, as higher nitrogen contents increase the viscosity [69], or the use of additives which allow (partial) crystallization. This is, for example, the reason

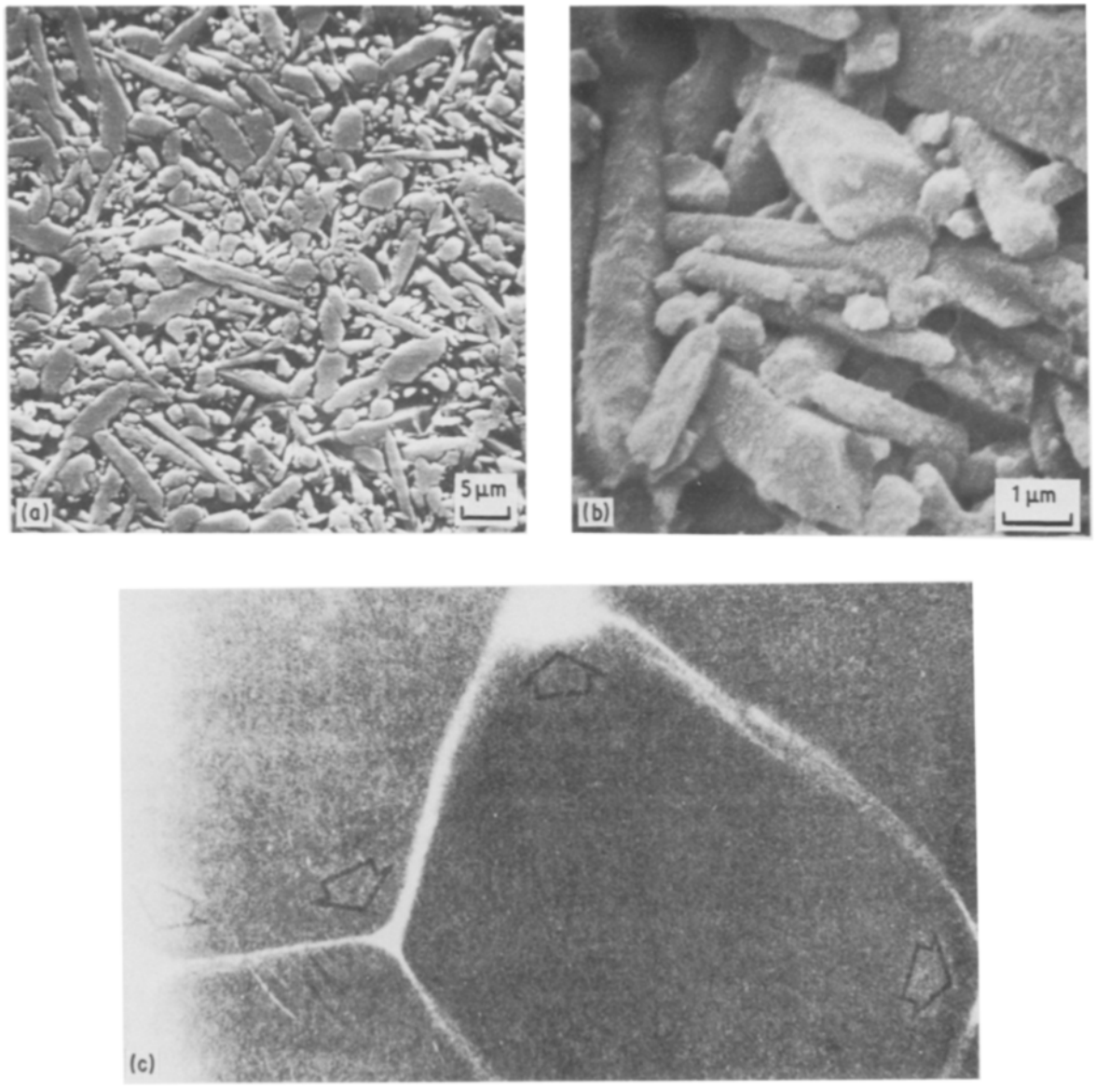

Figure 11 Typical microstructure of dense Si_3N_4 characterized by elongated β-grains (a and b) and by a glassy grain-boundary phase located in thin layers or at triple points (c). (a) Etched microsection, (b) Etched fracture surface (scanning electron micrograph), (c) Transmission electron micrograph (dark field) [67].

for using Y_2O_3 instead of MgO, as the former additive more easily leads to the crystallization of Y–Si–O–(N) compounds. Additionally, investigations are under way to devitrify the intergranular phase by a special post-heat-treatment.

One more typical feature of dense Si_3N_4 is the morphology of β-Si_3N_4. Whereas the residual α-grains are equiaxed (~ 0.1 to $2\,\mu m$), the β-phase exhibits elongated grain structure (~ 5 to $10\,\mu m$) with aspect ratios (= ratio length to thickness) of between 5 and 10 [59–65]. Here it should be noted that in most commercially available materials the $\alpha \rightarrow \beta$ transformation is completed. The elongated grain structure of the β-phase has a strong influence on the mechanical properties up to about 1000° C (see Section 4.3). The aspect ratio of the β-grains is mainly controlled by the phase composition of the starting material, the characteristics of the liquid phase (which are affected by the type and amount of additives and the impurity content), and some processing conditions. The optimization of all these parameters may lead to improved mechanical properties.

Typical microstructures are given in Fig. 11 indicating the elongated grain structure of the β-phase and the distribution of the grain-boundary phase. Microstructural characteristics of typical dense Si_3N_4 materials are summarized in Table IV. All these microstructural variables may affect the mechanical and thermal properties.

4.2. Relationships between powder properties, additives, processing conditions, and densification and microstructure of dense Si_3N_4

As outlined above, densification and microstructure of the different types of dense Si_3N_4, produced by pressureless sintering, hot-pressing and hot-isostatic pressing, are controlled by a liquid-phase sintering process. Based on the mechanisms taking place during liquid-phase sintering it may be deduced that both

TABLE IV Summary of the microstructural characteristics of dense silicon nitride

Formation mechanism:	liquid-phase sintering
Density:	nearly theoretical density depending on the amount and composition of the glassy phase (th. d. of pure Si_3N_4 3.20 g cm^{-3})
Phase composition:	
$-\beta/(\alpha + \beta)$	0.8 → 1.0
–glassy phase	~ 5–20 vol %
	arranged in 1 to 5 nm thick layers or in triple points. Composition and chemical structure depends on the type and composition of sintering aids (MgO, Y_2O_3, Al_2O_3, SiO_2)
Grain structure:	
–α-phase	equiaxed ~ 0.1–2 μm
–β-phase	rod-like ~ 5–10 μm aspect ratio 5–10

densification and microstructure are strongly influenced by the properties of the starting powder, the additive composition, and the processing parameters, which are mainly determined by the manufacturing technique. Major factors are: powder activity, phase composition, oxygen and impurity content and grain morphology of the starting powder, type and amount of additives as well as processing parameters, such as temperature, soaking time, sintering atmosphere, and in the case of pressure-assisted sintering, direction and magnitude of pressure. In particular, the composition of the starting powder and the phase relations in the system Si_3N_4–additives are important because these parameters control the composition and chemistry of the grain-boundary phases and the morphology of the resulting β-phase.

The influence of these parameters is briefly discussed below.

4.2.1. Influence of Si_3N_4 starting powder properties

The specific surface area, the oxygen content (in the form of SiO_2 or Si_2N_2O layers on the particle surfaces), the amount of carbon and metallic impurities, and the phase composition of the starting powders control the sintering behaviour. Powder morphology has an important effect on green densification and sintering characteristics. These powder properties are strongly dependent on the production technique and subsequent processing steps.

4.2.1.1. Production of Si_3N_4 powders. There are four main techniques to produce Si_3N_4 powders on a large scale [70–73]:

(A) Nitridation of metallic silicon powder:

$$3Si + 2N_2 \rightarrow Si_3N_4 \quad (5)$$

(B) Gas-phase deposition:

$$3SiCl_4 + 4NH_3 \rightarrow Si_3N_4 + 12HCl\uparrow \quad (6)$$

(C) Carbo-thermal reduction of SiO_2 in nitrogen atmosphere:

$$3SiO_2 + 6C + 2N_2 \rightarrow Si_3N_4 + 6CO\uparrow \quad (7)$$

(D) Precipitation of silicon diimide and thermal decomposition:

$$SiCl_4 + 6NH_3 \rightarrow Si(NH)_2 + 4NH_4Cl\uparrow \quad (8)$$

$$3Si(NH)_2 \rightarrow Si_3N_4 + 2NH_3\uparrow \quad (9)$$

There are marked differences in the type and amount of impurities, in the size and morphology of the powder particles and the phase composition of powders obtained from these techniques. By varying the processing conditions, however, the properties of powders produced by any of these techniques may be changed, particularly the phase composition, degree of crystallinity and particle morphology. Typical properties of powders produced by the techniques A to D are listed in Table V.

4.2.1.2. Fineness of the starting powders. For the nitrided powders (Type A powder) the specific surface area is mainly dependent on the subsequent processing steps. For example, the specific surface area can be increased by subsequent milling up to about 25 m^2 g^{-1}. The influence of increasing the fineness of powders, with approximately constant oxygen content, on the densification behaviour is shown in Fig. 12. The finer the starting powder, the higher the resulting sintered density. Here, however, it has to be considered that, in practice, an increase in the specific surface area is usually closely connected with an increase in the oxygen content (see Fig. 13) [64]. Fig. 13 also illustrates the effect of additive concentrations. Using a higher concentration of additive reduces the effect of fineness of the starting powder.

4.2.1.3. Oxygen content. Higher oxygen contents result in an increasing amount of liquid phase and thus in an enhancement of the rearrangement and diffusion

TABLE V Typical properties of Si_3N_4 powders produced by various processing techniques

Technique	Nitridation of Si (type A)	Vapour phase deposition (type B)	Carbo-thermal reduction (type C)	Diimide precipitation (type D)
Specific surface area (m^2 g^{-1})	8 → 25	3.7	4.8	9.1
O (wt %)	1.0 → 2.0	1.0	1.6	1.4
C (wt %)	0.14 → 0.4	–	1.05	0.1
Σ Fe, Al, Ca (wt %)	0.07 → 0.15	0.03	0.06	0.006
Crystallinity (%)	100 100	60	100	100
$\alpha/(\alpha + \beta)$ (%)	95 95	95	95	86
Morphology	equiaxed	equiaxed + rod-like	equiaxed + rod-like	equiaxed

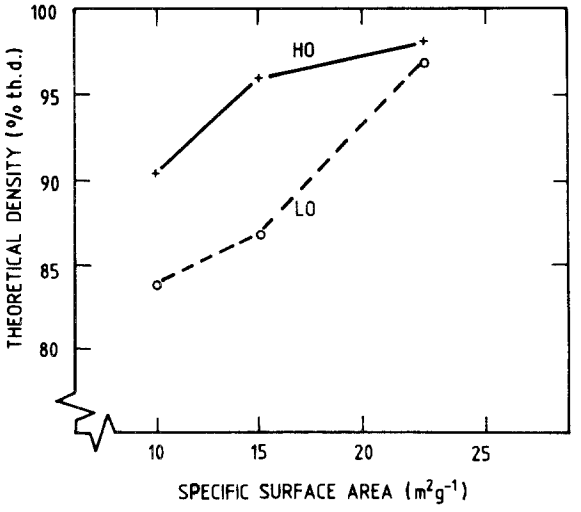

Figure 12 Influence of the specific surface area for two oxygen contents on sintering density [35]. High oxygen content (HO), ~3 wt % O_2; low oxygen content (LO), ~1.6 wt % O_2. 2 wt % MgO, 1950° C/30 min/30 bar N_2.

processes. For coarser grained powders this effect is more significant. In the case of fine grained powders, however, the specific surface area is the dominating factor. This is also demonstrated in Fig. 12. A certain oxygen content, of about 1.5%, seems to be necessary for high densification [33, 35].

4.2.1.4. Carbon content. The influence of free carbon, which is often high in Si_3N_4 powders of Type C, is to reduce the oxygen content by the reaction with the oxygen-rich surface layer of the powder particles to form volatile CO and/or SiO. As a consequence, the formation of the liquid phase is hindered and the amount and composition of the liquid is changed [35, 74].

4.2.1.5. Impurity content. The purity of the starting powders is dependent on the purity of the starting material for powder production, the manufacturing technique and the subsequent processing procedure. Usually the impurity content of the powders of Types B and D is lower than that of A and C. Impurities such as alkali and alkaline earth metals and compounds of aluminium or iron favour the formation of low-viscosity liquid phases. This has a positive effect on densification behaviour, but is detrimental to the high-temperature properties. In addition, impurities may lead to the formation of inclusions (e.g. WC, SiC, FeSi) which may reduce strength [75–78].

4.2.1.6. Phase composition. As already discussed in Section 4.1, high concentrations of the α-phase enhance the densification and the formation of rod-like β-grains. The resulting aspect ratio, $\bar{a}$, of the elongated β-grains as a function of the α/β-ratio in the starting powder is described in the literature [63] as $a = 1 + \alpha/\beta$.

Partially amorphous powders produced, for example, by gas-phase deposition (Type B powder) exhibit higher sintering activity. This effect is caused by the improved dissolution of amorphous phases (or submicrometre α-particles crystallized from the former amorphous phase) in the liquid phase during sintering [60, 63, 64]. However, their green compaction behaviour is bad due to an unfavourable particle morphology.

4.2.1.7. Particle morphology. The particle morphology is thought to have two effects. First, the partly fibre- or rod-like morphology of powders of Types B and C leads to low green densities and, secondly, to changes in the sintering characteristics. The former results in higher shrinkage values compared to those of equi-axed powders, giving rise to problems in sintering complex shapes (Figs. 13 and 14). The latter leads to densification over a narrower temperature interval as demonstrated in Fig. 14. This is believed to be caused by the impediment to rearrangement, because of the unfavourable grain morphologies and the superposition of the rearrangement and solution–precipitation stage of liquid-phase sintering. Additionally, the rate of solution may be increased, compared

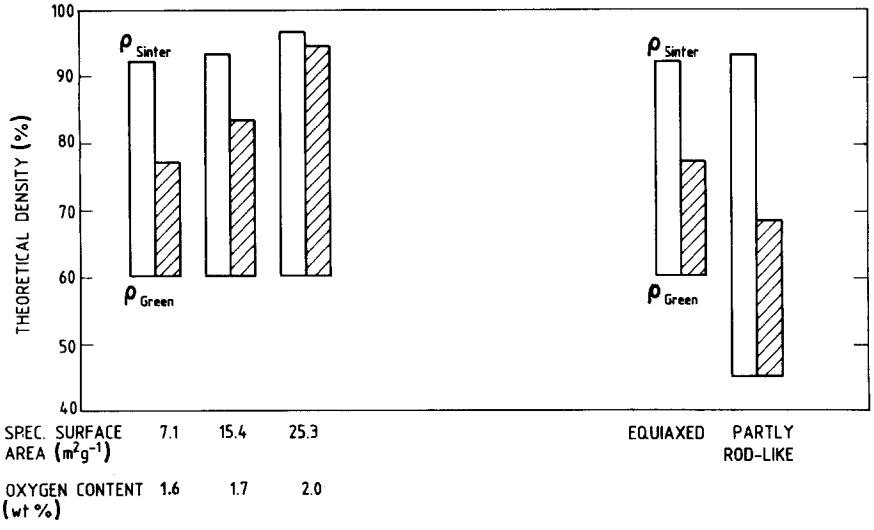

Figure 13 Influence of powder fineness and powder morphology of commercially available Si_3N_4 powders on green and sintered density for two additive concentrations [64]. Unshaded bars: $15Y_2O_3 + 3.4Al_2O_3$ (wt %), $\varrho_{th.} = 3.48\,g\,cm^{-3}$; shaded bars: $5Y_2O_3 + 1.13Al_2O_3$ (wt %), $\varrho_{th.} = 3.28\,g\,cm^{-3}$.

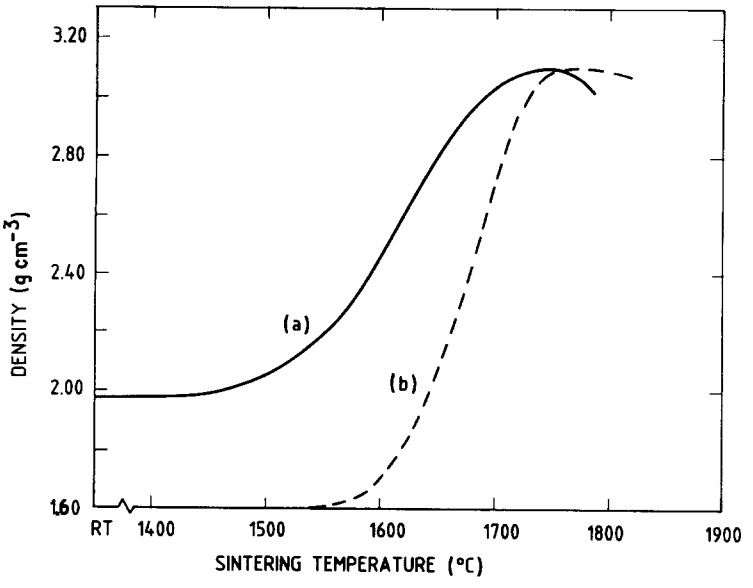

Figure 14 Sintering characteristics of two Si_3N_4 powders with different particle morphology [35]: (a) equiaxed, (b) partly rod-like; additive: 2 wt % MgO.

with that of powders of Type A, by the higher surface/volume ratios and probably by a higher degree of lattice defects. It is obvious that such densification characteristics may lead to difficulties in sintering large components.

In order to achieve the high densification and microstructure desired for good mechanical properties, the following powder properties are, in general, required (see Table VI in which the effects of powder properties on the different stages occurring during liquid-phase sintering and on room temperature- and high-temperature strength are listed): high specific surface area, high α-content, about 1.5 wt % O, low amounts of carbon and other impurities and an equiaxed particle morphology. It should be noted, however, that the significance of powder properties is reduced when hot pressing is employed instead of sintering and that they are even less significant when hot-isostatic pressing is employed [35, 50, 64, 79, 80].

4.2.2. Influence of densification additives

The type and amount of sintering additives determine the temperature at which densification commences and its rate during pressureless and pressure-assisted sintering. They also determine the morphology of the β-grains and the characteristics of the grain-boundary phase (see Section 4.1) which control the high-temperature properties. In this respect, the following characteristics of the secondary phase are of interest: the softening temperature of the additive–SiO_2 composition, the amount and viscosity of the resulting liquid phase at the sintering temperature, the solubility of nitrogen and the wettability of Si_3N_4 by the liquid phase. These characteristics are closely connected with the SiO_2 concentration on the Si_3N_4–particle surfaces and the impurity content of the starting powder. Thus, phase relations are very important in predicting the influence of the type and amount of the sintering additives on the densification behaviour and the microstructural development.

The various types of additives which have been employed can be divided into three groups [81–84]:

(a) Metal oxides and oxide mixtures which do not form solid solutions with Si_3N_4 like MgO, Y_2O_3, Al_2O_3, CeO_2, La_2O_3, Sc_2O_3, ZrO_2, Li_2O, SrO, $MgAl_2O_4$, $ZrSiO_4$. In many commercial materials, for example, MgO, Y_2O_3 or (Y_2O_3 + Al_2O_3) mixtures have been added. These oxides mainly react with the SiO_2 on powder surfaces and form a liquid phase which remains after cooling as an amorphous or partially crystallized grain-boundary phase.

(b) Oxide- or non-oxide additives or mixtures which form solid solutions, like BeO, Al_2O_3 + AlN, AlN + Y_2O_3, $BeSiN_2$. In the case of these materials, a liquid phase is also formed by reaction of the additives and the SiO_2 on the powder surfaces. Si_3N_4

TABLE VI Evaluation of the influence of powder characteristics on the sintering mechanisms and on mechanical properties

Powder characteristics	Sintering mechanisms		Mechanical properties	
	Rearrangement	S–D–P*	RT	HT
High specific surface area	+	++	++	
Spherical particle morphology	+	0	+	
High O content	++	++	+	–
High C content	–	–	–	
High impurity content	++	++	+	–
High α–Si_3N_4 content	0	++	++	
High amorphous constituents	–	+	+	

*S–D–P: solution–diffusion–precipitation.
+: positive effect/promotion.
0: indifferent/unknown effect.
–: negative effect.

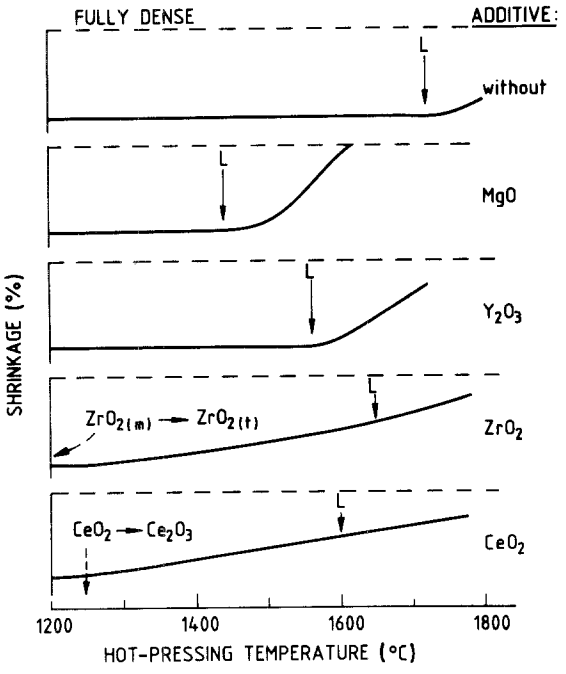

Figure 15 Influence of the type of additive on the densification of Si_3N_4 by hot-pressing (schematic plot) [5].

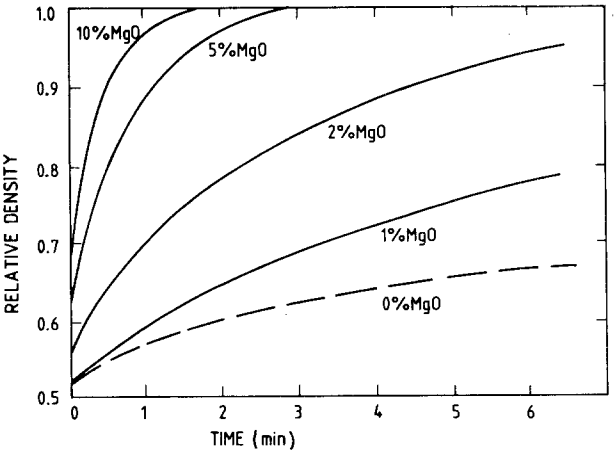

Figure 16 Influence of the amount of MgO addition on the densification of Si_3N_4 by hot-pressing; $T = 1650°C$, $p = 20\,MN\,m^{-2}$ [41].

is dissolved in the liquid, and Si_3N_4 solid solutions are precipitated which incorporate a certain amount of the additives. Thus, the amount and composition of the liquid phase changes gradually. Theoretically, a material without an amorphous intergranular phase might be achievable [26–32, 85]. Usually, materials consisting of Si_3N_4 solid solutions are known under the name SiAlON or SiBeON; the first material group is commercially available.

(c) Non-oxide additives or mixtures like Mg_3N_2, Be_3N_2, ZrN, ZrC, Zr + AlN. This group of additives has been used in order to improve the high-temperature properties by avoiding a low-viscosity grain-boundary phase. Further investigations are necessary to learn more about the densification mechanisms and to achieve satisfactory density values, microstructures and properties.

A schematic plot of the influence of various oxide additives, compared to Si_3N_4 without additives, on the densification behaviour is shown in Fig. 15 [5]. The upper curve shows that the shrinkage of Si_3N_4 without additives is limited even at high temperatures. The other curves are determined by the softening temperature and viscosity of the secondary phase which mainly controls the rearrangement and the solution–diffusion–precipitation processes. For example, in the case of MgO addition the eutectic temperature of the mixture $MgO–SiO_2$ is about 1540° C but this can be lowered by impurities to about 1400° C. With increasing temperature the viscosity of the liquid is decreased. As a result, rearrangement and subsequently the solution–diffusion–precipitation processes are enhanced. In the cases of Y_2O_3, ZrO_2 and CeO_2 additives, the softening temperatures with SiO_2 are higher and densification consequently starts at higher temperatures. Because of the higher viscosities of these liquids, the densification rates are lower, which is indicated by the lower slopes of the curves. In the cases of Y_2O_3 and ZrO_2 additives, the melts are more stable, thus higher temperatures can be applied if an increased nitrogen pressure is used to suppress the Si_3N_4 decomposition. Softening temperature, viscosity and, consequently, the start of sintering, the densification rate, thermal stability of the liquid and the total shrinkage, can be changed by adding a second oxide [86, 87]. One important example is the $Y_2O_3–Al_2O_3$ mixture which, compared to an addition of pure Y_2O_3, results in a decrease of the softening temperature and viscosity, but also in a reduction of the thermal stability. As a result, the densification rate and the total shrinkage are high, but the high-temperature behaviour is not satisfactory.

Additionally, the viscosity of the liquid has a strong effect on the grain morphology. A strong relationship has been found between the viscosity of the liquid phase and the aspect ratio of the precipitated β-Si_3N_4 grains. Probably due to a slow reduction of local supersaturations by high viscosity melts (meaning low diffusion rates), after spontaneous nucleation, grains of very high aspect ratios crystallize. During subsequent annealing, the reduction in aspect ratio is also low for high viscosity melts, as the diffusion rate is low. Consequently, materials processed with additives which form liquid phases of high viscosity consist of grains with higher aspect ratios, and therefore, show better mechanical properties, particularly at room temperature. In this respect the amount of liquid phase seems to be of secondary importance for the low-temperature properties. Of course, some sort of compromise has to be chosen between high viscosity (to improve the high-temperature properties and to optimize the aspect ratio) and appropriate densification behaviour [61, 64, 65, 83]. Promising additives with this respect are pure Y_2O_3 or Sc_2O_3 [88–90].

As well as by the type of additive, densification can be improved by higher amounts of the liquid phase caused, for example, by higher additive concentrations. Enhancement of densification during hot-pressing by increasing the amount of the secondary phase is demonstrated in Fig. 16 for MgO additions [41]. Usually the amount of additives is varied between 1 and about 15 wt %. For example,

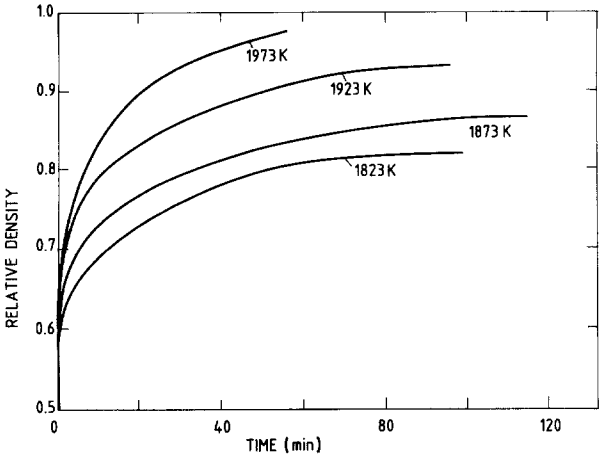

Figure 17 Densification of α-Si_3N_4 + 5 wt % MgO by hot-pressing at varying temperatures, $p = 29.4\,MN\,m^{-2}$ [41].

commercially available MgO-fluxed HPSN contains about 2.5 wt % MgO, (Y_2O_3 + Al_2O_3)-fluxed HPSN and SSN about 8 wt % Y_2O_3 and 2 wt % Al_2O_3. The amount of a sintering aid necessary to achieve high densities can be reduced by applying external pressure, as in the case of hot-pressing or hot-isostatic pressing.

As already pointed out, compositions which form solid solutions based on β- or α-Si_3N_4 structures are of particular interest. It was thought that these compositions would solve the high-temperature softening problem because in the ideal case no amorphous grain-boundary phase should remain. However, in processing SiAlONs it has been found that dense materials can only be produced if a certain amount of oxygen surplus is present. In this case, the excess of the oxygen-rich melting phase remains at the grain boundaries and has a detrimental effect on the high-temperature properties. Adding Be_3N_2 or $BeSiN_2$ additives, β'-SiBeON solid solutions with minor amounts of residual amorphous phase and good high-temperature properties could be achieved. The application of these beryllium compounds, however, is strictly limited due to their toxicity [33, 85, 91]. In sintering such compositions, it seems that the formation of the solid solution is the rate-limiting process during the solution–precipitation step. As a result, grain growth occurs nearly in an equilibrium state which leads to the formation of more equiaxed grains than in systems without solid solution. Thus, the interlocking effect of elongated grains is reduced and mechanical properties at room-temperature (up to about 1000° C) are usually inferior to those of materials consisting of grains with high aspect ratios. Although materials with α-based structures are under investigation, the same problems are anticipated [32, 91, 92].

4.2.3. Influence of processing conditions

Important process parameters are temperature, time, atmosphere and pressure. In addition, in some cases special conditions are used.

In general, higher temperatures and longer soaking times enhance densification (Fig. 17). The temperature, however, is limited by the decomposition of Si_3N_4 and the vaporization of the liquid phase. Moreover, it has to be considered that long soaking times and high temperatures favour grain growth and lead to a change in grain morphology towards equiaxed grains [64, 65, 93, 94]. These microstructural changes result in a strength degradation for long soaking times (Fig. 18) although the density remains nearly constant.

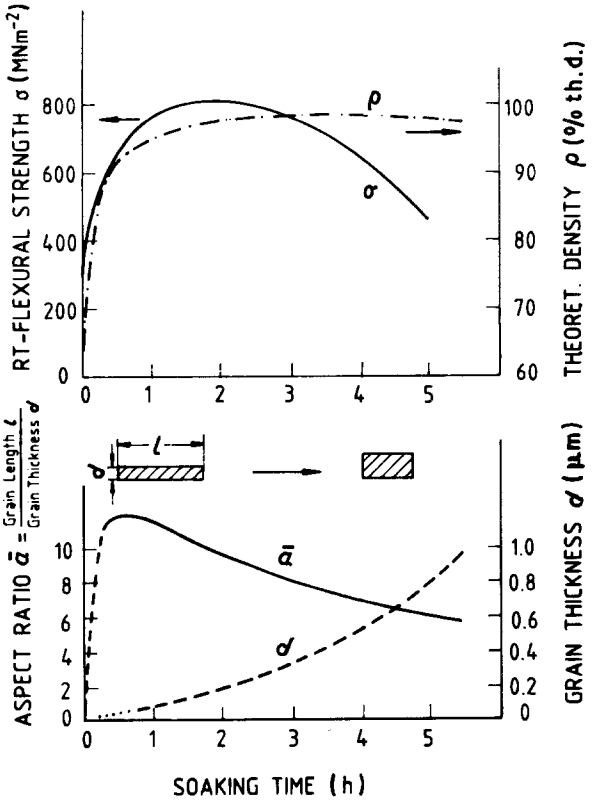

Figure 18 Density and microstructural characteristics (aspect ratio, $\bar{a}$, and mean thickness, d) of the β-crystals, and resulting room-temperature strength as a function of sintering time (schematic plot) [93].

Examples of special processing conditions are the application of high nitrogen pressure, the powder bed technique, and the encapsulation technique during sintering, and hot-isostatic pressing.

In the following, essential processing conditions are discussed for the important production techniques of dense Si_3N_4. When discussing the influence of these parameters on densification and microstructure two facts have to be considered: first, in most cases processing conditions are closely connected with the properties of the starting powders and the type and amount of sintering additions, and thus have to be coordinated with these factors. Second, using different production routes the significance of powder properties and additives will be different.

4.2.3.1. Hot pressing. In addition to temperature and time, the next most important processing parameter is the uniaxial pressure. The influence of pressure on densification is illustrated in Fig. 19 which shows that the densification rate increases as the pressure increases. In addition, the influence of the applied pressure on the resulting grain size is of importance. Fig. 20 shows results of one of the few quantitative microstructural analyses performed in dense Si_3N_4. It indicates that a finer grain size is obtained, for the

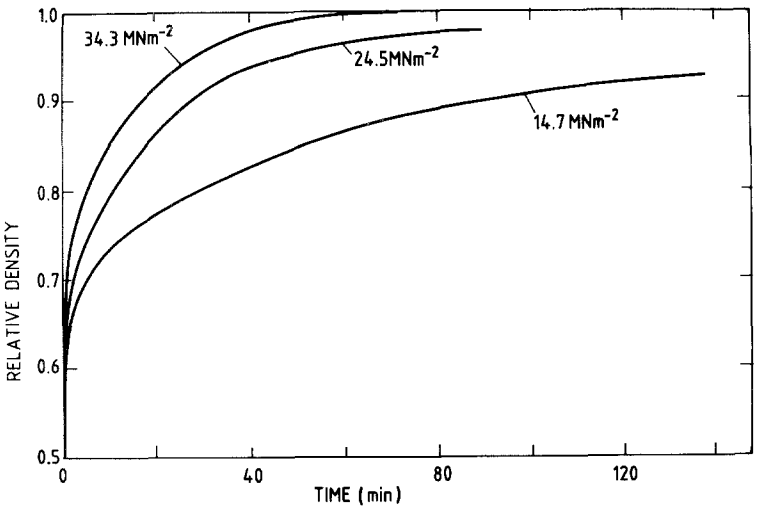

Figure 19 Densification of α-Si_3N_4 + 5 wt % MgO by hot-pressing at varying pressures, T = 1700° C [41].

same transformed volume fraction of β-Si_3N_4, with higher pressure [60]. This result may be interpreted by assuming that increase in the nucleation rate occurs with increasing pressure due to higher pressure-induced solubility at the highly stressed particle contact points. Furthermore, increasing pressure seems to increase orientation effects in the microstructure (see Section 4.3). Systematic investigations have shown that there is a relationship between the amount and viscosity of the liquid phase present during hot-pressing and the degree of orientation (see [95]). With higher viscosity, orientation effects are increased.

As already stated, the significance of powder properties and additives on densification and microstructural development is reduced due to the applied external pressure [40, 41, 59, 60].

4.2.3.2. Sintering. As discussed in Section 4.1, it is necessary to avoid the decomposition of Si_3N_4 and to control the equilibrium partial pressures. This can be realized by using the powder-bed technique and by applying high nitrogen pressures.

During sintering the optimum process parameters of temperature, time and nitrogen pressure are dependent on each other and are determined by the powder properties and the type and concentration of sintering additives. As an example, Fig. 21 shows the densification behaviour of two compositions with constant ratio Y_2O_3/Al_2O_3 but different total amounts of additives as a function of sintering conditions [89]. Samples prepared from the mixture with the highest addition reach the final sintering density at 1800° C, 1 h + 1820° C, 1 h (under 0.1 MPa N_2), whereas samples made with the lowest addition need to be soaked for at least 2 h at these temperatures. This demonstrates the influence of the amount of addition and consequently the volume of liquid phase formed, on the densification.

The sintering temperature to be used depends on the nitrogen pressure. Under 0.1 MPa N_2 (atmospheric pressure), temperatures are limited to those below about 1820° C. Embedding the samples in a mixture consisting of BN (to avoid fritting), Si_3N_4 and additive(s) suppresses decomposition and vaporization by establishing the equilibrium partial pressures over the constituents. The use of the same additive concentration in the powder bed as in the samples helps to prevent concentration gradients. Higher sintering temperatures are applicable by sintering under

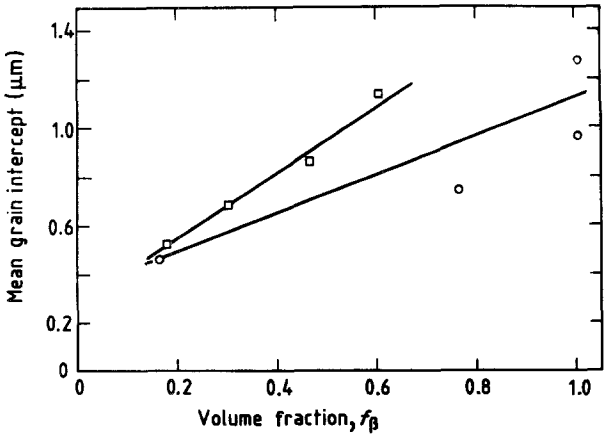

Figure 20 Mean grain intercept as a function of transformed volume fraction of β-phase for materials hot-pressed with different applied pressures [60]. T = 1600° C, f_β = 0.04, 5 wt % MgO. (○) p = 70 MN m^{-2}, (□) p = 35 MN m^{-2}.

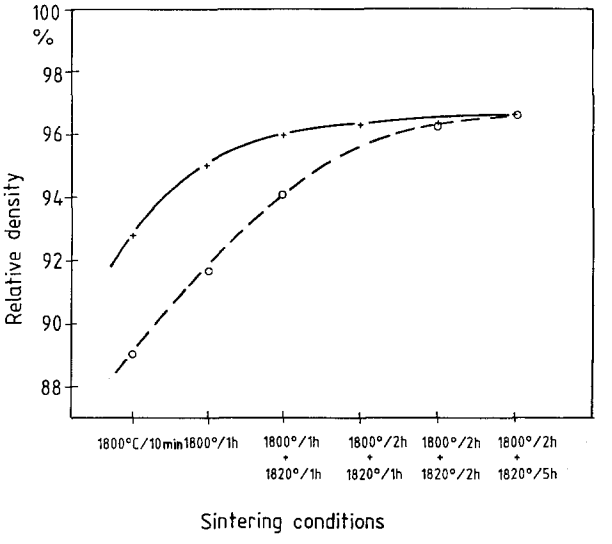

Figure 21 Sintering behaviour of two compositions with different total amounts but constant ratio of (Y_2O_3 + Al_2O_3) additions [93]. (+) 15 wt % Y_2O_3 + 3.4 wt % Al_2O_3; (○) 10 wt % Y_2O_3 + 2.3 wt % Al_2O_3. Powder: Type A.

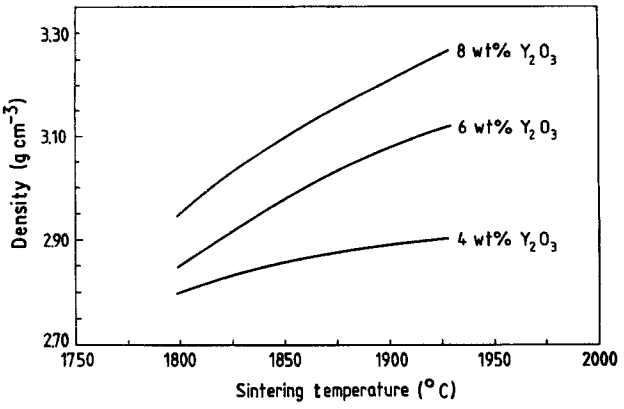

Figure 22 Sintering behaviour of SRBSN as a function of Y_2O_3 concentration [52]. $t = 6$ h, $p_{N_2} = 2$ MPa.

increased nitrogen pressures. Up to now, equipment has been used which allows nitrogen pressures up to 10 MPa and temperatures up to 2200° C. Such high temperatures allow the use of more refractory and/or lower amounts of additives. Several investigations, however, have shown that the successful use of this gas-pressure sintering technique demands a two-stage sintering cycle, consisting of a pre-sintering stage at relatively low pressure and a second stage under increased nitrogen pressure. During the first stage the open porosity must be removed in order to achieve nearly complete densification during the second stage. Otherwise, highly pressurized gas will be trapped in the pores, preventing complete densification or even a reduction in density after sintering at higher temperatures, due to swelling of the pores as a result of the thermal expansion of the gas. Thus, the problems are similar to HIPing. The amount of additive must be sufficiently high for the open porosity to be removed in the first stage. In order to achieve this, gas-pressure sintering is advantageous (compared with sintering under 0.1 MPa N_2), as the pre-sintering may be performed under slightly increased nitrogen pressure (e.g. 0.5–1 MPa) at temperatures between 1850 and 1950° C. Encouraging results have been achieved with this two-step technique [88, 96, 97]. It may be anticipated that, by detailed correlation of powder properties, type and amount of sintering additives and process conditions, further improvement in materials' properties will be obtained.

*4.2.3.3. Post-sintering of RBSN.*The sintering aids used are similar to those applied in sintered and hot-pressed Si_3N_4. They may be added to the silicon powder before nitridation, by infiltration of RBSN with salt solutions or by diffusion of the additives in the vapour form into the pre-formed RBSN. The sintering additives may affect the nitridation process and the resulting microstructure [98, 99]. The resultant RBSN material can be sintered in nitrogen at atmospheric pressure at about 1800° C, or using nitrogen overpressures at temperatures of up to 2000° C (see Table III). The optimum sintering conditions again are dependent on the type and concentrations of the additives. In order to minimize the thermal decomposition of Si_3N_4 and to prevent the migration of additives out of the samples, the RBSN pre-forms often are also

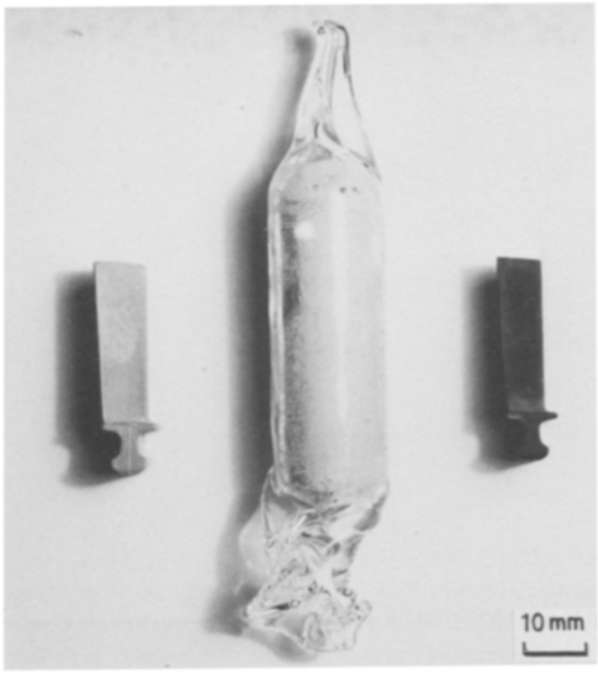

Figure 23 Encapsulation of turbine blades [55].

embedded in a powder bed consisting of a mixture of Si_3N_4 and sintering additives [48, 51–53].

Up to now, relatively little information is available concerning the influence of process conditions on densification, microstructure and properties. Fig. 22 shows, as an example, the relationship between density and sintering temperature (under 2 MPa N_2 pressure) for different amounts of additive. As can be seen, only RBSN with 8 wt % Y_2O_3 could be sintered to high densities at about 1925° C, 6 h [100]. Recent results indicate that the pore structure of the starting RBSN has a strong influence on densification behaviour and resulting microstructure and properties [101].

4.2.3.4. Hot-isostatic pressing. The main characteristic of hot-isostatic pressing is the application of high isotropic pressures usually transmitted by a high pressurized gas. This allows the production of complex-shaped components as well as the improvement of materials properties (see Table III and Section 4.3). As described in Section 3.4, all starting materials which exhibit open porosity have to be encapsulated before HIPing to prevent the penetration of the highly pressurized gas into the compact. Up to now, refractory metals, such as tantalum, molybdenum, tungsten, ceramics and different types of glasses have been used. The encapsulation of complex-shaped components, particularly for parts with sharp edges and corners, presents serious difficulties in hot-isostatic pressing. For example the encapsulation of large parts, the prevention of the reaction between the ceramic and the container material, the decapsulation of complex-shaped components without causing any damage and economical processing have to be solved. For the canning of complex-shaped components, special encapsulation techniques, such as the application of a glass-particle envelope and subsequent hot-evacuation through the still porous and permeable glass envelope and sealing of the glass envelope, or

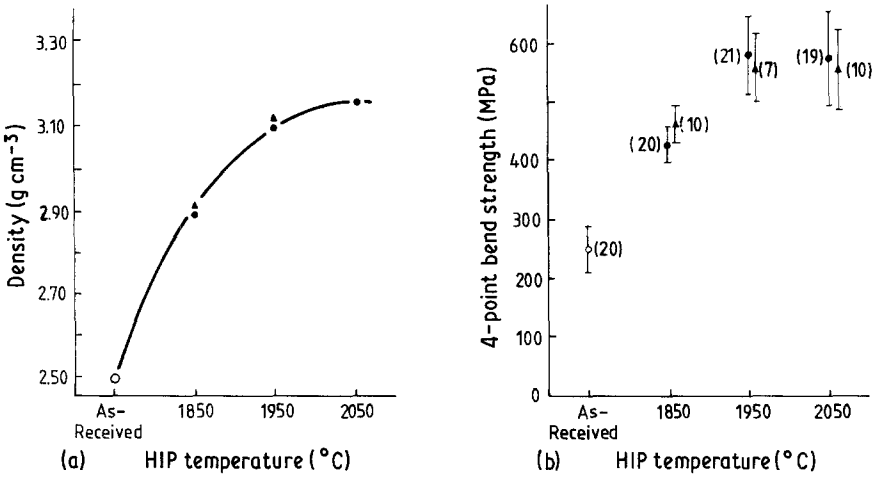

Figure 24 Effect of hot-isostatic pressing temperature and barrier layer material on (a) density, (b) room-temperature strength of RBSN [104]. (Numbers in parenthesis represent number of specimens tested; bars represent ±1 S.D.). (●) BN barrier layer, (▲) SiO_2 barrier layer.

canning by a two-layer method have been developed [54, 56, 102, 103]. An example of the encapsulation of small components is given in Fig. 23. Using this technique, turbine blades are embedded into boron nitride powder by cold isostatic pressing. After this, the compact is encapsulated in a silica glass tube. The boron nitride powder bed acts in this case as a pressure transmitter avoiding stress and reaction zones [55].

If the problem of encapsulation is solved, for the powder compact- and RBSN-routes the processing conditions temperature, time and pressure are of importance for the degree of densification and the resulting microstructure. On the other hand, the choice of the processing conditions depends on the characteristics of the starting material, e.g. grain size, additive amount, density. An example of the influence of HIP temperature on densification and strength of a RBSN material without additives, embedded in two different types of barrier layers inside a tantalum can, is given in Fig. 24 [104]. As expected, densification and strength are improved with rising HIP temperature. No marked influence of the type of barrier layer was found on the densification behaviour and the room-temperature strength. The slight drop in strength of materials HIPed at highest temperatures seems to be due to grain growth and globularization effects.

Higher pressures generally improve densification compared with sintering or hot-pressing. This allows a reduction of the additive amount or the use of more refractory additives. Additionally, the high pressure is thought to result in a finer grained microstructure (see Section 4.2.3.1.). The evaluation of the pressure dependence of densification was analysed for RBSN containing 0.5 to 5 wt % MgO and 0.7 to 7 wt % Y_2O_3 (Fig. 25) [105]. With 10 MPa gas pressure at 1750° C, 1 h, complete densification of all materials can be achieved. Increased pressure neither led to essentially higher densities nor to significant improvements of room-temperature strengths. Different types and amounts of additives, however, resulted in markedly different microstructures. Further optimization work is necessary in this field.

Up to now it seems that the results of HIP densification of pre-sintered Si_3N_4 are strongly dependent on various microstructural characteristics of the sintered starting materials, e.g. density, grain size, grain morphology, characteristics of grain boundary. Therefore, this technique will need to be studied in future in combination with the further development of the sintering technique. Recent HIP experiments with several types of pre-densified Si_3N_4, which were carried out in the temperature range 1700 to 1900° C under a pressure of 200 MPa using argon or nitrogen as pressurized gas, showed three interesting results [106]. First, a

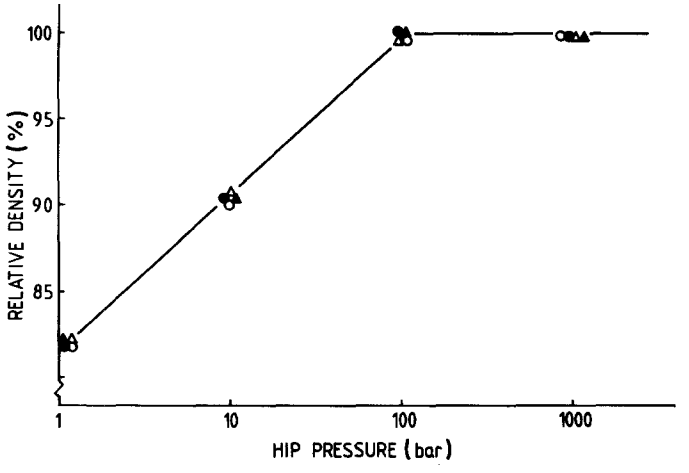

Figure 25 Relative density of additive-containing HIPRBSN materials (HIP-conditions: 1750° C, 1 h) as a function of HIP-pressure [105]. Y_2O_3-content, wt %: (△) 0.7, (▲) 1.4, (○) 4.2, (●) 7.0.

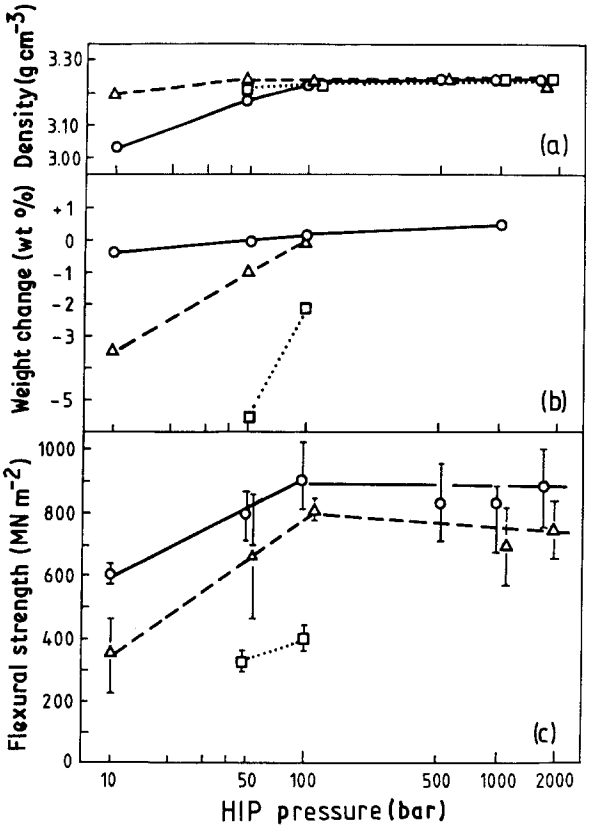

Figure 26 Relationship between HIP pressure and (a) density, (b) weight change, (c) flexural strength [106]: HIP-Temperature, °C: (○) 1700° C, (△) 1850° C, (□) 2000° C, 1 h.

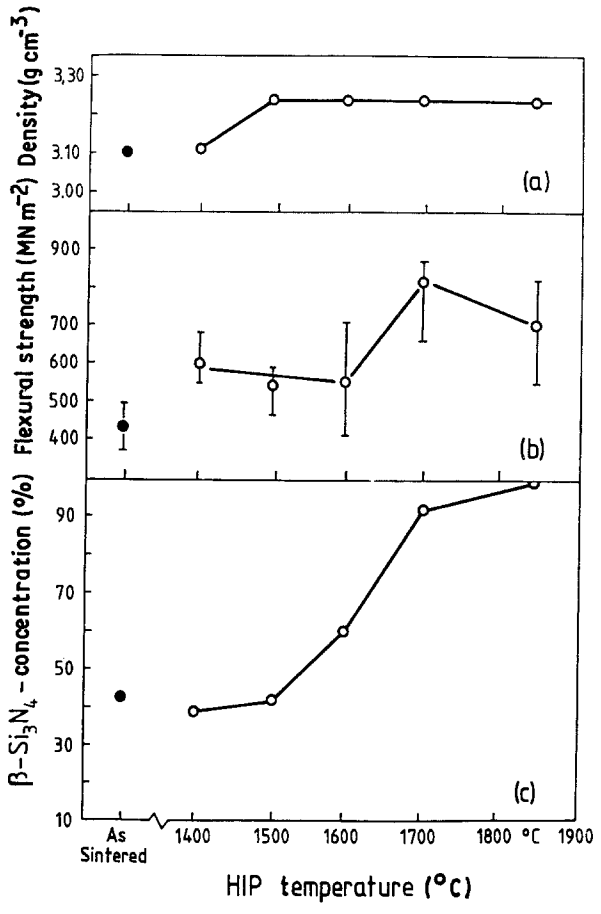

Figure 27 Relationship between HIP temperature and (a) density, (b) flexural strength, (c) amount of β-phase (HIP: 1 h, 100 MPa) [106].

density increase was only observed if the density of the pre-densified Si_3N_4 prior to HIPing was higher than 93% th.d. Second, the strength data after HIPing are dependent on the type of pre-sintered Si_3N_4. The α/β-Si_3N_4 phase composition and the grain morphology of the pre-densified material are thought to be decisive parameters for controlling strength values. Third, the use of nitrogen as the pressurizing gas led to higher densities and higher strength values than those obtained using an argon atmosphere because high-pressure nitrogen gas suppressed the decomposition of Si_3N_4. Additionally, the results are dependent on the process parameters, as demonstrated in Figs 26 and 27 [106]. Fig. 26 gives density and strength values as a function of pressure for different temperatures. For the pre-sintered material used, complete post-densification was achieved with a HIP-pressure of 10 MPa, which was nearly independent of the HIP temperature. The resulting mechanical properties, however, are markedly influenced by the HIP temperature. This is explained by insufficient suppression of the Si_3N_4 decomposition. Fig. 27 shows the influence of HIP temperature on density, flexural strength and $\beta/(\alpha + \beta)$ phase ratio. About 1500° C is sufficient for complete densification of this material (Y_2O_3–Al_2O_3–MgO-fluxed), the flexural strength, however, runs through a maximum. Increasing flexural strength is consistent with increasing β-Si_3N_4 amount and the formation of rod-like, interlocked grains. The drop at high HIP temperatures seems to depend on grain coarsening and globularization. Thus, also for post-HIPing, a careful correlation of the characteristics of the starting material, process conditions and resulting microstructure and properties is necessary.

Recent investigations on fracture strength, fracture toughness and microstructural changes after post-HIPing of pre-sintered Si_3N_4 permit the conclusion to be drawn that the filling of residual pores and the healing of cracks and flaws are dominating factors [57]. As a consequence, this technique may be used to reduce property scatter and to improve the reliability of components. An improvement of the absolute data, however, is limited in many cases due to grain growth and globularization effects during post-HIPing [57].

4.3. Properties of dense Si_3N_4 ceramics: data and microstructural effects

A summary of various properties of dense and reaction-bonded Si_3N_4 is presented in Table I. In this Section the values of the main thermo-mechanical and thermo-physical properties, which have been achieved using various processing techniques, but particularly the interdependence of microstructural characteristics are outlined. The usual interdependence between microstructural variables, such as total porosity or macropore size, and properties are only mentioned briefly. The correlation of the typical microstructural characteristics of Si_3N_4 (in the case of dense Si_3N_4 the amount and morphology of the β-phase as well as the type and amount of the grain-boundary phase; in the case of reaction-bonded Si_3N_4 — see Section 5.3 — the amount and morphology of the α-phase, and the size of the micropores) and various properties are

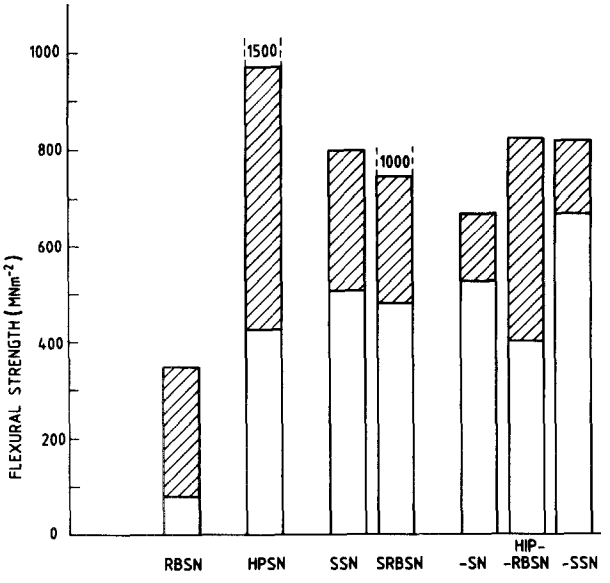

Figure 28 Fracture strength (RT) of various types of Si_3N_4 [107]. The scatter in each material group represents the results of various grades.

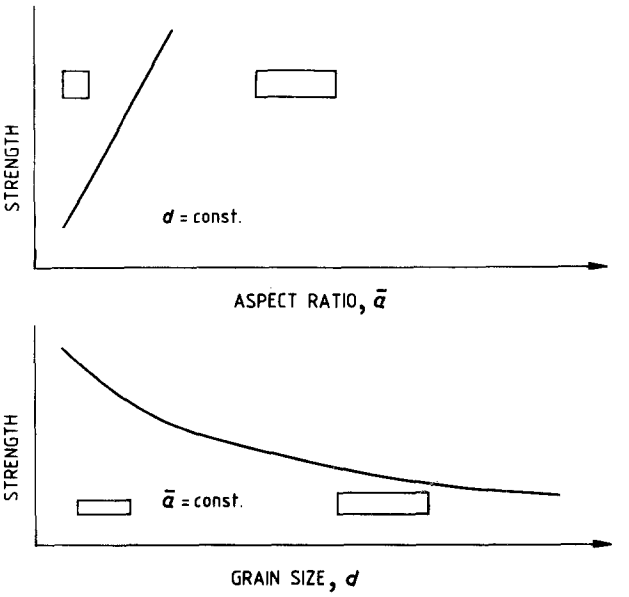

Figure 30 Influence of two typical microstructural variables of dense Si_3N_4, the aspect ratio and the grain size of the β-phase, on the mechanical properties at room temperature (schematic plot) [7].

discussed. As mentioned above, these microstructural parameters are strongly influenced by the properties of the starting powder, by the manufacturing technique and by processing parameters.

In order to separate the influence of different microstructural characteristics, it is necessary to produce materials with well defined microstructures in which various microstructural parameters are isolated as much as possible. This can be done by variation of powder properties and processing conditions. Thus, the systematic investigation of the interrelation between powder properties, processing conditions and microstructural development is the basis for the correlation of microstructural characteristics and thermomechanical properties. This point naturally implies the detailed (if possibly quantitative) characterization of microstructure with different methods.

4.3.1. Mechanical properties below about 1000° C

Fracture stress and fracture toughness data of various types of Si_3N_4 (including a large number of commercial materials and laboratory grades) are shown in Figs 28 and 29. These results clearly indicate that both properties exhibit large variations. Typical average room-temperature strength values of HPSN are 650 MN m^{-2} (MgO-fluxed) and 800 MN m^{-2} (Y_2O_3-fluxed) (for four-point bending and specimen dimensions 3.5 mm × 4.5 mm × 45 mm), maximum values of up to about 1200 MN m^{-2} were achieved by some working groups (but with smaller specimen dimensions and in three-point bending) [108, 109]. Values of Weibull modulus, m, of up to 30 and of fracture toughness, K_{Ic}, of more than 8 MN m$^{-3/2}$ have been obtained. Strength and toughness values at room temperature of SSN have been improved recently to give values similar to HPSN, e.g. σ_F = 800 MN m^{-2} and K_{Ic} = 8 MN m$^{-3/2}$. The room-temperature strength of certain SRBSN grades exceeds 700 MN m^{-2}. There are only a limited number of strength data of hot-isostatically pressed materials which exhibit a strong dependence on the type and amount of sintering additives. In general, relatively high room-temperature strengths and high values of the Weibull modulus, m, have been observed by all HIP-routes; but this area is still under investigation [8].

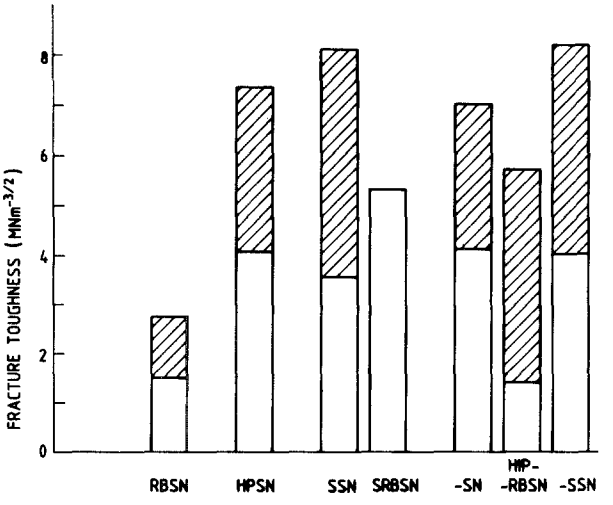

Figure 29 Fracture toughness of various types of Si_3N_4 [39]. The scatter in each material group represents the results of various grades.

The reason for these significant variations in mechanical properties (and also thermal properties and thermal shock resistance) is that various microstructural characteristics have an important influence on these properties. The mechanical properties of dense Si_3N_4 materials at room temperature are mainly controlled by two microstructural parameters: by the elongated β-grains, which can be characterized by the average aspect ratio, $\bar{a}$, ($\bar{a}\uparrow \rightarrow \sigma_F\uparrow$) and by the overall grain size d ($d\uparrow \rightarrow \sigma_F\downarrow$) (see Fig. 30). This is demonstrated by experimental data in Fig. 31 which shows the changes in flexural strength and fracture toughness as a function of hot-pressing time. A significant increase of about 50% is observed both in flexural strength and in fracture toughness with increasing

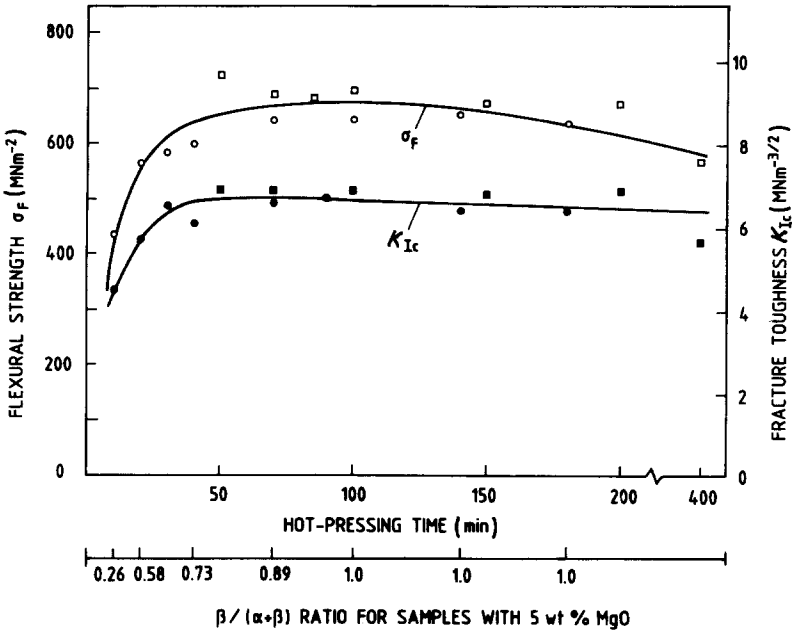

Figure 31 Fracture strength and fracture toughness as a function of hot-pressing time [7]. (○, ●) 5 wt % MgO, (□, ■) 10 wt % MgO.

β-content, this means with increasing time during the first stage of hot-pressing while the density is nearly constant. After complete α/β conversion for long pressing times a decrease in strength occurs. Quantitative microstructural characterization of different types of dense Si_3N_4 and the interdependence of microstructural characteristics with mechanical properties permit the conclusion to be drawn that the major factor controlling fracture strength and fracture toughness up to temperatures of about 1000° C is the aspect ratio of the β-grains (see e.g. Fig. 18). The influence of grain size on fracture strength has been found to be smaller (see Fig. 30). The reason for this is that the linked elongated β-crystals provide higher resistance to crack growth because of the absorption of energy, crack deflection and pull-out effects. Nevertheless, there are some indications that other parameters, such as the amount and properties of the glassy phase, also have an influence on room-temperature strength. As a consequence, a further optimization of mechanical properties at temperatures of up to about 1000° C can be achieved with microstructures consisting of β-grains with high aspect ratios associated with small grain sizes. The aspect ratio and the grain size can be affected by the type and composition of the sintering aid and by variation of the process parameters [59, 60, 63–65, 110]. This is demonstrated by the higher strength values of Y_2O_3-fluxed materials compared to MgO-fluxed Si_3N_4.

Additionally it should be noted that in the case of hot-pressing the orientation effect causes a difference in mechanical properties measured parallel and perpendicular to the hot-pressing direction ($\sigma_\perp > \sigma_\parallel$) [6].

4.3.2. Mechanical properties at high temperatures

High-temperature properties are strongly affected by the nature of the grain-boundary phases. Because of the softening of the glassy phase at higher temperatures, for most sintering additives a decrease in strength, creep and oxidation resistance has been observed at temperatures above 1000° C (Figs 32 to 34). Thus, depending on powder properties, processing and, in particular, the type and amount of sintering additives a wide variety of high-temperature properties can be obtained.

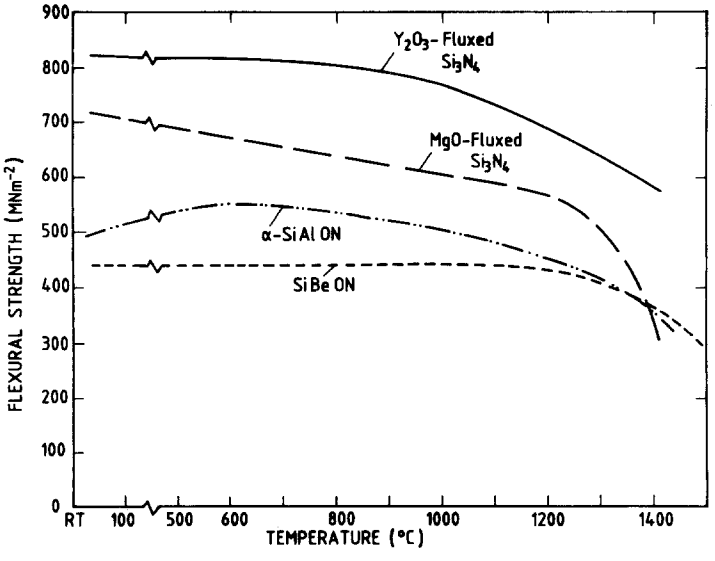

Figure 32 High-temperature flexural strength of various Si_3N_4 ceramics as a function of temperature [39].

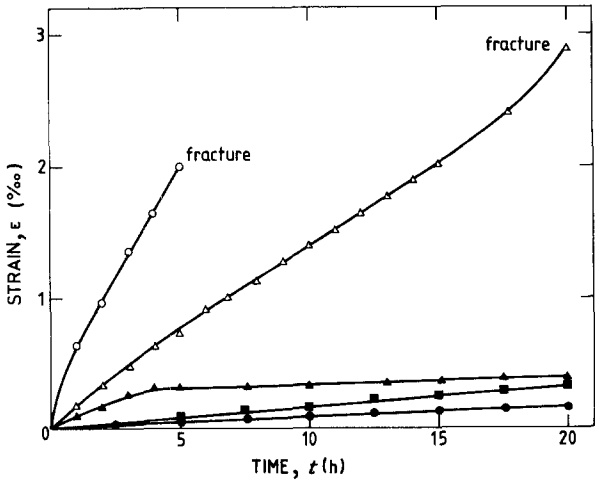

Figure 33 Total strain as a function of time during creep experiments for Si_3N_4 ceramics with different types and amounts of additives: MgO (△ 3 and ○5 wt %) and Y_2O_3 (■ 1.4; ▲ 4.2 and ● 7.0 wt %) [111]. Temperature = 1350° C, stress 100 MN m^{-2}, air.

4.3.2.1. Flexural and tensile strength. Flexural and tensile strength usually decreases at temperatures > 1000° C depending on the parameters discussed above (see upper two curves in Fig. 32) [39]. Because of the lower softening temperature of glassy Mg–Si–O–N phases compared with Y–Si–O–N phases, the drop in high-temperature strength with MgO-doped materials occurs at lower temperatures than those which are Y_2O_3-doped. Besides the softening behaviour, the different tendency of both phases to form crystalline compounds seems to be important, as by this mechanism the amount of glassy phase is reduced, e.g. in Y_2O_3-doped Si_3N_4. Comparing differently processed Si_3N_4 materials, hot-pressed and HIPed Si_3N_4 grades have at present superior high-temperature strengths compared to those of sintered Si_3N_4 as complete densification is achieved with lower amounts of additive or more refractory additives. Up to now, the best strength values above 1350° C are reported for gas-pressure sintered and hot-pressed SiBeON [96].

Of much more practical significance than these short-term strength values is the long-term behaviour.

4.3.2.2. Creep behaviour. The creep behaviour of dense Si_3N_4 at high temperatures, which is usually characterized by a three-stage $\varepsilon = f(t)$ curve, is mainly controlled by grain-boundary sliding along the amorphous phase. The accompanying processes of accommodation are described in the literature as grain-boundary separation, pore formation or cracking [112–115]. In the Si–Mg–O–N system, diffusional creep, the generation of voids during creep and hardening effects due to compositional changes induced by oxidation, have also been observed [6]. Diffusional creep with a stress exponent of 1 was determined for low concentrations of the amorphous secondary phase. At higher concentrations, voids are generated and a stress exponent of > 1.5 was measured. The observation that during oxidation impurity ions such as Mg^{2+} and Ca^{2+} diffuse from the interior to the surface leads to a hardening effect resulting in a

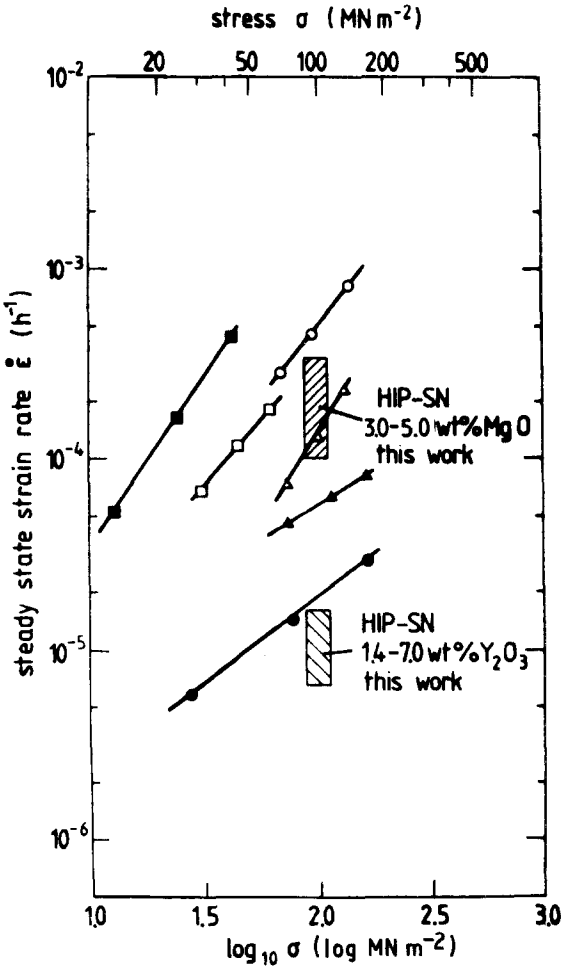

Figure 34 Stress dependence of the strain rate of different Si_3N_4 grades [111]; literature data for comparison from [11]. Temperature = 1350° C; atmosphere, air; bending. HPSN: (○) Norton NC-132 (~ 1 wt % MgO), (□) Ceradyne 147 A (~ 1 wt % MgO), (△) Norton HS-130 (~ 1 wt % MgO), (■) Ceradyne 147 Y–1 (8 wt % Y_2O_3), (▲) Norton NZX-34 (8 wt % Y_2O_3), (●) Ceradyne 147Y (15 wt % Y_2O_3).

decrease of the creep rate after oxidation [6]. In addition to the amount of the amorphous phase, its viscosity plays an important role. Experimental work at a temperature of 1350° C and a constant stress of 100 MN m^{-2} shows that Y_2O_3-doped materials have lower creep rates than MgO-doped grades [111] (Fig. 33). This observation can again be explained by the fact that Y_2O_3-containing amorphous phases have higher viscosities than compositions in the Si–Mg–O–N system [69, 116] and that Y_2O_3-based phases tend to crystallize on cooling from the sintering temperature, thus lowering the residual amount of amorphous phase.

In addition to the volume fraction, the viscosity of the amorphous grain-boundary phase and to the applied stress, the grain size and grain shape have an influence on the creep rate. As long as grain-boundary sliding and diffusion are regarded as the deformation mechanisms, the creep rate would be expected to decrease in inverse proportion to the grain size. In reality the rod-like shape of the β grains also plays a role.

The determination of strain at different stress levels allows the stress dependence of the steady state strain rate, $\dot{\varepsilon}$, at constant temperature to be calculated. An

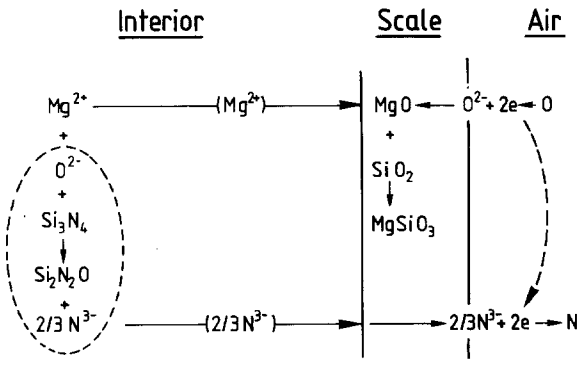

Figure 35 Schematic reaction mechanism for magnesium diffusion in response to a SiO_2 scale formed on the surface of a silicon nitride alloy containing an intergranular phase [121].

example is given in Fig. 34, comparing the values shown in Fig. 33 with data from the literature. With one exception, the favourable effect of Y_2O_3-doped materials compared with MgO-doped Si_3N_4 can be seen. The slope of these plots represents the stress exponent, n, discussed above.

4.3.2.3. Oxidation. Oxidation of pure Si_3N_4 in principle may occur by two mechanisms, depending on the oxygen partial pressure [117]. The so-called "active" oxidation takes place at low oxygen concentrations, leading to volatilization of e.g. SiO, associated with weight loss. "Passive" oxidation, however, which occurs at higher oxygen levels in the atmosphere results in the formation of a "protective" layer and may be represented by

$$Si_3N_{4(s)} + 3O_{2(g)} \rightarrow SiO_{2(s)} + 2N_{2(g)} \qquad (10)$$

Processes taking place are much more complex depending in particular on the composition of the material. Various investigations [117–120] have shown that the reaction is diffusion-controlled and can be described by the parabolic function

$$(\Delta G/A)^2 = K_p t \qquad (11)$$

where $(\Delta G/A)$ is the weight gain per unit area, t is the oxidation time and K_p is the parabolic rate constant. The latter is mainly influenced by temperature, the type and amount of additives and impurities. In MgO-fluxed materials it has been demonstrated that diffusion of magnesium-cations and impurities from the inside of the sample towards the surface via the intergranular amorphous secondary phase is the rate-controlling mechanism [121, 122]. This result has been explained by a gradient in chemical potential which is formed between the silica produced at the oxide scale/sample interface and the intergranular phase, leading to the outward diffusion of Me-cations. The general mechanism is presented in Fig. 35 [121]. Thus, a depletion of Me-cations occurs in the intergranular phase. The oxygen released is thought to react with Si_3N_4 to form Si_2N_2O and nitrogen anions. The latter diffuse to the oxide scale associated with the Me-cations in order to ensure charge balance, and are subsequently released at the surface. This may lead to the formation of bubbles. The rate of these processes in MgO-fluxed Si_3N_4 depends mainly on the amount

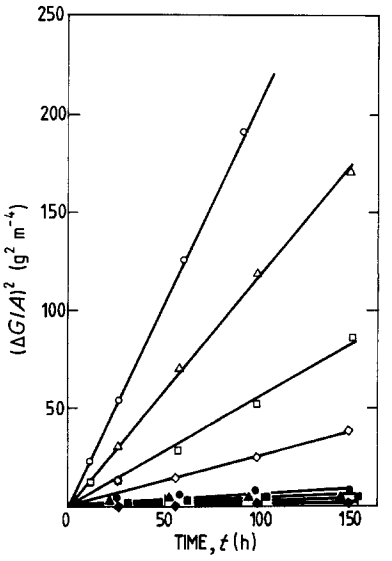

Figure 36 Weight gain during oxidation as a function of time for Si_3N_4 ceramics with different types and amounts of additives. MgO (wt %): (◇) 0.5, (□) 1.0, (△) 3.0, (○) 5.0. Y_2O_3 (wt %): (◆) 0.7, (■) 1.4, (▲) 4.2, (●) 7.0 [111]. Temperature = 1350° C; atmosphere: air.

of the additive present, as shown in Fig. 36 [111]. In Y_2O_3-doped materials, less glassy phase forms because crystalline phases appear simultaneously with oxidation. Additionally, the residual glassy phase is usually more viscous than that in the MgO-doped samples due to the higher eutectic temperatures. Either of those two events cause or slow-down the weight increase. There exists, however, one problem with Y_2O_3-doped materials, the so-called "catastrophic" oxidation. This type of oxidation occurs, if a large amount of mellilith ($Y_2Si_3O_3N_4$) or ternary Y–Si–O–N phases (J-, H-, K-phase) has been formed during processing. These phases show a very high volume increase by oxidizing to yttria silicates (up to 35 vol %) which may lead to total disintegration of the samples [86]. By avoiding high Y_2O_3/SiO_2 ratios in the starting composition, the creation of these phases can be prevented.

Improvement of the oxidation resistance is generally achieved by using highly pure starting powders as well as additives which lead to relatively high viscosities of the secondary phase. In fact, good accordance has been found between the densification and the oxidation rate: additives forming low viscous liquid phases provide high densification rates but low oxidation resistance and vice versa [122]. Additionally it should be mentioned, that compositions forming solid solutions (e.g. SiAlONs) often show improved oxidation resistance, probably due to the relatively high oxygen level already present in the material. Also with these materials, oxidation is controlled by the outward diffusion of additives and impurities, leading to parabolic kinetics [120].

4.3.2.4. Development lines. To improve the high-temperature properties of dense Si_3N_4, it is essential to reduce the glassy phase or to modify the grain-boundary characteristics to produce more stable phases. Different approaches are being followed to make progress in this area.

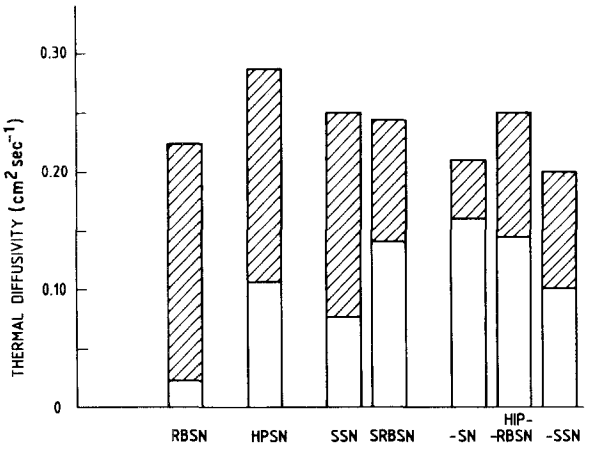

Figure 37 Thermal diffusivity (RT) for various types of Si_3N_4 [107]. The scatter in each material group represents the results of various grades.

(i) Reduction of the additive and impurity concentration in the starting composition coupled with the application of higher pressures (e.g. by HIPing or gas-pressure sintering).

(ii) Use of densification aids with high solidus temperatures and high viscosities which have the tendency to form refractory phases by crystallization.

(iii) Conversion of the amorphous phase to crystalline phases on cooling or during subsequent annealing.

(iv) Selection of a composition where the sintering aids are dissolved in the Si_3N_4 lattice to form a single-phase system, or which enables the elimination of the liquid phase by vaporization during extended heat treatment.

The efforts to optimize the grain-boundary characteristics are summarized under the term "grain-boundary engineering" [123]. Examples of the improvement of the high-temperature properties are the grain-boundary crystallization, as in the case of Y_2O_3 as densification aid, or the elimination of the grain-boundary phase by the formation of β-solid solution by using additives, such as alumina or beryllium compounds [124, 125] (SiAlONs and SiBeONs – see Fig. 32 and Section 4.2). The latter materials partly have good high-temperature strength and good oxidation resistance compared to other materials. One disadvantage of these materials, however, has been the relatively low room-temperature strength. By using the approaches of solid-solution formation and crystallization of the residual amorphous phase, recent developments have shown that this disadvantage can be overcome. Special Y–Si–Al–O–N compositions were fabricated with room-temperature strength of about 700 MN m^{-2} which remains constant up to about 1100° C and drops to about 500 MN m^{-2} at 1400° C [126, 127]. This result demonstrates that grain morphology, grain size (for high strength values up to 1000° C) and grain-boundary characteristics (for good high-temperature properties) have to be optimized.

4.3.3. Thermal and thermo-mechanical properties

4.3.3.1. Thermal diffusivity/conductivity. A summary of thermal diffusivity data* as one example of the thermal properties, of various types of Si_3N_4 (including also a large number of commercial materials and laboratory grades) is shown in Fig. 37 [107]. These results demonstrate that thermal properties also exhibit large variations which are mainly caused by microstructural effects.

Thermal diffusivity/conductivity of dense Si_3N_4 is mainly controlled by the phase composition (the β-content and the amount of glassy phase), by solid solution and, in the case of hot-pressing, by orientation effects. A summary of systematic investigations of various microstructural effects is given in Fig. 38. As an example, Fig. 39 shows thermal diffusivity data as a function of hot-pressing time and the proportion of β-phase present. The α to β transformation with increasing hot-pressing time results in a significant

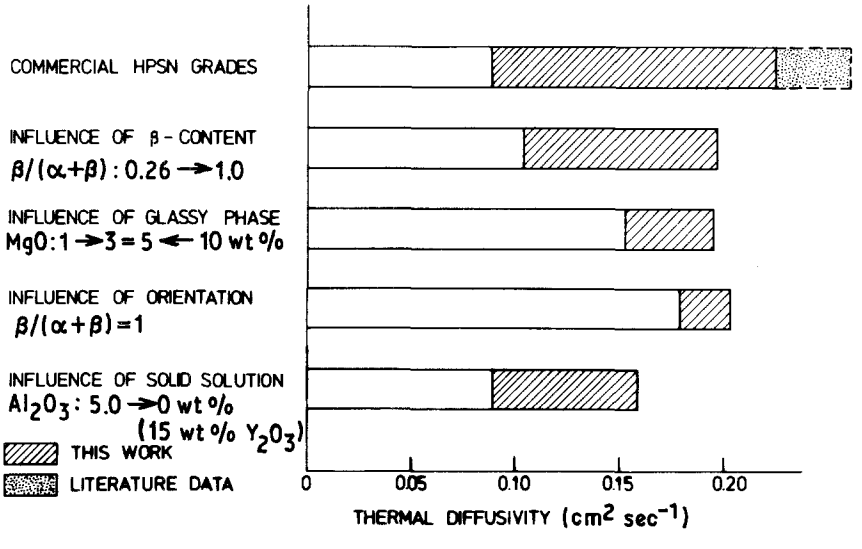

Figure 38 Influence of various microstructural characteristics on the thermal diffusivity of dense Si_3N_4 [128].

*Thermal diffusivity, a, is defined by the expression $a = \lambda/(\varrho c_p)$ in cm^2 s^{-1}, where ϱ is the density of the material in g cm^{-3}, and c_p the specific heat in J kg^{-1} K^{-1}. On the basis of this definition, thermal conductivity can be computed from diffusivity data if the density of the material and the specific heat are known. From calorimetric measurements of the specific heat of different Si_3N_4 materials with different phase compositions, sintering additives and grain structure it may be concluded that the specific heat of Si_3N_4 is independent of microstructural effects.

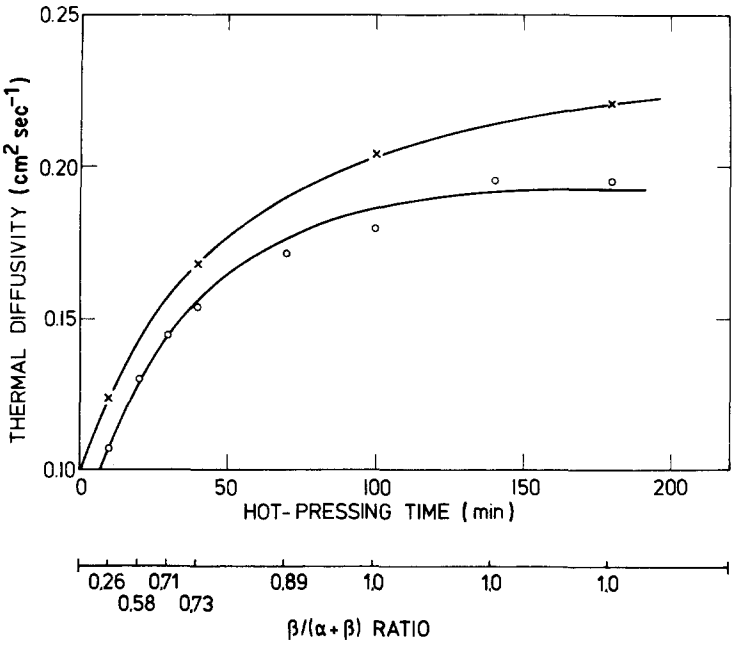

Figure 39 Influence of the amount of β-phase, varied by the hot-pressing time, and of the hot-pressing direction on thermal diffusivity of hot-pressed Si_3N_4 [128]. 5 wt % MgO, T = 1700° C. (×) Perpendicular, and (○) parallel to HP direction.

increase in the room-temperature diffusivity. It is suggested that this effect arises because the thermal conductivity of the β-phase is higher than that for the α-phase. Moreover, a strong orientation effect on thermal diffusivity is observed. The reason for this is that the elongated β-grains exhibit a preferred orientation in such a way that their direction of elongation, which coincides with the crystallographic c-axis of the hexagonal β-phase, is oriented perpendicular to the hot-pressing direction. This preferred orientation has been shown to result also in a pronounced anisotropy in strength and fracture toughness. Moreover, thermal diffusivity/conductivity of dense Si_3N_4 is influenced by other microstructural parameters, such as the amount of glassy phase and solid solution effects (Fig. 38). For example, maximum values were observed between 3 and 5 wt % MgO. Also an increasing concentration of Al_2O_3 in Y_2O_3-doped dense Si_3N_4 results in a decrease of thermal diffusivity/conductivity [107, 128–130].

4.3.3.2. Thermal shock resistance. Thermal shock resistance of Si_3N_4 ceramics varies widely. This is demonstrated for the critical temperature difference, ΔT_c, after water and oil quench in Figs 40 and 41 [39, 128, 131, 132]. Here, it should be noted that the test-pieces from all quenching experiments clearly showed that unstable crack propagation had occurred for all the grades of dense and reaction-bonded Si_3N_4

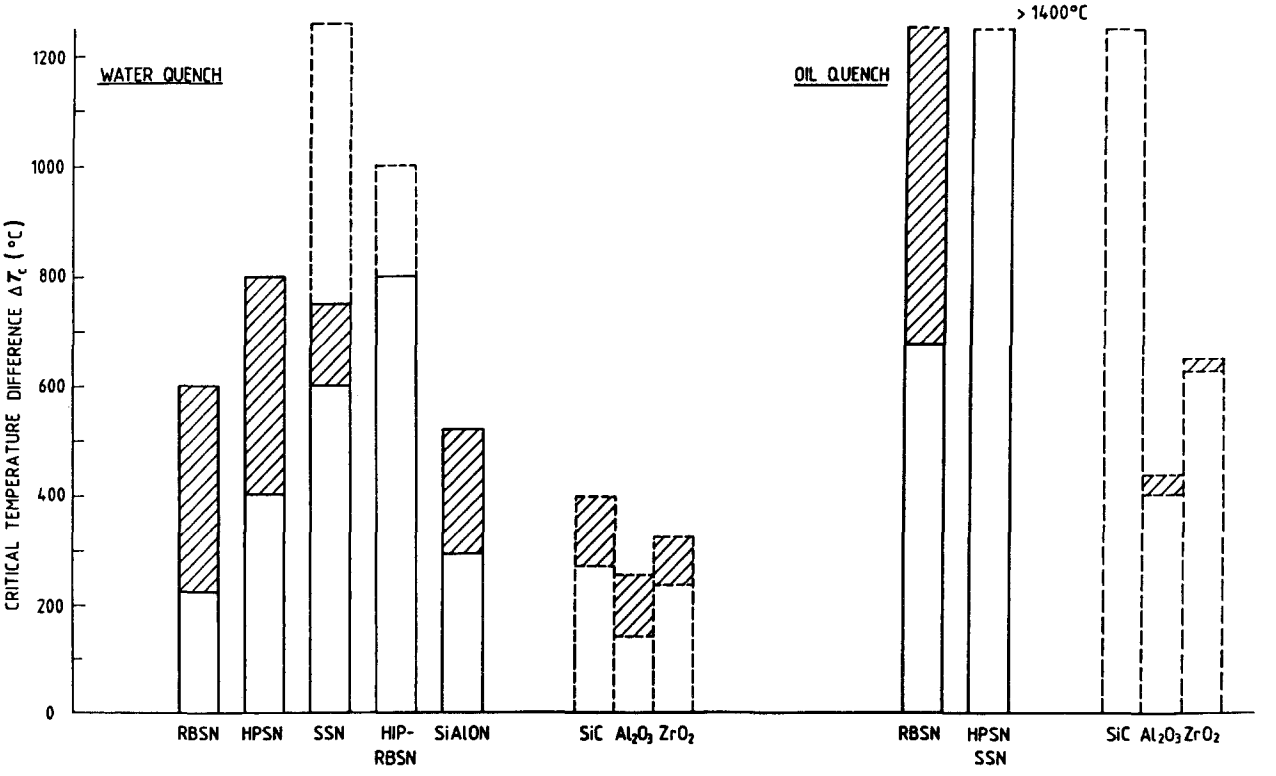

Figure 40 Critical temperature difference, ΔT_c, after water and oil quench (22° C) for various Si_3N_4 ceramics (specimen dimensions 3 mm × 3 mm to 3.5 mm × 4.5 mm to 5 mm × 5 mm; length 45 to 50 mm) [131]. The scatter in each material group represents the results of various grades.

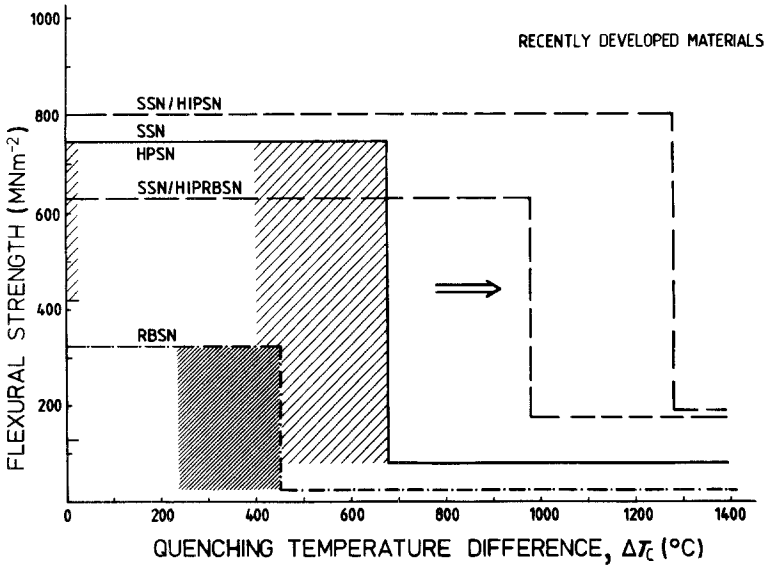

Figure 41 Strength (RT) as a function of quenching temperature difference after water quench (22° C) for various structural ceramics (specimen dimensions 3.5 mm × 4.5 mm to 5 mm × 5 mm, length 45 to 50 mm) [131]. The scatter in each material group represents the results of various grades.

investigated, even for very low-strength materials [131, 133].

As thermal shock resistance of ceramic materials is, in general, controlled by mechanical and thermal properties, particularly the ratio of strength, σ_F, to Young's modulus, E, the coefficient of thermal expansion, α, and the thermal conductivity, λ, the strong microstructural effects on mechanical and thermal properties determine the interdependence of microstructural variables and thermal shock resistance of Si_3N_4 in a rather complex way. The influence of various microstructural characteristics on thermal shock resistance and the relationship of strength and thermal conductivity to the thermal shock resistance parameters R ($R = \sigma_F(1 - \nu)/\alpha E$) and R' ($R' = R\lambda$) for severe and less severe quenching is demonstrated in Table VII. Fig. 42 summarizes the influence of the major microstructural characteristics on the thermal shock resistance to fracture initiation, characterized by a quality factor indicating positive or negative changes. Here, it should be noted that for Si_3N_4 (dense and reaction-bonded Si_3N_4) and the specimen dimensions used in these investigations, the changes in the critical temperature difference, ΔT_c, after water and oil quench can be described by a value between R and R'. Moreover, this graph demonstrates whether the variations in thermal shock resistance are caused by changes in fracture strength or in thermal conductivity.

TABLE VII Influence of microstructural characteristics on thermal shock resistance of dense Si_3N_4 (the increase of the microstructural characteristics leads to the marked changes in properties: ↑ increase; ↓ decrease) [107]

Thermal shock resistance characterized by:

$$R = \frac{\sigma(1 - \nu)}{\alpha E} \text{ and } R' = \frac{\sigma(1 - \nu)}{\alpha E}\lambda$$

α- to β-transformation	$\sigma\uparrow$	$E\downarrow$	$R\uparrow$ $R'\uparrow$
aspect ratio	$\sigma\uparrow$	$E\downarrow$	$R\uparrow$ $R'\uparrow$
β-content		$\lambda\uparrow$	$R\uparrow$ $R'\uparrow$
grain size	$\sigma\downarrow$	$E \approx$ $\lambda \approx$	$R\downarrow$ $R'\downarrow$
MgO content	$\sigma \approx$	$E\downarrow$ $\lambda\uparrow\downarrow$	$R \approx$ $R'\uparrow\downarrow$
solid solution	$\sigma \approx$	$E \approx$ $\lambda\downarrow$	$R \approx$ $R'\downarrow$

Thermal shock resistance to fracture initiation of dense Si_3N_4 is controlled by the changes in mechanical and thermal properties which are strongly influenced by grain morphology, overall grain size and phase composition, that is, the β-content and the amount of the glassy phase. Fracture strength up to about 1000° C is mainly determined by the elongated β-grains (positive effect), and by the grain growth (negative effect). Thermal conductivity is strongly influenced by the β-content and the amount of glassy phase. Results show that the strongest microstructural effect on thermal shock resistance of dense Si_3N_4 is the α to β transformation. Maximum thermal shock resistance of dense Si_3N_4 has been achieved after complete conversion and with small grain sizes. Further improvement can be obtained by optimizing the amount of sintering aids [107, 128, 132, 134].

4.3.3.3. Thermal cycling behaviour. In practice, the thermal cycling behaviour of ceramic materials, under less severe quenching conditions than those to cause a drastic decrease in retained strength, is of great importance. Thermal cycling data of Si_3N_4 are given in Fig. 43. Here, the fracture strength at room temperature retained after thermal cycling as a function of the number of cycles is shown. In these experiments thermal cycling was carried out from a temperature of 1260° C to room temperature. The specimens were quenched in a high-pressure air jet causing a maximum cooling rate of about 80° C sec^{-1}.

Strength of dense and reaction-bonded Si_3N_4 under the applied quenching conditions decreases during thermal cycling. Both types of material exhibit large differences in strength degradation, whereby the strength reduction is usually higher for reaction-bonded Si_3N_4 than for dense Si_3N_4. In spite of the strength loss, dense Si_3N_4 has the highest strength after thermal cycling, compared to the other engineering ceramics [135].

The interpretation of the thermal cycling behaviour of both types of Si_3N_4 is rather complex. The reason for this is that, depending on the thermal cycling conditions as well as the type and characteristics of the materials, a superposition of various effects

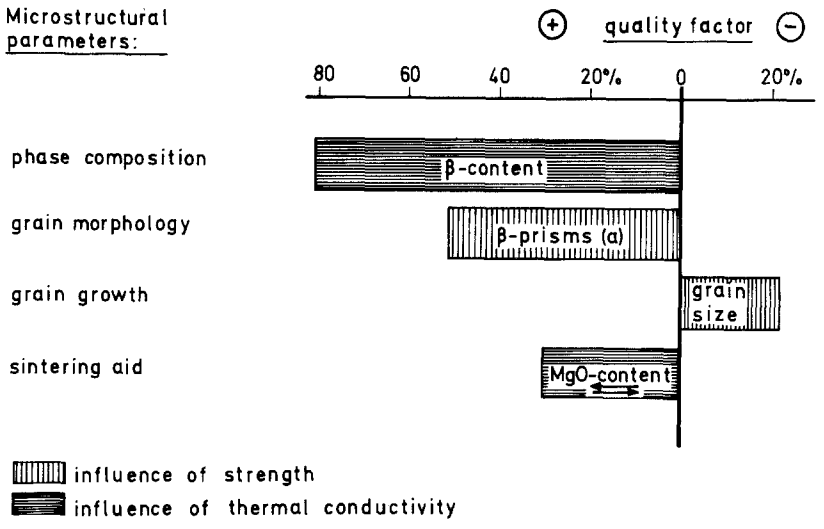

Figure 42 Influence of various microstructural characteristics on the thermal shock resistance to fracture initiation of dense Si_3N_4 [128, 132].

takes place, which include mainly the applied thermal stresses, oxidation processes, crack healing, and rounding off of internal pores and flaws [136]. In the case of dense Si_3N_4, the major factor influencing the thermal cycling behaviour is the effect of oxidation products (formation of sharp microcavities on the surface and/or of surface pits) on fracture strength which is controlled by the grain-boundary characteristics. As a result, the thermal cycling behaviour is dependent on the nature and amount of the additives and on the impurities of the materials. This is demonstrated in Fig. 44. As a consequence, the thermal cycling behaviour of dense Si_3N_4 may be improved by increasing the oxidation resistance.

5. Reaction-bonded silicon nitride

5.1. Formation mechanism and microstructure of reaction-bonded Si_3N_4

According to the following equation systems, reaction-bonded silicon nitride can be formed from its elements [38]:

$$3Si(s) + 2N_2(g) \rightarrow Si_3N_4(s)$$
$$\Delta G^\circ \simeq -723 + 0.315\,T \text{ kJ mol}^{-1} \quad (12)$$

$$3Si(l) + 2N_2(g) \rightarrow Si_3N_4(s)$$
$$\Delta G^\circ \simeq -874 + 0.405\,T \text{ kJ mol}^{-1} \quad (13)$$

$$3Si(g) + 2N_2(g) \rightarrow Si_3N_4(s)$$
$$\Delta G^\circ \simeq -2080 + 0.757\,T \text{ kJ mol}^{-1} \quad (14)$$

Thermodynamic calculations show that silicon can react in all physical conditions with nitrogen in the standard state. Nevertheless, different modifications of silicon nitride are generated with different formation rates. This point will be discussed when considering the reaction kinetics. Reactions 12 and 13 are valid only up to temperatures near the melting point of silicon. It is proposed in literature, that the major growth of β-Si_3N_4 during the formation of RBSN occurs in the liquid phase and, to a minor extent, as the result of the reaction between solid silicon and nitrogen. The α-modification is mainly formed by a gas-phase reaction between gaseous silicon and nitrogen according to Reaction 14 [38, 137–142]. The reaction between silicon monoxide and nitrogen according to Equation 15

$$3SiO(g) + 2N_2(g) \rightarrow Si_3N_4(s) + \tfrac{3}{2}O_2(g) \quad (15)$$

is also often discussed concerning the formation of the α-phase, although ΔG° for Reaction 15 is positive under standard conditions. The reason for this is the fact that the presence of hydrogen in the nitriding gas can influence the partial pressure of SiO and O_2, and thus the equilibrium constant of this equation.

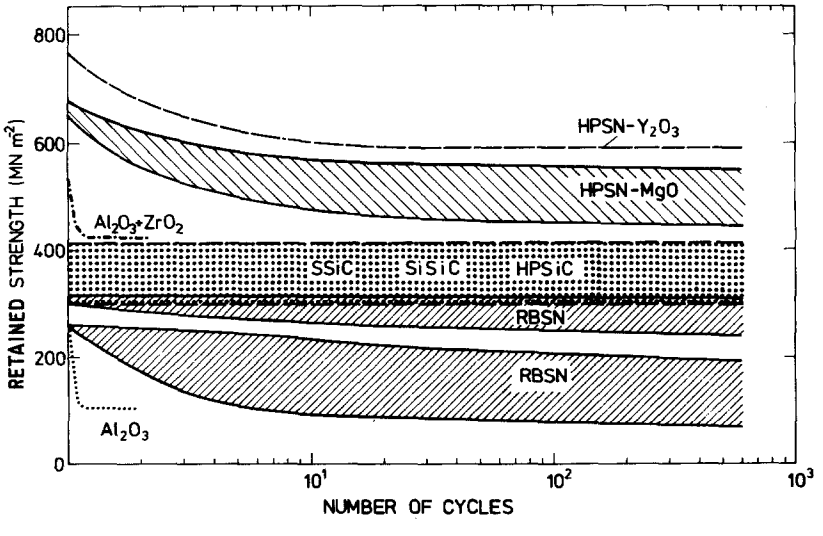

Figure 43 Strength behaviour of HPSN and RBSN and other high-strength engineering ceramics after thermal cycling (the scatter in each material group represents the results of various grades) [135]. T_F = 1260° C → RT (cooling rate 80° C sec^{-1}).

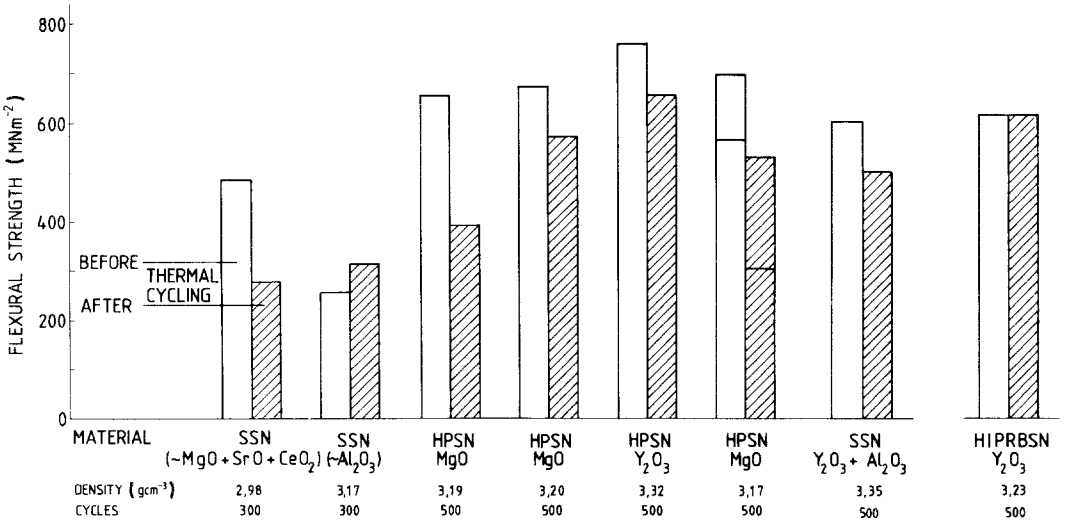

Figure 44 Thermal cycling characteristics of various dense Si_3N_4 grades [135]. T_F = 1260° C → RT (cooling rate 80° C sec^{-1}).

Therefore, Reaction 15 can become important during the nitridation of silicon as proposed by Lindley *et al.* [143].

These processes may be used either to produce Si_3N_4 powder (see Section 4.2) or RBSN bodies. One important factor with the latter is that the volume expansion of approximately 22 vol % connected with the conversion of silicon to Si_3N_4 leads to a decrease in total porosity without any marked change in overall dimensions. The RBSN formation and the resulting microstructural development are affected by several factors: mean particle size and size distribution as well as the nature and distribution of impurities in the starting silicon powder, the method of fabrication which affects the packing of particles, and the nitriding conditions, e.g. gas composition, gas pressure, temperature, time and heating rate.

5.1.1. Formation of the α-phase

The α-phase consists of α-whiskers and the very fine-grained so-called α-matte.

5.1.1.1. α-whiskers. The α-whiskers, preferably formed on sample surfaces, are in the form of long thin fibres with diameters ranging from 0.05 to 0.2 μm and an inner crystalline core, surrounded by a thin amorphous layer [144, 145]. Many of these whiskers have a spherical origin which frequently contains impurities like iron [137]. So it is concluded that these α-whiskers are formed through a vapour–liquid–solid mechanism [138]. A schematic illustration of this process is given in Fig. 45. Iron can decrease the melting temperature of silicon by as much as 200° C. Nitrogen is transported to the whisker origin where it condenses in the liquid. This nitrogen reacts at the solid–liquid interface to form silicon nitride and to contribute to the growth of the needles [138].

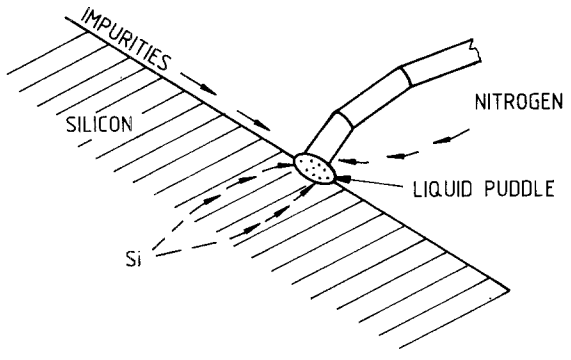

Figure 45 Schematic illustration showing the possible mechanism for the formation of α-needles with liquid phase on the surface of a silicon grain [138].

5.1.1.2. α-matte. To explain the formation mechanism of the α-matte, the following model is generally accepted [139, 140]. At the beginning of the reaction between silicon and nitrogen, silicon nitride nuclei are formed at the silicon surface through chemisorption (Fig. 46). To these nuclei, silicon is transported through evaporation–condensation or surface diffusion from the vicinity of the nuclei. At the same time, the nitrogen concentration in the nuclei's close

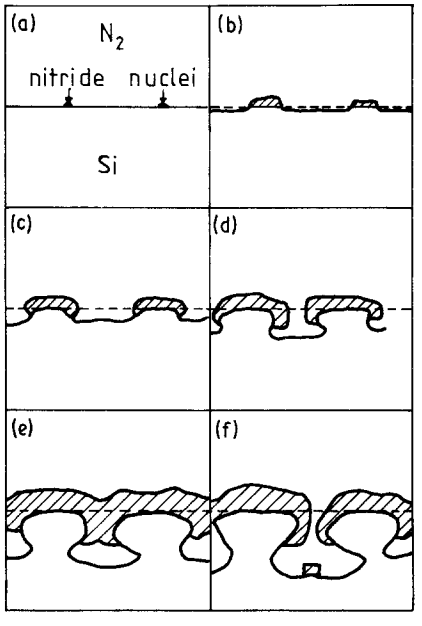

Figure 46 Suggested nitride growth sequence [139]. (a) Formation of Si_3N_4 nuclei, (b) lateral growth of nuclei, (c) depression of the uncovered silicon surface by silicon removal, (d) nitride growth around depression edges, (e) sealing of the silicon-surface or (f) forming new nuclei inside pores.

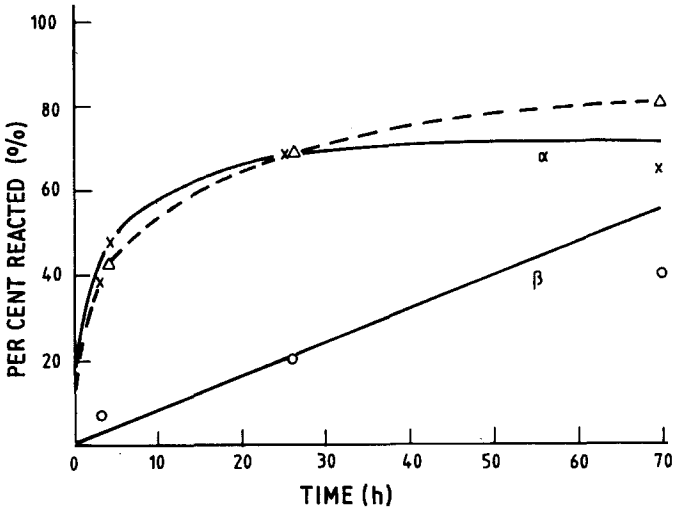

Figure 47 Formation kinetics of (x) α- and (○) β-Si_3N_4 (the α-Si_3N_4 formation approximately obeys the expected rate law) [138]. 99.99% pure powder. Gas flow rate = 65.5 $cm^3 min^{-1}$, heating rate = 350° C h^{-1}, temperature = 1500° C. (△) $[1 - (1 - x)^{1/3}]^2 = D'K''t^{2/3}/r^{7/3}$. D = diffusion constant; K = constant; t = time; r = radius of spheres; x = fraction already reacted.

vicinity (where silicon evaporates) becomes too low to form new nuclei. With increasing growth of the nuclei a dense silicon nitride layer is formed and pores are generated at the places where silicon has evaporated or diffused away. In these newly formed pores the nitrogen, which has diffused in, reacts with silicon or silicon monoxide in the gas phase. Because of the volume expansion occurring during this reaction, these newly formed pores can be completely refilled with nitride.

5.1.1.3. Reaction kinetics of the α-phase. If, after nuclei formation, a silicon nitride layer has formed at the surface of silicon particles, the formation of the α-phase is connected with the diffusion of nitrogen through this nitride layer. Agreement of the calculated curve shown in Fig. 47 and the parabolic correlation (found by experimentation) between the reaction product and the time of reaction confirms that diffusion is the rate-limiting factor [138]. As, in addition to the α-matte, other products may be formed at the same time, the relation as presented above between reaction product and time of reaction can, however, only be an approximation.

5.1.2. Formation of the β-phase

While the α-phase is preferably formed at temperatures below the melting point of silicon through a gas-phase reaction, the β-modification may be formed by the solid–gas reaction between silicon and nitrogen and through diffusion of nitrogen in solid silicon nitride or in the presence of a liquid phase [141, 142, 146]. After the formation of a layer, nitrogen may diffuse through the hexagonal tunnels of the β-crystals to the Si–Si_3N_4 interface and react there with silicon (Fig. 48).

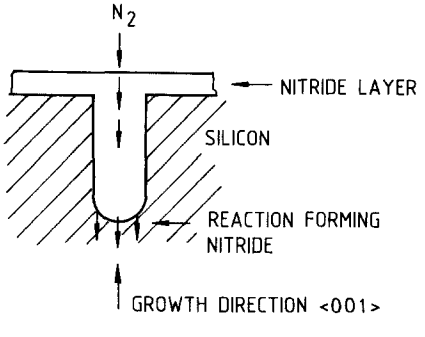

Figure 48 Schematic drawing showing β-spike growth into a silicon grain by diffusion of nitrogen down the hexagonal tunnels in β-Si_3N_4 to the end of the spike where reaction occurs [138].

As a result of the volume expansion accompanying the transformation of silicon into Si_3N_4, new space must be provided for the reaction product. Such space may be generated through new porosity or through a melting of silicon, which explains the high proportion of β-phase formed at nitridation temperatures above the silicon melting point [138]. The assumption that the β-phase is formed in the presence of a liquid phase is also supported by observations that impurities in silicon, which form with the silicon low-melting point eutectics, enhance the formation of the β-modification [142, 146, 147]. As nitrogen can easily diffuse through the large hexagonal tunnels in β-crystals (Fig. 48), it is not diffusion but the reaction at the Si–Si_3N_4 interface which is the rate-controlling step. Hence, the relation between reaction product and time of reaction is linear (Fig. 47).

5.1.3. Microstructure

Based on these mechanisms the microstructure of RBSN consists mainly of the α- and β-phases, unreacted silicon, impurity phases and, in particular,

TABLE VIII Microstructural characteristics of RBSN

Formation mechanism:	
α-phase	gas-phase reaction
β-phase	diffusion process
Porosity:	
total porosity (%)	12–30
open porosity (%)	6–22
size of macropores > 1 (μm)	1–50
size of micropores < 1 (μm)	0.01–0.5
Phase composition:	
α-phase (%)	60–92
β-phase (%)	8–40
unreacted Si (%)	< 5
impurity phases (%)	< 5
Grain structure:	
α-phase (μm)	needle-like: width ~ 0.1–0.3 length ~ 0.5–1
β-phase (μm)	equiaxed: 0.5–5

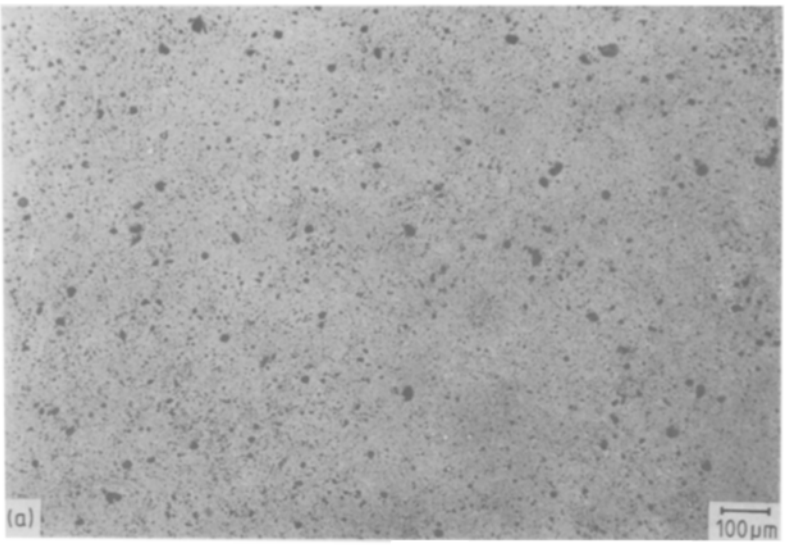

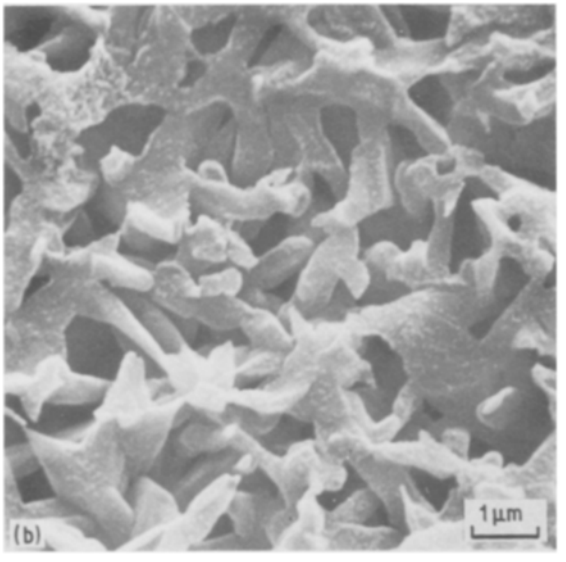

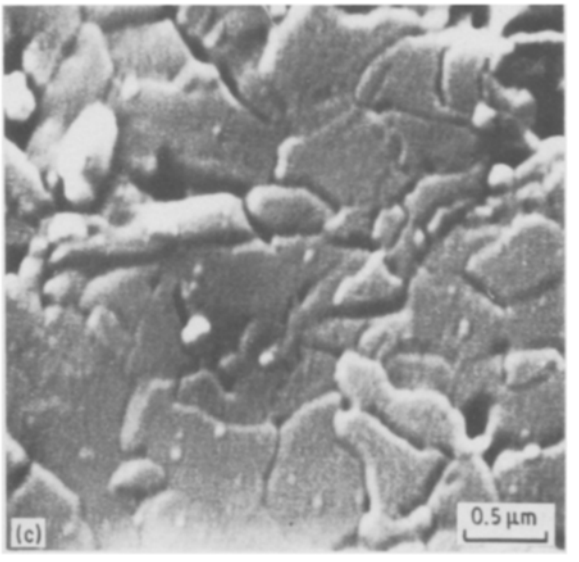

Figure 49 Typical microstructure of RBSN; (a) pore structure on polished microsections (density 2.57 g cm^{-3}), (b) morphology of the α-phase (ion-etched, scanning electron micrograph), (c) morphology of the β-phase (chemically etched, scanning electron micrograph).

macro- and micropores (macropores > 1 µm; micropores < 1 µm). RBSN has a residual porosity of 12 to 30 vol %. The pore structure covers a large range of pore sizes beginning with the very small micropores of 0.01 µm diameter and going as far as macropores reaching diameters of about 50 µm (Table VIII). The micropores are closely connected with the size of the fine α-needles. The β-phase is usually equiaxed (only in some cases are rod-like grains formed, especially in the vicinity of macropores) with grain sizes between 0.5 and 5 µm [24, 148, 149]. Typical microstructures of RBSN are given in Fig. 49 indicating the pore structure, the needle-like α-phase and the equiaxed β-phase.

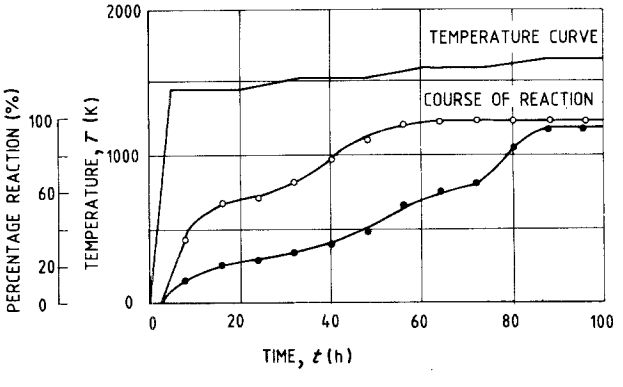

Figure 50 Nitridation of silicon powder compacts with different grain sizes [150]. Starting grain size of silicon powder; (○) < 10 µm, (●) 37 to 63 µm.

5.2. Relationship between powder properties, processing conditions and densification and microstructure of reaction-bonded Si_3N_4

5.2.1. Influence of silicon starting powder properties

5.2.1.1. Grain size. A change in silicon starting grain size leads to a completely changed course of reaction during nitridation. With increasing specific surface area and decreasing grain size of the silicon powder the degree of reaction at low temperatures is increased. This leads to a substantial reduction of the total time of reaction and to a decrease in the necessary final temperature (Fig. 50 [150, 151]).

The different courses of reaction result in great differences in the microstructure.

(a) Macropores. Fig. 51 shows light micrographs of the RBSN samples produced from a coarse (d_{50} = 51 µm) and a fine (d_{50} = 7 µm) silicon powder. At a constant density of approximately 2.4 g cm^{-3},

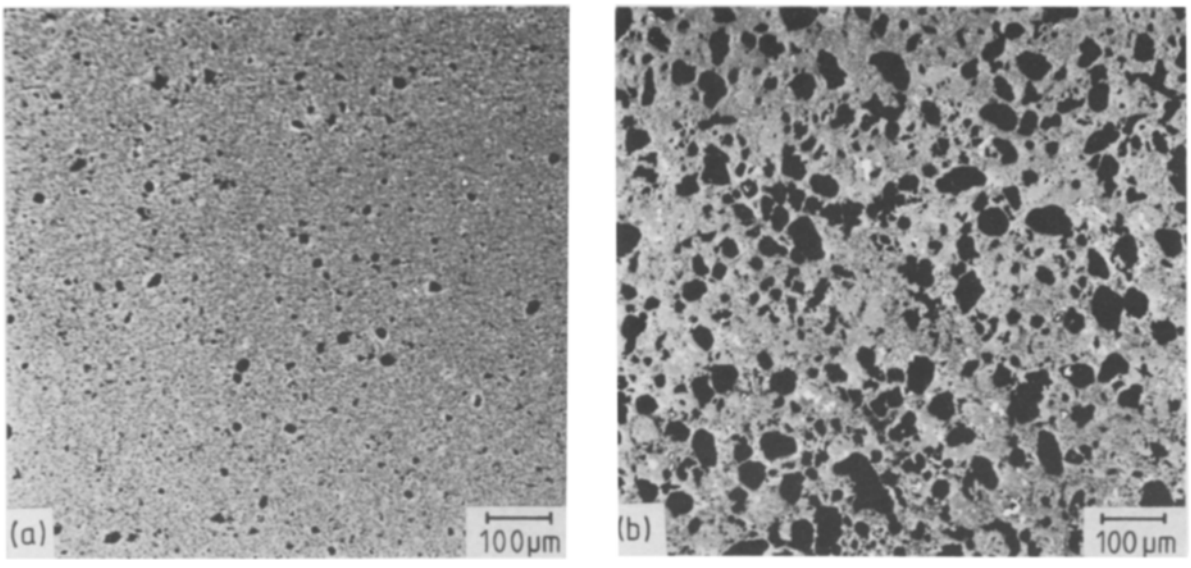

Figure 51 Optical micrographs of RBSN produced from silicon powders with different grain sizes; (a) $< 10\,\mu m$, (b) 37 to $63\,\mu m$ [148].

the pore-size distribution is shifted to larger values with increasing grain size of the silicon starting powder.

(b) Phase composition. With a fine starting powder, the amount of the α-modification is higher than with coarse starting powders. This is attributed to the fact that the larger specific surface of the fine starting powder increases the evaporation rate of silicon. Since the α-modification is formed through a gas-phase reaction between silicon or SiO and nitrogen, an increased amount of the α-modification is obtained with increasing specific surface.

(c) Grain size of the α- and β-phase. Fig. 52 shows the difference in size of the α- and β-grains in two

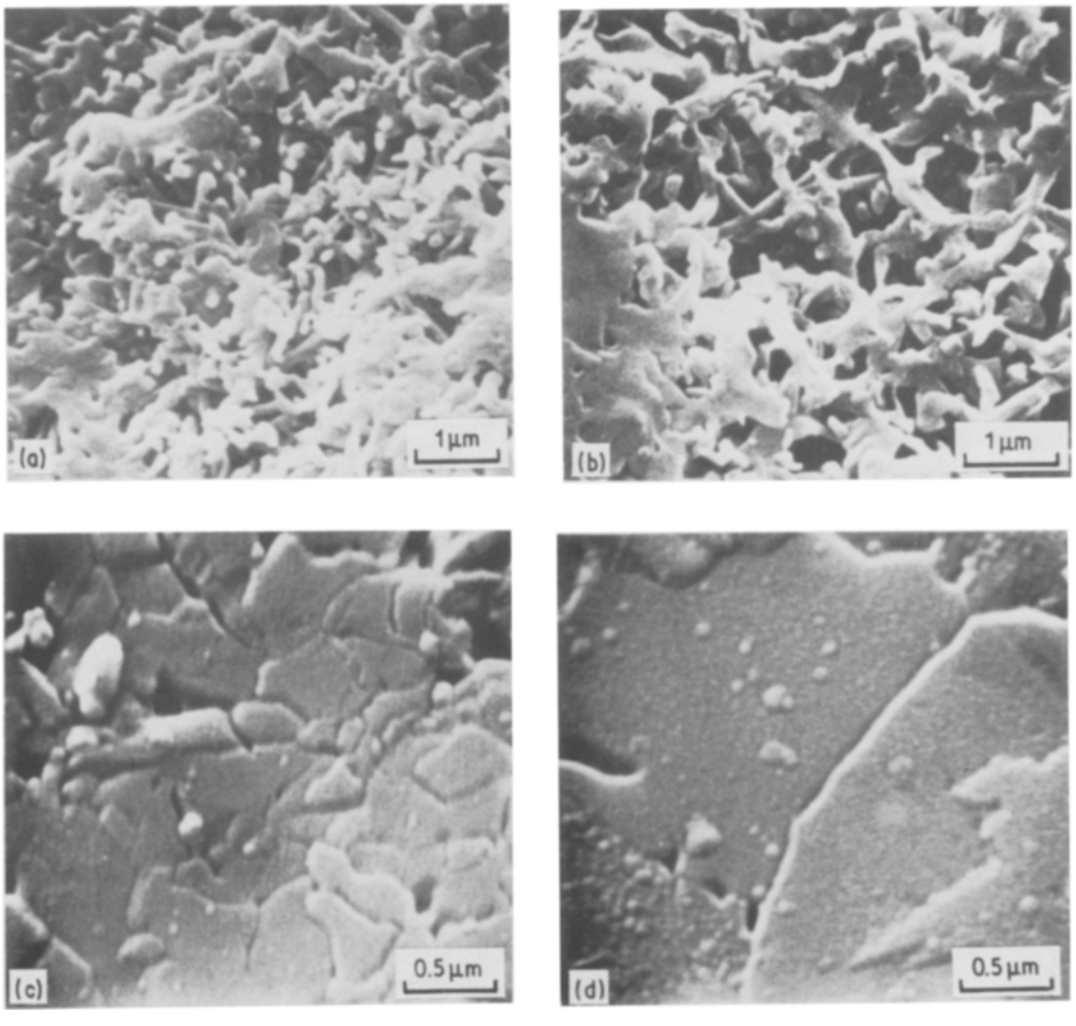

Figure 52 Morphology of the α- and β-phase for RBSN produced from silicon powders with different grain sizes [148]; (a) and (b) α-phase, (c) and (d) β-phase; (a) and (c) initial silicon grain size $< 10\,\mu m$, (b) and (d) initial silicon grain size 37 to $63\,\mu m$.

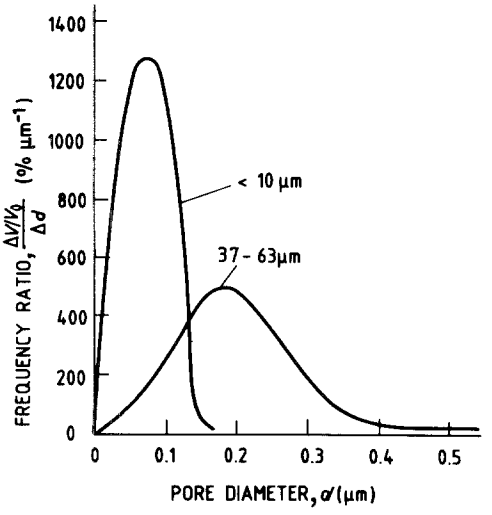

Figure 53 Distribution of micropores in RBSN produced from silicon powders with different grain sizes [152].

materials produced from silicon-powders of different sizes. The needle-like crystals (Figs. 52a and b) of the α-modification result from the formation via the gas phase. Growth of such needles is impeded, if no gaseous reactants are available or if these needles impede themselves during growth. As the coarse-grained material contains larger pores, larger needles can grow. The size of the equiaxed β-grains increase with increasing starting grain size of the silicon powder (Figs 52c and d). The reason for this could be that, due to the formation mechanism of the β-phase (see Fig. 48), from each silicon crystal a silicon nitride crystal could be formed. As the silicon particles may also be composed of several crystallites, the β-grains can be smaller than the particle size of the silicon starting powder.

(d) Micropores. In addition to the macropores which are visible in the light microscope, RBSN contains micropores which can be determined by means of mercury porosimetry. Fig. 53 shows the size distribution of these micropores for two materials prepared from different silicon-powders. A comparison with Figs. 52a and b shows that the micropore size thus determined is in agreement with the pores between the α-Si_3N_4 formed from the gas phase. With increasing silicon particle size the size of the α-crystals increases and therefore the distribution of the micropores is shifted to higher values.

TABLE IX Typical characteristics of a commercial silicon powder

Major impurity elements	wt %
Fe	0.80
Al	0.20
Ca	0.02
C	0.05
O_2	0.40
Mean particle size:	15 µm
Specific surface area:	1.5 $m^2 g^{-1}$

With this respect, a rather strong relation has been found between the particle size distribution and the pore size distribution in the silicon-powder compacts and the grain size and pore size distribution in the resulting RBSN (Fig. 54). Here it is presumed that the chemical composition of the powder is not changed markedly by milling. Decreasing particle size of the silicon-powder leads to smaller pore sizes in the silicon-compact and, finally, to a decrease in the size of micropores in RBSN. Thus, the particle size distribution of the silicon-starting powder determines the characteristics of the micropores in RBSN and, as it is shown, also the mechanical properties [153]. Additionally, it has been demonstrated that the impurity content is important for the morphology of micropores [153].

5.2.1.2. Impurities. As with all technical powders, silicon-starting powders contain certain impurities. Typical characteristics of commercial silicon-powders are shown in Table IX. Many impurities in the silicon powder, such as iron, aluminium, calcium, carbon or oxygen, may affect the course of nitridation and hence frequently also the microstructural development. As during preparation silicon powder is often contaminated with iron, the influence of iron has so far been given the most intensive analysis. Very small additions of iron are known to accelerate the nitridation process (Fig. 55). However, the role which iron plays in influencing the nitridation kinetics has not yet been completely clarified and several mechanisms have been suggested [38, 154]. Iron may act as an inert catalyst to increase the diffusion rate of silicon or it may provide voids, pores, and channels for diffusing atoms via the formation of liquid-phase Fe_xSi_y. It may also act as an oxygen remover either by dissolving

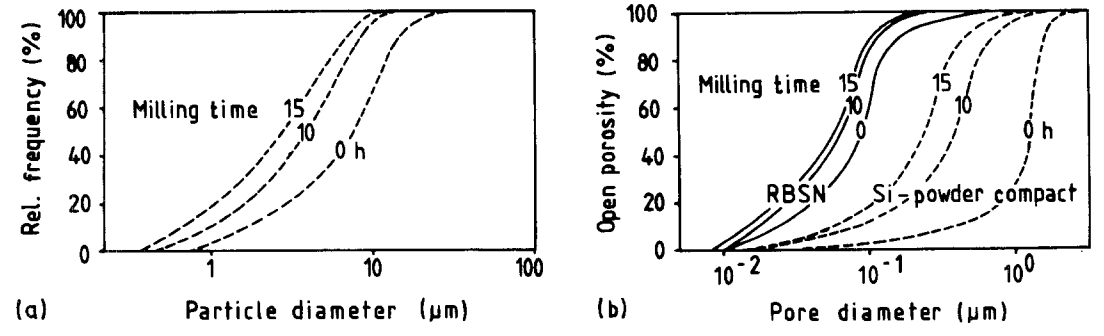

Figure 54 (a) Particle size distributions after different milling times and their relation to (b) pore size distributions in the silicon powder compacts and the resulting RBSN grades [153].

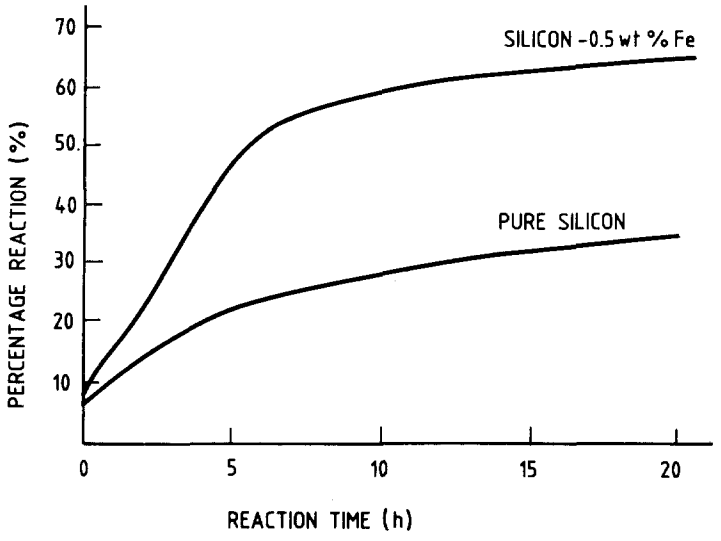

Figure 55 Nitridation of pure silicon and silicon + 0.5 wt % Fe in nitrogen [154].

surface oxide barriers or by combining directly to form iron-suboxides. Usually a high iron concentration promotes the formation of β-phase which has an influence on pore and grain structure and the mechanical properties.

Other metallic impurities, such as aluminium or calcium, may also form low-melting-point eutectics with silicon, which may influence the reaction kinetics in a similar way. The influence of such metallic impurities is still under discussion [155, 156].

Because of the thermodynamic instability of silicon towards oxygen, technical silicon powders always contain SiO_2 layers at the surface of the silicon particles. In the case of thin SiO_2 layers, SiO_2 can react with silicon to form gaseous SiO and this may, at least to a certain extent, be eliminated during the nitridation process. This could be the reason for the fact that RBSN in most cases exhibits lower oxygen contents than Si_3N_4-powder compacts. Thicker SiO_2 layers (> 20 nm) can, however, considerably reduce the degree of reaction [157].

5.2.2. Influence of processing conditions

5.2.2.1. Temperature–time programme. Reaction of silicon with nitrogen to form silicon nitride is an exothermal process. If the temperature–time programme is insufficiently adjusted, the heat generated during this reaction may result in overheating which makes the course of reaction uncontrollable. It is, however, not possible to provide general information about a temperature–time programme for nitridation, as this programme must be matched to the size of the furnace, the charging quantity, the size of the components, and, especially, to the characteristics of the starting powder, in each case.

Depending on the silicon starting powder, the nitridation reaction starts at temperatures of between 1000 and 1150° C and stops at temperatures above the melting point of silicon (1410° C). Time of reaction for complete nitridation of silicon powder compacts is, depending on component size, furnace size and charging quantity between some hours and several days. Too high reaction rates may lead to local overheating and hence to local melting. Even with extremely long times of reaction, the wall thicknesses which can be completely nitrided to silicon nitride are only about 3 cm. With large-sized components the diffusion of nitrogen in Si_3N_4 is rate-controlling and therefore the reaction rate is extremely slow.

TABLE X Influence of microstructural characteristics on thermal shock resistance of reaction-bonded Si_3N_4 (the increase of the microstructural parameters leads to the marked changes in properties: ↑ increase; ↓ decrease) [107]

Thermal shock resistance characterized by

$$R = \frac{\sigma(1-\nu)}{\alpha E} \quad \text{and} \quad R' = \frac{\sigma(1-\nu)}{\alpha E}\lambda$$

density	$\sigma\uparrow\downarrow\ E\uparrow\ \lambda\uparrow$	$R\uparrow\downarrow\ R'\uparrow$
macropore size	$\sigma\downarrow\ E\approx\ \lambda\approx$	$R\downarrow\ R'\downarrow$
α-content	$\sigma\uparrow\ E\approx\ \lambda\downarrow$	$R\uparrow\ R'\uparrow\downarrow$
grain structure of the α-phase including the pore structure of micropores*	$\sigma\downarrow\ E\approx\ \lambda\downarrow$	$R\downarrow\ R'\uparrow$
oxidation	$\sigma\downarrow\ E\downarrow\ \lambda\downarrow\alpha\uparrow\downarrow$	$R\downarrow\ R'\downarrow$

*coarser grain structure/larger micropores.

5.2.2.2. Gas composition. The composition of the nitriding gas and/or the nitriding gas pressure influence the course of reaction at constant temperature–time programme and thus influence the microstructural development and the resulting mechanical properties. The addition of hydrogen to the nitriding gas, for example, leads to a high partial pressure of silicon monoxide at the beginning of the nitridation reaction by the reduction of SiO_2. This results in an accelerated reaction rate (Fig. 56) and, since the α-modification is partially formed through a gas-phase reaction between SiO and nitrogen, an increasing amount of α-phase in the microstructure. The consequence is that, through the presence of hydrogen in the nitriding gas, a finer-grained, more homogeneous microstructure with improved mechanical properties is formed [149].

By contrast, inert gases, such as argon, in the nitriding gas do not have any effect on the nitridation reaction at all [149]. They may, however, as in the case of helium, lead to a more favourable heat transfer [158]. In addition, the kinetics of nitridation may be influenced by oxygen impurities in the nitriding gas.

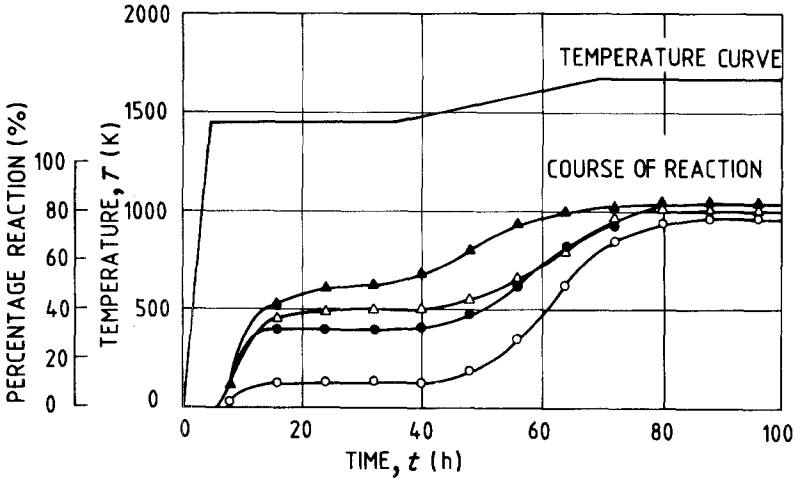

Figure 56 Nitridation of silicon powder compacts in different gas compositions [149]: (○) 100% N_2, (●) 95% N_2 + 5% H_2, (△) 90% N_2 + 10% H_2, (▲) 80% N_2 + 20% H_2.

With up to 50 v.p.m. O_2 in nitrogen, the degree of reaction does not depend on the oxygen partial pressure. But higher concentrations of oxygen may cause the reaction to stop, due to the formation of SiO_2 layers [157].

5.2.2.3. Gas pressure. Decreasing nitrogen partial pressure in the nitridation reaction strongly reduces the reaction rate. This automatically extends the time of reaction necessary to achieve a complete degree of reaction (Fig. 57) [149]. At a high nitrogen partial pressure, many Si_3N_4 nuclei are formed at the silicon surface. This results in a homogeneous, fine-grained microstructure with small pores [139]. At low nitrogen pressures, by contrast, a relatively small number of Si_3N_4 nuclei are formed at the silicon surface. With advancing reaction, silicon evaporates at the uncovered surfaces and precipitates on the few nuclei or diffuses to these nuclei (see Fig. 46). As the distance of the individual nuclei at high pressures is smaller than at low pressures, a finer, more homogeneous microstructure is obtained. Furthermore, this mechanism explains the decrease in reaction rate with decreasing nitrogen partial pressure in the nitriding gas (Fig. 57).

5.3. Properties of reaction-bonded Si_3N_4: data and microstructural effects

The properties of reaction-bonded silicon nitride are influenced in various ways by the microstructural parameters. Besides the total porosity, the size and the distribution of the macropores and micropores as well as their ratio is of importance. The grain size of the α- and/or the β-phase, the amounts of these phases and in some cases the amount of unreacted free silicon, also play a significant role. Consideration of the interrelationships between microstructural parameters and the material properties results in different assessments, depending on whether room-temperature or high-temperature properties are considered.

5.3.1. Mechanical properties at room temperature

The mechanical behaviour of RBSN materials at room temperature is brittle, and the fracture stress can be expressed as for all other ceramic materials by [159]

$$\sigma_f = \frac{1}{Y}\left(\frac{2E\gamma_I}{c}\right)^{1/2} \quad (15)$$

where E is the Young's modulus, c is the critical flaw size, and Y is a geometrical constant. The specific fracture energy, γ_I, is related to the fracture toughness of the material, K_{Ic}, by the Irwin equation

$$K_{Ic}^2 = 2\gamma_I E \quad (16)$$

Equation 15 clearly shows the parameters influencing strength.

5.3.1.1. Fracture energy. The specific fracture energy, γ_I, can be measured by using notched bend specimens or those containing artificially introduced sharp-fronted cracks [160]. Published data [160, 161] indicate that measured values depend on the root radius. As the radius decreases, the surface energy decreases. If values are compared which are obtained from sharp cracks, it can be stated that the fracture energy

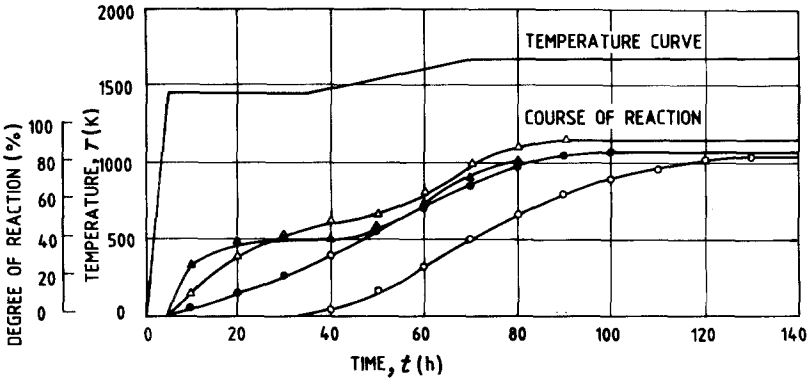

Figure 57 Nitridation of silicon powder compacts at different gas pressures [149]. $p(N_2 + H_2)$: (○) 70, (●) 130, (△) 270, (▲) 950; $N_2 : H_2 = 90 : 10$.

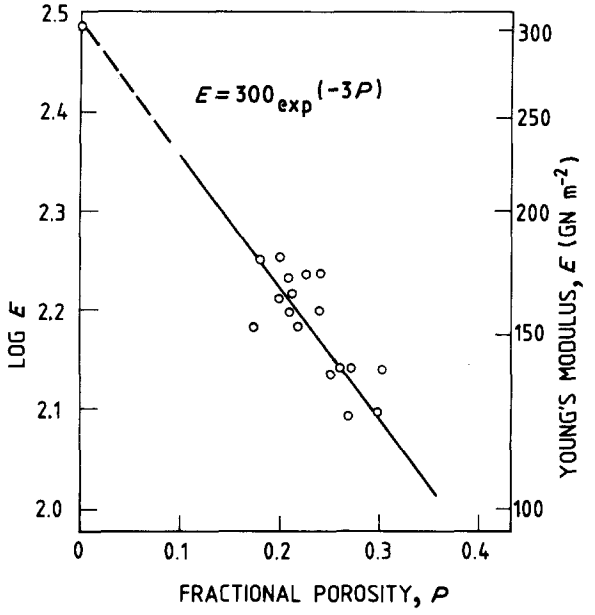

Figure 58 Semi-logarithmic plot of the Young's modulus of elasticity of Si_3N_4 as a function of porosity [38]. $E = 300 \exp(-3P)$.

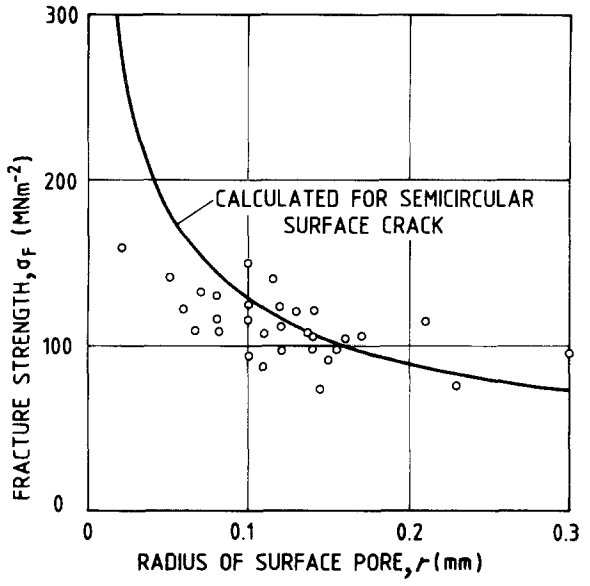

Figure 59 Fracture strength as a function of crack-initiating pore size [163].

decreases as the density decreases and there does not appear to be a marked influence of α/β ratio for a given density. Typical values of fracture energy range from $4\,J\,m^{-2}$ ($\varrho = 2.13\,g\,cm^{-3}$) to $10\,J\,m^{-2}$ ($\varrho = 2.63\,g\,cm^{-3}$) [161, 162].

5.3.1.2. Young's modulus of elasticity. Young's modulus of elasticity, E, exhibits the expected general dependence on total porosity. Data can be fitted to different relationships, one example is shown in Fig. 58 [38]. The modulus of elasticity is a bulk property and will depend on the amount and orientation of phases present in the material. In the case of RBSN the total amount of porosity seems to be the most important microstructural characteristic. For example, the materials shown in Fig. 51, with very different microstructures due to the different pore size distributions, have nearly the same elastic moduli.

5.3.1.3. Flaw size. The critical flaw size, c, is the parameter which influences the strength of RBSN most effectively. It is closely correlated with the microstructure of the material, the most obvious flaws are pores. Three main types of critical defects in RBSN can be distinguished. One type of flaw is a large pore, whilst another is machining damage. Large pores can form during the reaction-bonding process as a result of silicon melting at $T > T_{mSi}$ or by reaction with impurities even at lower temperature. For the third type, it is suggested that fields of very fine porosity rather than large pores may be regarded as critical defects.

5.3.1.4. Strength. In Fig. 59 [163], the strength of various RBSN materials with constant total porosity is shown as a function of the largest pore diameter on the tensile surface of a four-point-bending sample, together with the calculated strength for a semicircular surface crack of size c. As can be seen, the critical defect may be quite well characterized by the largest pore at the tensile surface. The room-temperature strength of RBSN materials therefore shows a great scatter for a given density (Fig. 60) [164, 165].

The increase in strength with density has to be regarded as a general trend only. A very significant factor influencing the strength is the microstructure, and here especially the pore size. To make high-strength materials it is more desirable to have a homogeneous microstructure with a narrow pore-size distribution at moderate densities than a high-density material which contains large voids. This has been shown by varying the starting silicon powder and by control of the reaction-bonding process, both of which are of great importance in affecting the quality of the material. The influence of grain size of the starting silicon powder on the strength at comparable densities is shown as an example in Fig. 61. The decrease in strength is caused by the large pores which are formed during reaction-bonding of the coarse-grained powder. Besides the macropores, strength is also influenced by the size distribution of the micropores. It has been found [153] that small mean pore sizes with a very narrow distribution lead to improved mechanical properties.

5.3.1.5. Grain size. The effect of grain size on the strength of RBSN is considerably smaller than that of the macropores, as the grain size of both the α- and the β-modification is substantially smaller than the macropore size (see Figs 51 and 52) and as changes in grain size fall within considerably closer limits. In order to investigate the effect of grain size on the strength of RBSN it is hence necessary to keep the macropore size at a constant level. This can be achieved by annealing of RBSN samples with a high α-content. During this heat treatment, the α-modification is transformed into the β-modification [24, 152]. With increasing β-amount the size of the micropores increases while the size of the macropores remains nearly constant. At constant macropore size

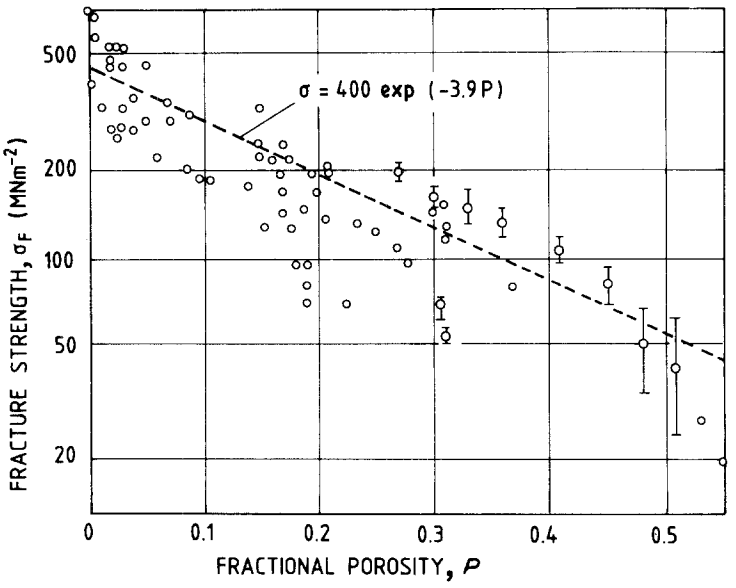

Figure 60 Semi-logarithmic plot of the flexural strength of Si_3N_4 as a function of porosity [164]. $\sigma = 400 \exp(-3.9P)$.

the strength decreases with increasing β-amount and/or with increasing micropore size (Fig. 62). But transformation of α- into β-modification is at the same time associated with an increase in grain size, which makes the situation very complicated. Hence, correlation between one microstructural parameter and strength, without taking into account the others, can lead to misinterpretations.

5.3.2. Mechanical properties and oxidation at high temperatures

5.3.2.1. High-temperature strength. Strength is nearly constant over the whole temperature range for the RBSN grades, as shown in Fig. 63. In this graph the different materials have densities of between 2.2 and 2.5 g cm^{-3}, corresponding to a porosity of between 22 and 31 vol %, and strongly differing mean pore diameters. If density increases and macropore size decreases, strength rises and remains almost constant in all cases, up to temperatures of about 1500° C presuming no other effects occur. For different RBSN material grades, however, a strength minimum has been observed at approximately 900° C. Although this drop in strength has not yet been finally clarified, it seems to be associated with the internal oxidation of reaction-bonded silicon nitride.

5.3.2.2. Oxidation. The oxidation behaviour of RBSN is very much influenced by the amount of porosity and by the pore structure. As the pores are frequently open ones, oxidation starts both at external and internal surfaces. Since both amorphous and crystalline SiO_2, which are formed during oxidation, have a larger volume than Si_3N_4, the oxidation leads to a decrease in total porosity and to a reduction in pore diameter. As the macropores are in most cases closed pores (in some cases these macropores are interconnected by micropores), the size and distribution of the micropores is the decisive parameter in an assessment of the oxidation behaviour. Small pore channels in the order of magnitude of some 10 nm are closed after a relatively short time; with larger micropores present there is an increase in the extent of internal oxidation of the

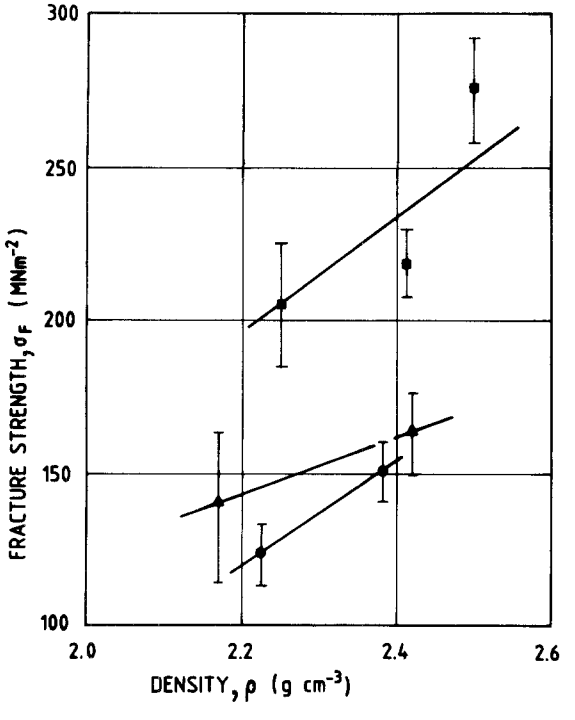

Figure 61 Flexural strength as a function of density for RBSN prepared from silicon powders with different starting grain sizes (μm): (■) < 10, (▲) 10 to 37, (●) 37 to 63 [166].

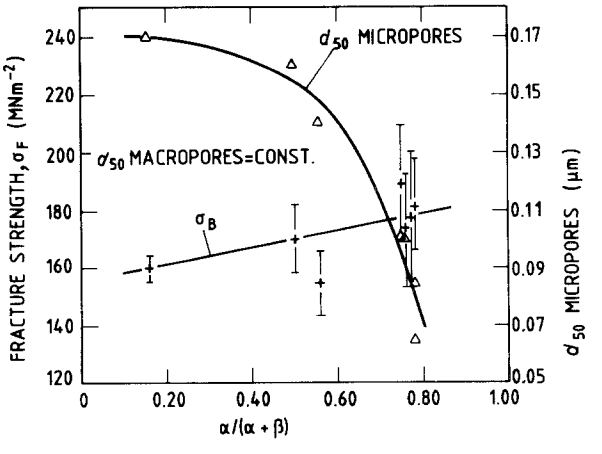

Figure 62 Influence of micropores and α/β ratio on fracture strength [152].

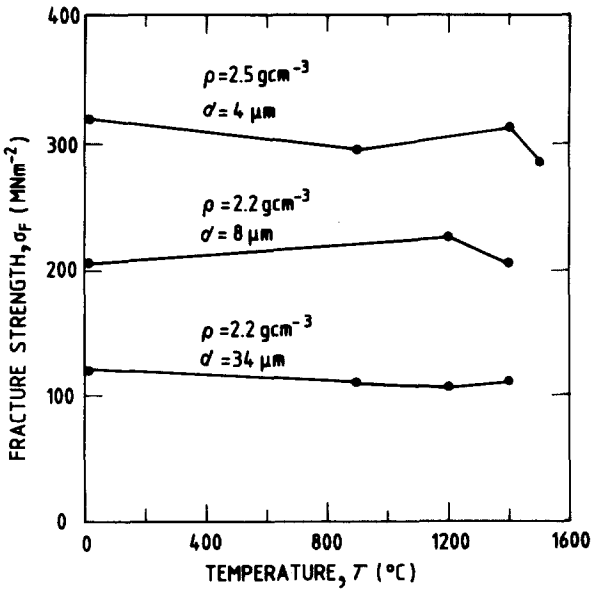

Figure 63 Flexural strength as a function of temperature for specimens of different density, ϱ, and varying mean pore diameter, d [166].

material (Fig. 64) [167, 168]. After formation of a closed SiO_2 layer, oxygen must diffuse through this SiO_2 layer for further oxidation to occur; as a result, the oxidation rate is strongly reduced. Fig. 65 illustrates the relationship between the micropore size distribution of different material grades (determined by means of a mercury porosimeter) and the cristobalite content of these RBSN materials after heat treatment at 1300° C under oxidizing conditions [168]. For samples with a small micropore size, only relatively thin cristobalite layers grow at their surface. For those with larger micropore diameters, oxidation products are even found in the centre of the samples. The decisive effect of the pore channel diameters on the weight gain during oxidation is clearly shown in Fig. 66 [169].

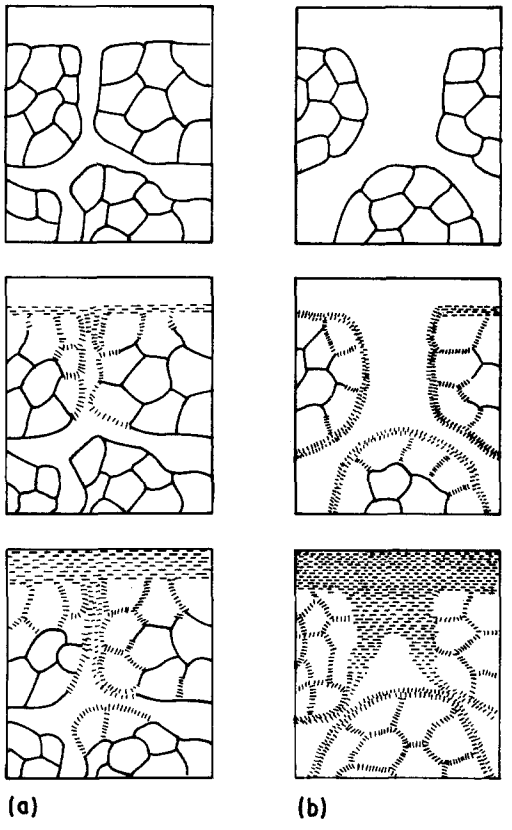

Figure 64 Model of RBSN oxidation; material with (a) small and (b) large pores [168].

Besides the pore structure, the type and degree of oxidation is determined by temperature. At high temperatures, the open pores are closed by the oxidation product in a short time and further oxidation occurs slowly by diffusion (external oxidation at temperatures of about 1200° C and higher). At lower temperatures, the open pores remain open for longer times and reaction may take place throughout the whole sample (see Fig. 65b), resulting after a certain time in a higher weight gain than at higher temperatures (internal oxidation predominates at temperatures of up to about 1100° C). Additionally, impurities play a role in forming either melts with low softening temperature by reaction with silica (e.g. calcium), by favouring diffusion through a widened glass network or by inducing crystallization which may lead to crack formation [167].

5.3.2.3. Influence of oxidation on room-temperature strength. The oxidation products and microcracks formed during cooling from the oxidation temperature lead to strong variations in the properties of RBSN materials. There is, for example, a strong and rather complex influence of oxidation on room-temperature strength [170]. Strength degradation, but also an increase in strength and unaffected strength results have been observed. At the present time, an unequivocal explanation cannot be given for the variations in strength caused by oxidation effects. Several opposing factors might be effective, depending on the oxidation conditions and on the microstructure of the materials. The main effects thought to be effective are [159, 162, 168, 170–173]:

(a) rounding off of internal flaws and pores and crack healing effects which lead in particular to an increase in strength;

(b) formation of cracks in the oxidized surface layer caused by the phase conversion of cristobalite during cooling in the temperature range between 270 and 170° C accompanied by a large volume decrease. These cracks are thought to be the reason for the observed decrease in strength after cooling;

(c) building up stresses due to the large volume increase and the changes in the coefficient of thermal expansion during the conversion of Si_3N_4 into SiO_2.

Based on these possibilities, positive and negative effects are possible.

5.3.2.4. Creep behaviour. In the case of reaction-bonded silicon nitride it is assumed that the creep mechanism is the viscous flow of a grain-boundary phase which is formed because of the thermodynamic instability of Si_3N_4 in oxygen at high temperatures. Furthermore it is thought that accommodation occurs by grain-boundary separation and by crack formation [168, 174, 175]. The creep rate of RBSN strongly depends on the open porosity and the pore size

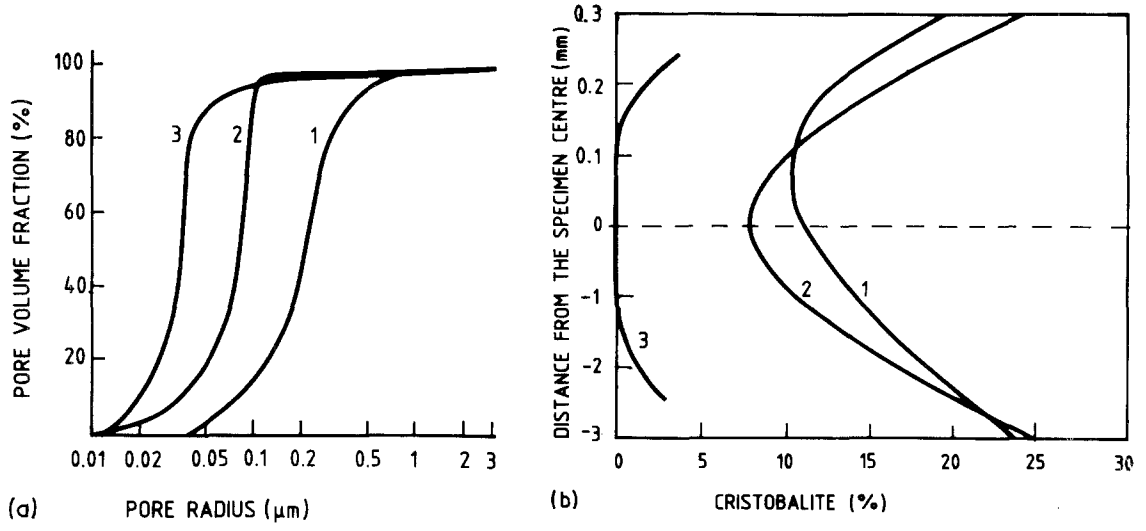

Figure 65 (a) Pore size distributions in RBSN of different grades [168]. (b) Cross-section profiles of cristobalite in RBSN samples after creep experiments [168].

distribution [168]. The correlation between the total porosity and the creep rate is shown in Fig. 67 [176] and can be described by the following Equation:

$$\frac{\dot{\varepsilon}_p}{\dot{\varepsilon}_d} = 1 + aP^2 \qquad (17)$$

where $\dot{\varepsilon}_p$ is the steady state creep rate at a certain porosity P, $\dot{\varepsilon}_d$ is the steady state creep rate at $P = 0$ and a is a constant (i.e. slope). This relation has also been observed for other ceramic materials [177]. At constant density and constant macropore size, however, the creep rate in RBSN can be significantly influenced by the micropore size distribution as demonstrated in Fig. 68 [176]. The micropore size was changed by heat treatment as mentioned above [24]. The total porosity and the size of the macropores remain constant. This increase in micropore size leads to an increased internal oxidation at 1300° C in air indicated by the increased mass gain in Fig. 69 (see also Fig. 68). The increasing oxide content in the interior of the samples facilitates grain-boundary sliding by viscous flow, thus increasing the creep rate. Similar results have been achieved when the micropore size distribution was changed by the variation of processing conditions, for example by varying the initial silicon particle size [149]. In this respect, the chemistry of the materials is of great importance. Fig. 70 [171] shows, as an example, creep strains of four RBSN grades. The porosity characteristics do not explain the great differences found, especially the behaviour of material 3. This material, however, contains 0.17 wt % Ca, nearly ten times more calcium than the other materials. This high calcium content seems to assist the formation of silicate phases with low viscosity which are detrimental to the high-temperature deformation resistance.

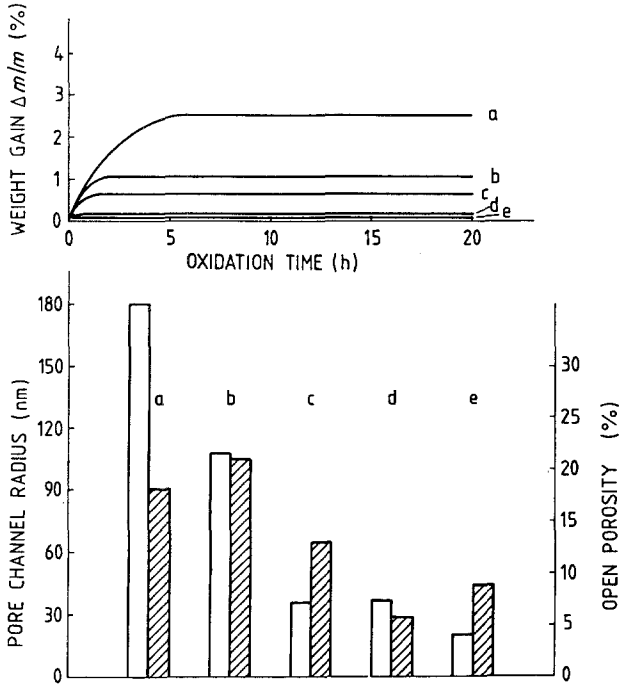

Figure 66 Oxidation of five RBSN grades with approximately constant density but different pore size characteristics [169]. T = 1260° C, air atmosphere. Solid bars: channel radius; shaded bars: open porosity.

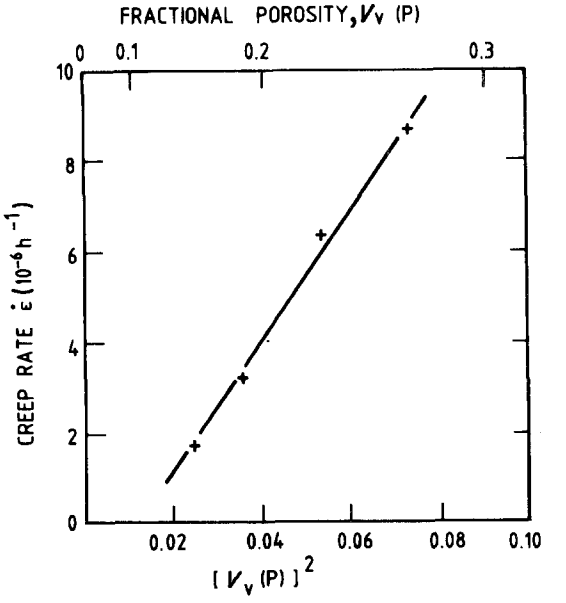

Figure 67 Porosity dependence of creep rate in air, T = 300° C, σ = 70 MPa [176].

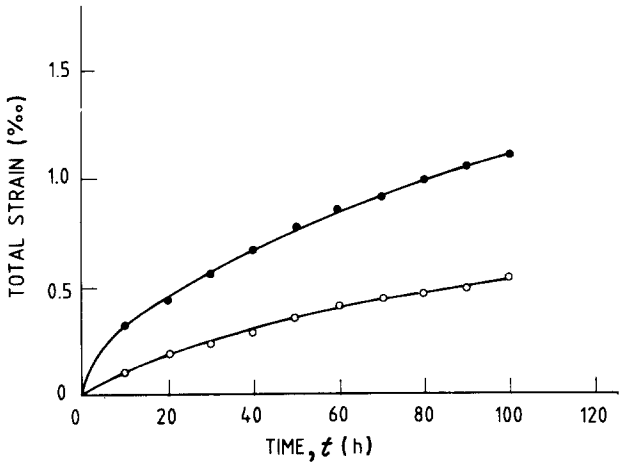

Figure 68 Total strain plotted against time for samples with different micropore sizes [176]. $\sigma = 70\,MN\,m^{-2}$, $T = 300°C$. (○) $\alpha/(\alpha + \beta) = 0.76$, d_{50} micropores $= 0.102\,\mu m$. (●) $\alpha/(\alpha + \beta) = 0.16$, d_{50} micropores $= 0.170\,\mu m$.

5.3.3. Thermal and thermo-mechanical properties

5.3.3.1. Thermal diffusivity/conductivity. The wide variation in thermal diffusivity/conductivity (see Fig. 37) can be explained by microstructural effects. Thermal diffusivity and conductivity are mainly controlled by total porosity, pore structure, the amounts of the $\alpha-$, $\beta-$ and silicon-phases, the needle-like morphology of the α-phase, as well as oxidation products.

Results of systematic investigations with mostly well-defined microstructures are summarized in Fig. 71 [128]. Thermal diffusivity/conductivity increases with higher density. Here, however, it has to be noted that in many cases density changes are accompanied by variations in other microstructural variables. The size of spherical macropores has no effect on thermal properties at constant bulk density, when other microstructural variables are also constant. The influence of the amount of unreacted silicon on thermal diffusivity is thought to be dependent on the impurity content of silicon. Results clearly indicate that the amount and morphology of the α-phase have a strong influence on thermal properties of reaction-bonded Si_3N_4. An increase in the proportion of the α-phase leads to a decrease in thermal diffusivity/conductivity. Microstructures with small α-needles and small micropores exhibit low values. In most cases, oxidation products cause a decrease in thermal diffusivity/conductivity which is dependent on the type and penetration depth of the oxidation products [24, 128, 130, 178, 179].

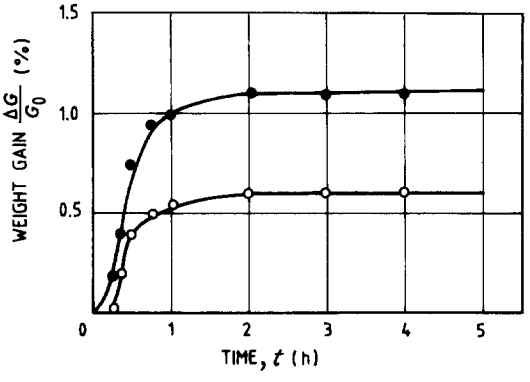

Figure 69 Mass gain plotted against time during oxidation of samples with different micropore size in air [176]. $T_c = 300°C$. (○) $\alpha/(\alpha + \beta) = 0.76$, d_{50} micropores $= 0.102\,\mu m$. (●) $\alpha(\alpha + \beta) = 0.16$, d_{50} micropores $= 0.170\,\mu m$.

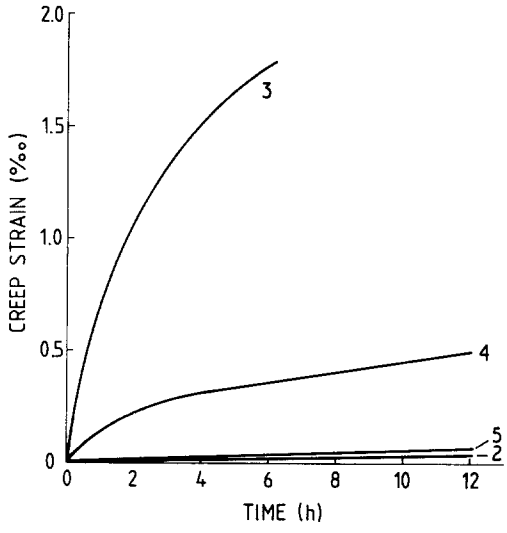

Properties of the RBSN materials studied

	Material			
	2	3	4	5
Density (g cm^{-3})	2.67	2.62	2.59	2.57
Total porosity (%)	16	18	19	19
Open porosity (%)	13	6	11	9
Size of micropores r_{50} (nm)	37	38	28	20

Figure 70 Creep curves for the RBSN materials 2 to 5, characterized in the accompanying table [171]. $T = 1400°C$, $\sigma = 100\,MN\,m^{-2}$.

5.3.3.2. Thermal shock resistance. Because of the microstructural effects on mechanical and thermal properties, thermal shock resistance of RBSN, which exhibits a wide range of values (see Fig. 40), is strongly affected by microstructure. A summary of systematic investigations of various microstructural effects on thermal shock resistance is given in Fig. 72 [132] (for interpretation of this graph see Section 4.3 and Fig. 42).

Porosity, the size of macropores, the proportion and morphology of the α-phase (controlling the fine pore structure), and oxidation processes (also influenced by the pore structure) have an important influence on thermal shock resistance to fracture initiation. High densities generally improve the thermal shock resistance. When the total porosity and other microstructural parameters are constant, an increase in pore size leads to a decrease in thermal stress resistance to fracture initiation. However, RBSN is a material which additionally reveals a strong effect of phase composition α/β (which is closely connected with the fibre-like morphology of the α-phase and the size of micropores) on mechanical and thermal properties, and consequently on thermal shock resistance. For example, a high proportion of α and very fine grain structures of the α-phase cause a decrease in the thermal shock resistance due to a reduction in thermal conductivity. The influence of oxidation is strongly dependent on the microstructure of the material and

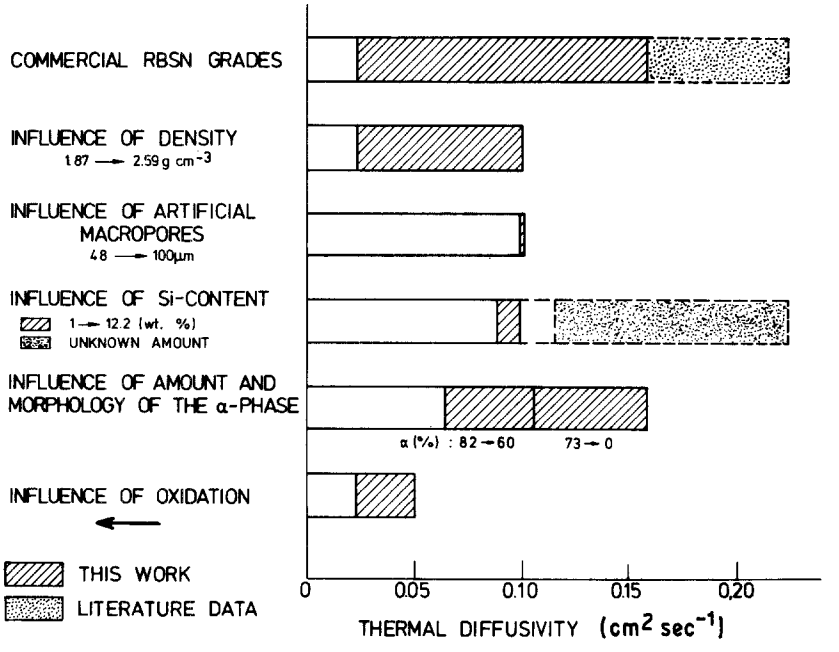

Figure 71 Influence of various microstructural characteristics on the thermal diffusivity of RBSN [7].

on the oxidation conditions. In most cases, thermal shock resistance is decreased by oxidation effects. In many cases, a superposition of various microstructural effects (density, macropore size, amount and morphology of the α-phase) takes place, depending on the processing conditions.

It can be concluded from these results that thermal shock resistance to fracture initiation of RBSN can be considerably improved by processing materials with higher densities, smaller macropores and a coarser grain structure for the α-phase. A high concentration of α-phase and oxidation products, which are strongly dependent on the pore structure of the material, may have an essentially negative effect on thermal shock resistance [107, 128, 132, 170, 180].

5.3.3.3. Thermal cycling behaviour. Reaction-bonded Si_3N_4 exhibits large differences in strength degradation during thermal cycling (see Fig. 73). The comparison of the thermal cycling behaviour with oxidation experiments and the correlation with various microstructural characteristics indicate that oxidation obviously plays an important role during thermal cycling. Systematic investigations permit the conclusion to be drawn [135, 181] that, for a large number of grades, strength degradation during thermal cycling is mainly controlled by the flaw size in the oxidized surface layer and by the critical flaw size of the unoxidized materials. Consequently, all parameters which affect the oxidation behaviour, such as open porosity, and the size of micropores, have an important influence on the thermal cycling behaviour of reaction-bonded Si_3N_4. Differences in these microstructural characteristics and in the critical flaw size of the unoxidized materials (this means the initial strength of the starting material) cause the wide range of thermal cycling behaviour of reaction-bonded Si_3N_4. This is demonstrated in Figs 74 and 75. Fig. 74 shows the thermal cycling behaviour of three materials with different initial strength values (caused by differences in the size of macropores), but with similar values of the open porosity and the size of micropores. The lower the initial strength, the smaller the strength reduction during thermal cycling. Fig. 75 shows the

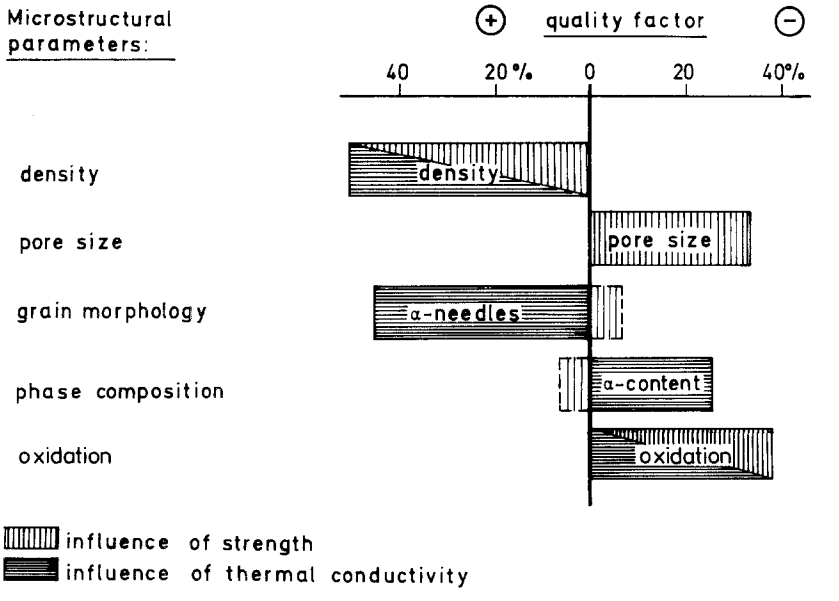

Figure 72 Influence of various microstructural characteristics on the thermal shock resistance of RBSN [128, 132].

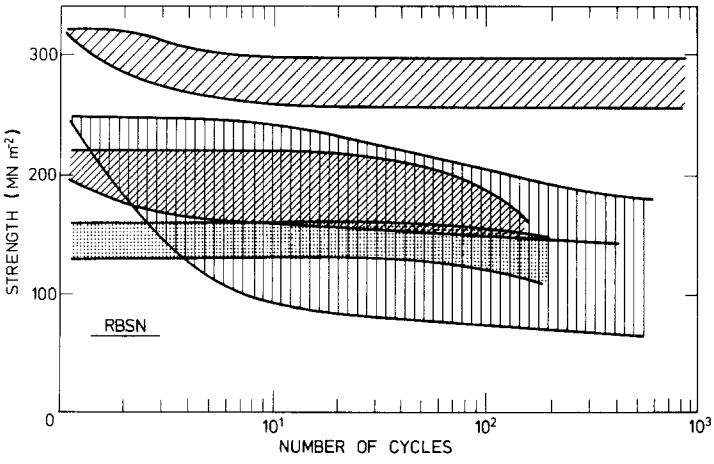

Microstructural characteristics

Material group	Density (g cm^{-3})	Open porosity (%)	Micropore size d_{50} (μm)	$\alpha/(\alpha + \beta)$ ratio
$\sigma \sim 150$ MN m^{-2}	2.31–2.45	12.3–21.5	0.09–0.15	0.60–0.92
$\sigma \sim 200$ MN m^{-2}	2.25–2.58	16.8–20.7	0.05–0.13	0.78–0.85
$\sigma \sim 250$ MN m^{-2}	2.45–2.65	6.6–18.2	0.04–0.18	0.76–0.84
$\sigma > 300$ MN m^{-2}	2.49–2.58	6.7–10.1	0.03–0.06	0.76–0.78

*Mean pore size from cumulative frequency distribution.

Figure 73 Strength behaviour after thermal cycling of a number of RBSN grades summarized in material groups of similar initial strength (the scatter in each material group represents the results of various grades) [135]. T_F = 1260° C → RT (cooling rate 80° C sec^{-1}).

strength behaviour after thermal cycling of three materials with the same initial strength values, but differences in the amount of open porosity and in the size of micropores. As indicated by these results, there are large differences in the strength degradation of these materials. High values of open porosity and of the size of micropores lead to a large decrease in strength [135, 181].

As a result of these systematic investigations, an improvement of the thermal cycling behaviour of RBSN can be expected by optimizing all those microstructural characteristics which make the material more oxidation-resistant.

6. Conclusions and outlook

Considering the processing techniques of Si_3N_4 and the improvement of the mechanical and thermomechanical properties, it can be stated that during the past few years enormous progress has been made. Thus, dense Si_3N_4 can easily meet the strength requirements up to temperatures of about 1000° C for a variety of applications. The nature of the grain-boundary phases, however, leads at higher temperatures (because of softening effects) to a decrease in strength, creep and oxidation resistance. Furthermore, the production costs of complex-shaped components produced from hot-pressed Si_3N_4 are too high, also the reliability of material properties and of the production of large complex-shaped components by the advanced process techniques are, at the present time, not satisfactory. Reaction-bonded Si_3N_4 offers an almost perfect near-net shape fabrication process for mass production and low cost. Nevertheless, because of the residual porosity the strength values of

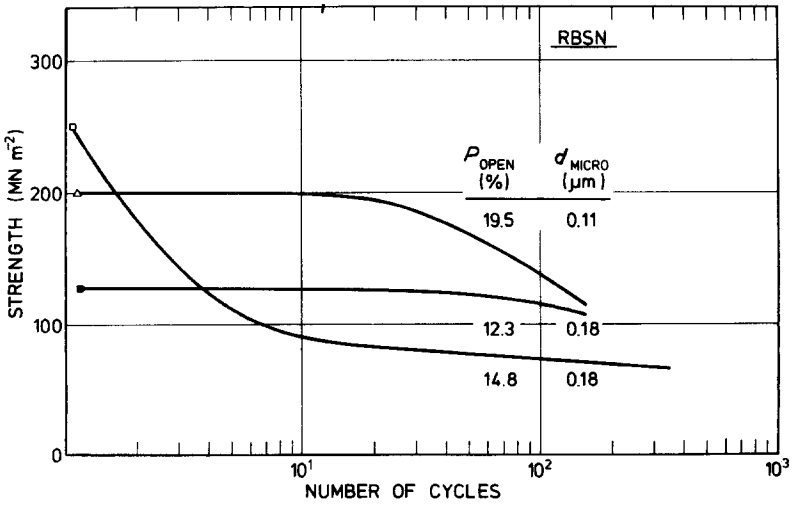

Figure 74 Strength behaviour after thermal cycling of three RSBN materials with different initial strength values, but similar microstructural characteristics [135]. Density (g cm^{-3}): (□) 2.46, (△) 2.58, (■) 2.38. T_F = 1260° C → RT (cooling rate 80° C sec^{-1}).

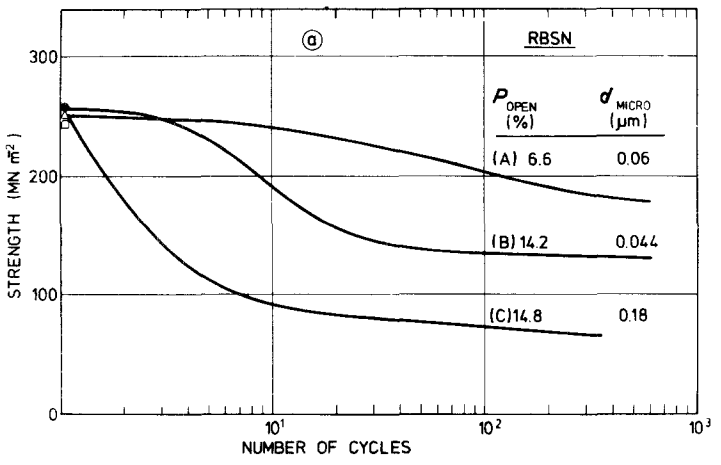

Figure 75 Strength behaviour after thermal cycling of three RBSN materials with the same initial strength, approximately the same density, but variations in the amount of open porosity and the size of micropores [135]. Density (g cm^{-3}): material A 2.58, material B 2.59, material C 2.46. T_F = 1260° C → **RT** (cooling rate 80° C sec^{-1}).

RBSN are relatively low. Because of the pore structure of this material the main problem is oxidation, particularly at intermediate temperatures, which has a detrimental effect on fracture strength, creep, thermal shock and thermal cycling behaviour. Thus, porosity and pore structure limit the range of possible applications of RBSN.

Therefore, further development in the area of Si_3N_4 is mainly concentrated on the following goals:

1. In the case of dense Si_3N_4:

(a) to intensify the work on the less-expensive processing techniques for complex-shaped components (sintering, gas-pressure sintering and hot-isostatic pressing) in order to use Si_3N_4 on a broader scale;

(b) to improve the high-temperature properties by optimizing the grain boundary characteristics, particularly to combine high room-temperature strength with good high-temperature properties, by crystallizing or avoiding the grain-boundary layers and by further improving the elongated grain structure.

2. In the case of reaction-bonded Si_3N_4: to reduce the residual porosity and to improve the oxidation resistance on the basis of controlling the pore structure by decreasing the size of macropores and by establishing narrow pore size distributions with small mean pore size.

3. Moreover, for both material groups: higher reliability is required for material properties, mass production and processing of large components.

These development lines include the following topics. In the case of sintering, further improvement of the powder properties (sintering activity, grain morphology and chemistry) as well as a more economical way of powder fabrication have to be found. Regarding the advanced processing techniques, sintering/gas pressure sintering and hot-isostatic pressing of Si_3N_4, the favourable possibilities for producing complex-shaped components with good thermo-mechanical properties, for improving high-temperature properties, and for increased, more uniform and less scattered strength properties have to be realized. These development steps have to be combined with the quantitative characterization of microstructure and the improvement of high-temperature properties.

As a result of basic investigations and of the new processing techniques a further step-by-step progress for Si_3N_4 may be expected in the future, including in particular the fabrication of complex-shaped components. This further development work should extend the application of Si_3N_4 as an engineering material.

References

1. F. L. RILEY, (ed.), "Nitrogen Ceramics" (Noordhoff-Leyden, 1977).
2. W. BUNK, M. BÖHMER and H. KISSLER, (eds), "Keramische Komponenten für Fahrzeug-Gasturbinen", Vols I to III (Springer-Verlag, Berlin, 1984).
3. E. M. LENOE, R. N. KATZ and J. J. BURKE (eds), "Ceramics for High-Performance Applications", Vol. III (Plenum, New York, London, 1979).
4. F. L. RILEY (ed.), "Progress in Nitrogen Ceramics" (Martinus Nijhoff, 1983).
5. K. H. JACK, The Fabrication of Dense Nitrogen Ceramics, in "Hayne-Palmour IV: Processing of Crystalline Ceramics", Vol. 11 (Materials Science Research, Plenum, New York, 1978) p. 561.
6. F. F. LANGE, *Int. Met. Rev.* **1** (1980) 1.
7. G. ZIEGLER, *Z. Werkstofftech.* **14** (1983) 147.
8. *Idem, ibid.* **14** (1983) 189.
9. J. W. EDINGTON, D. J. ROWCLIFFE and J. L. HENSHALL, *Powder Met. Int.* **7** (1975) 82.
10. *Idem, ibid.* **7** (1975) 136.
11. D. C. LARSEN and J. W. ADAMS, "Evaluation of Ceramics and Ceramic Composites for Turbine Engine Applications", IIT-Research Institute, Semiannual Interim Technical Report No. 13, June 1983; Contract F 33615-82-C-5101.
12. I. B. CUTLER and W. J. CROFT, *Powder Met. Int.* **6** (1974) 82.
13. *Idem, ibid.* **6** (1974) 144.
14. D. R. MESSIER and W. J. CROFT, Silicon Nitride, in "Preparation and Properties of Solid State Materials", Vol. 7, edited by W. R. Wilcox (Marcel Dekker, New York, Basel, 1982) pp. 131–220.
15. D. R. MESSIER and M. M. MURPHY, "An Annotated Bibliography on Silicon Nitride for Structural Applications" (Metals and Ceramics Information Center, Battelle, Columbus, Ohio, MCIC-79-41, 1979).
16. D. HARDIE and K. H. JACK, *Nature* **180** (1957) 332.
17. S. N. RUDDLESDEN and P. POPPER, *Acta Crystallogr.* **11** (1958) 465.
18. S. WILD, P. GRIEVESON and K. H. JACK, *Special Ceram.* **5** (1972) 385.
19. H. FELD, P. ETTMAYER and I. PETZENHAUSER, *Ber. Dt. Keram. Ges.* **51** (1974) 127.
20. C. M. B. HENDERSON and D. TAYLOR, *Trans. Brit. Ceram. Soc.* **74** (1975) 49.
21. K. BLEGEN, *Special Ceram.* **6** (1975) 223.
22. P. E. D. MORGAN, Research on Densification, Character and Properties of Dense Silicon Nitride; Franklin Institute, Philadelphia, TR AD 778 373 (1974).

23. D. R. MESSIER and F. L. RILEY, in "Nitrogen Ceramics", edited by F. L. Riley (Noordhoff-Leyden, 1977) pp. 141–9.
24. G. ZIEGLER and J. HEINRICH, *Sci. Ceram.* **11** (1981) 511.
25. W. P. CLANCY, *Microscope* **22** (1974) 279.
26. K. H. JACK, in "Nitrogen Ceramics", edited by F. L. Riley (Noordhoff-Leyden, 1977) pp. 109–28.
27. D. P. THOMPSON, P. KORGUL and A. HENDRY, in "Progress in Nitrogen Ceramics", edited by F. L. Riley (Matinus-Nijhoff, 1983) pp. 61–74.
28. L. J. GAUCKLER and G. PETZOW, in "Nitrogen Ceramics", edited by F. L. Riley (Noordhoff-Leyden, 1977) pp. 41–62.
29. D. P. THOMPSON and L. J. GAUCKLER, *J. Am. Ceram. Soc.* **60** (1977) 470–1.
30. S. HAMPSHIRE, H. K. PARK, D. P. THOMPSON and K. H. JACK, *Nature* **274** (1978) 880.
31. P. GREIL and G. PETZOW, in "Keramische Komponenten für Fahrzeug-Gasturbinen", edited by W. Bunk, M. Böhmer and H. Kissler, Vol. III (Springer-Verlag, Berlin, 1984).
32. K. H. JACK, in "Progress in Nitrogen Ceramics", edited by F. L. Riley (Martinus-Nijhoff, 1983) pp. 45–60.
33. S. PROCHAZKA and C. D. GRESKOVICH, Development of a Sintering Process for High-Performance Silicon Nitride, AMMRC TR 78-32 (1978).
34. S. C. SINGHAL, *Ceramurg. Int.* **2** (1976) 123.
35. G. WÖTTING, Thesis, TU Berlin (1983).
36. K. KIJIMA and S. SHIRASAKI, *J. Chem. Phys.* **65** (1976) 2668.
37. H. SALMANG and H. SCHOLZE, "Die physikalischen und chemischen Grundlagen der Keramik" (Springer-Verlag, Berlin, 1968).
38. A. J. MOULSON, *J. Mater. Sci.* **14** (1979) 1017.
39. G. WÖTTING and G. ZIEGLER, *Sprechsaal* **119** (1986) pp. 265, 555, continued 1987.
40. E. GUGEL, A. F. FICKEL and H. KESSEL, *Powder Met. Int.* **6** (1974) 136.
41. L. J. BOWEN, R. J. WESTON, T. G. CARRUTHERS and R. J. BROOK, *J. Mater. Sci.* **13** (1978) 341.
42. G. ZIEGLER, L. D. BENTSEN and D. P. H. HASSELMAN, *J. Am. Ceram. Soc.* **64** (1981) C35.
43. F. F. LANGE, *ibid.* **56** (1973) 518.
44. G. R. TERWILLIGER and F. F. LANGE, United States Patent 3 992 497, 16 November (1976).
45. C. D. GRESKOVICH and J. H. ROSOLOWSKI, *J. Am. Ceram. Soc.* **59** (1976) 336.
46. M. MITOMO, *J. Mater. Sci.* **11** (1976) 1103.
47. H. F. PRIEST, G. L. PRIEST and G. E. GAZZA, *J. Am. Ceram. Soc.* **60** (1977) 80.
48. A. GIACHELLO, P. C. MARTINENGO, G. TOMMASINI and P. POPPER, *J. Mater. Sci.* **14** (1979) 2825.
49. R. POMPE and R. CARLSSON, in "Progress in Nitrogen Ceramics", edited by F. L. Riley (Martinus-Nijhoff, 1983) pp. 219–24.
50. G. WÖTTING and H. HAUSNER, *ibid.*, p. 211.
51. P. POPPER, "Problems in Sintering Silicon Nitride", Research Paper no. 699 (British Ceramic Society, October 1978).
52. J. A. MANGELS and G. J. TENNENHOUSE, *Am. Ceram. Soc. Bull.* **59** (1980) 1216.
53. *Idem, ibid.* **59** (1980) 1222.
54. A. LARKER, Hot-Isostatic Pressing of Shaped Silicon Nitride Parts, in "High-Pressure Science and Technology", Vol. 2, edited by K. D. Tummerhans and M. S. Barber (Plenum, New York, 1979).
55. J. HEINRICH and M. BÖHMER, *Sci. Ceram.* **11** (1981) 439.
56. H. LARKER, AGARD Conference Proceedings no. 276, "Ceramics for Turbine Applications" (1979) 24/1–24/8, edited by E. Campo and P. Martinengo, AGARD Rep. no. 651 (1976).
57. G. ZIEGLER and G. WÖTTING, *Int. J. High Tech. Ceram.* **1** (1985) 31.
58. W. D. KINGERY, *J. Appl. Phys.* **30** (1959) 301.
59. H. KNOCH and G. ZIEGLER, *Sci. Ceram.* **9** (1977) 494.
60. H. KNOCH and G. E. GAZZA, *Ceramurg. Int.* **6** (1980) 51.
61. S. HAMPSHIRE and K. H. JACK, *Special Ceram.* **7** (1981) 37.
62. P. DREW and M. H. LEWIS, *J. Mater. Sci.* **9** (1974) 261.
63. F. F. LANGE, *J. Am. Ceram. Soc.* **62** (1979) 428.
64. G. WÖTTING and G. ZIEGLER, *Ceramurg. Int.* **10** (1984) 18.
65. *Idem, Sci. Ceram.* **12** (1983) 361.
66. D. R. CLARKE and G. THOMAS, *J. Am. Ceram. Soc.* **61** (1978) 114.
67. D. R. CLARKE, *ibid.* **64** (1981) 601.
68. T. M. SHAW, O. L. KRIVANEK and G. THOMAS, *ibid.* **62** (1979) 305.
69. R. E. LOEHMAN, *J. Non-Cryst. Solids* **42** (1980) 433.
70. G. SCHWIER, in "Keramische Komponenten für Fahrzeug-Gasturbinen", Vol. III, edited by W. Bunk, M. Böhmer and H. Kissler (Springer-Verlag, Berlin, 1984) p. 55.
71. S. T. BULJAN and P. E. STERMER, US Patent 4 073 845, February (1978).
72. M. MORI, H. INOUE and T. OCHIAI, in "Progress in Nitrogen Ceramics", edited by F. L. Riley (Martinus-Nijhoff, 1983) pp. 149.
73. T. YAMATE, T. KAWAHITO and T. IWAI, in Proceedings of the International Symposium on Ceramic Components for Engines, edited by S. Somiya, E. Kanai and K. Ando (KTK Scientific, Tokyo, 1983) p. 333.
74. P. R. MILLER, J. G. LEE and I. B. CUTLER, *J. Am. Ceram. Soc.* **62** (1979) 147.
75. C. D. GRESKOVICH and C. O'CLAIR, *Am. Ceram. Soc. Bull.* **57** (1978) 1055.
76. W. ENGEL, *Powder Met. Int.* **10** (1978) 124.
77. A. G. EVANS, in "Progress in Nitrogen Ceramics", edited by F. L. Riley (Martinus-Nijhoff, 1983) pp. 595–625.
78. D. MUNZ, O. ROSENFELDER, K. GOEBBELS and H. REITER, in "Keramische Komponenten für Fahrzeug-Gasturbinen", Vol. III, edited by W. Bunk, M. Böhmer and H. Kissler (Springer-Verlag, Berlin, 1984) pp. 513–35.
79. G. WÖTTING, R. PEITZSCH and H. HAUSNER, *Sci. Sintering* **17** (1985) 87.
80. G. WÖTTING and G. ZIEGLER, *Powder Met. Int.* **18** (1986) 35.
81. I. C. HUSEBY and G. PETZOW, *ibid.* **6** (1974) 17.
82. H. HAUSNER, *Sci. Ceram.* **12** (1983) 229.
83. K. S. MAZDIYASNI and C. M. COOKE, *J. Am. Ceram. Soc.* **57** (1974) 536.
84. R. PEITZSCH and H. HAUSNER, in Proceedings of the International Symposium on Ceramic Components for Engines, edited by S. Somiya, E. Kanai and K. Ando (KTK Scientific, Tokyo, 1983) p. 208.
85. J. BRIGGS, *Mater. Res. Bull.* **12** (1977) 1047.
86. C. L. QUACKENBUSH, J. T. SMITH, J. T. NEIL and K. W. FRENCH, in "Progress in Nitrogen Ceramics", edited by F. L. Riley (Martinus-Nijhoff, 1983) p. 669.
87. L. J. BOWEN, T. G. CARRUTHERS and R. J. BROOK, *J. Am. Ceram. Soc.* **61** (1978) 335.
88. G. E. GAZZA, in "Progress in Nitrogen Ceramics", edited by F. L. Riley (Martinus-Nijhoff, 1983) p. 273.
89. P. F. D. MORGAN, F. F. LANGE, D. R. CLARKE and B. I. DAVIS, *J. Am. Ceram. Soc.* **64** (1981) C77.
90. J. DODSWORTH and D. P. THOMPSON, *Sci. Ceram.* **11** (1981) 51.
91. I. J. McCOLM, *JEMMSE*, to be published.
92. G. PETZOW and P. GREIL, in Proceedings of the International Symposium on Ceramic Components for Engines, edited by S. Somiya, E. Kanai and K. Ando (KTK Scientific, Tokyo, 1983) p. 177.
93. G. WÖTTING and G. ZIEGLER, *Fortschrittsber. DKG* **1** (1985) 33.
94. *Idem*, in Proceedings of the International Symposium on Ceramic Components for Engines, edited by S. Somiya, E. Kanai and K. Ando (KTK Scientific, Tokyo, 1983) p. 412.

95. B. KANKA, G. WÖTTING and G. ZIEGLER, in preparation.
96. C. D. GRESKOVICH and J. A. PALM, Development of High Performance Sintered Si_3N_4; Report No. AMMRC TR 80-46, September (1980).
97. G. WÖTTING and G. ZIEGLER, *Fortschrittsber. DKG* (1986) to be published.
98. P. L. ANTONA, A. GIACHELLO and P. C. MARTINENGO, in "Ceramic Powders", Proceedings 5th CIMTEC, edited by P. Vincenzini (Elsevier, Amsterdam, 1983) pp. 753–66.
99. R. POMPE, L. HERMANSSON and R. CARLSON, *Sprechsaal* **115** (1982) 1098.
100. J. A. MANGELS, "Sintered Reaction-Bonded Si_3N_4 for the AGT 101 Turbine Rotor"; Report prepared for NASA-Lewis, Contract No. DEN 3-167, November (1980).
101. H. J. KLEEBE, G. WÖTTING and G. ZIEGLER, in Proceedings 6th CIMTEC, to be published.
102. J. HEINRICH and M. BÖHMER, *Powder Met. Int.* **16** (1984) 233.
103. *Idem, ibid* **16** (1984) 283.
104. G. K. WATSON, T. J. MOORE and M. L. MILLARD, *J. Am. Ceram. Soc.* **67** (1984) C208.
105. J. HEINRICH, N. HENN and M. BÖHMER, *Mater. Sci. Eng.* **71** (1985) 131.
106. K. HOMMA, T. TATSUNO, H. OKADA and H. TAKADA, *Zairyo* **31** (1982) 960.
107. G. ZIEGLER, *Z. Werkstofftech.* **16** (1985) 44.
108. A. TSUGE and K. NISHIDA, *Am. Ceram. Soc. Bull.* **57** (1978) 424.
109. *Idem, ibid.* **57** (1978) 431.
110. G. HIMSOLT, H. KNOCH, H. HÜBNER and F. W. KLEINLEIN, *J. Am. Ceram. Soc.* **62** (1979) 29.
111. J. HEINRICH and M. BÖHMER, *Ber. Dtsch. Keram. Ges.* **61** (1984) 399.
112. F. THÜMMLER and G. GRATHWOHL, "Creep of Ceramic Materials for Gas Turbine Applications" AGARD Rep. no. 651 (1976).
113. S. UD DIN and P. S. NICHOLSON, *J. Mater. Sci.* **10** (1975) 1375.
114. J. M. BIRCH and B. WILSHIRE, *ibid.* **13** (1978) 2627.
115. P. J. DIXON-STUBBS and B. WILSHIRE, *ibid.* **14** (1979) 2773.
116. R. A. L. DREW, S. HAMPSHIRE and K. H. JACK, *Special Ceram.* **7** (1981) 119.
117. S. C. SINGHAL, *J. Mater. Sci.* **11** (1976) 500.
118. D. CUBICCIOTTI, K. H. LAU and R. L. JONES, *J. Electrochem. Soc.* **124** (1977) 1955.
119. G. N. BABINI, A. BELLOSI and P. VINCENZINI, *Sci. Ceram.* **11** (1981) 291.
120. M. H. LEWIS and P. BARNARD, *J. Mater. Sci* **15** (1980) 443.
121. D. R. CLARKE, in "Progress in Nitrogen Ceramics", edited by F. L. Riley (Martinus-Nijhoff, 1983) pp. 421–6.
122. P. VINCENZINI and A. BABINI, in "Sintered Metal-Ceramic Composites", edited by G. S. Upadhyaya (Elsevier, Amsterdam, 1984) p. 425.
123. R. N. KATZ and G. E. GAZZA, in "Nitrogen Ceramics", edited by F. L. Riley (Noordhoff-Leyden, 1977) pp. 417–31.
124. J. F. WESTON, P. L. PRATT and B. C. H. STEELE, *J. Mater. Sci.* **13** (1978) 2137.
125. P. GREIL, J. C. BRESSIANI and G. PETZOW, in Proceedings of the International Symposium on Ceramic Components, edited by S. Somiya, E. Kanai and K. Ando (KTK Scientific, Tokyo, 1983) pp. 228–35.
126. R. J. LUMBY, *Ceram. Eng. Sci. Proc.* **3** (1982) 50.
127. E. BUTLER, R. J. LUMBY and A. SZWEDA, in Proceedings of the International Symposium on Ceramic Components, edited by S. Somiya, E. Kanai and K. Ando (KTK Scientific, Toyko, 1983) p. 159.
128. G. ZIEGLER, in "Progress in Nitrogen Ceramics", edited by F. L. Riley (Martinus-Nijhoff, 1983) p. 565.
129. G. ZIEGLER, K. BENTSEN and D. P. H. HASSELMAN, *J. Am. Ceram. Soc.* **64** (1981) C 35.
130. G. ZIEGLER and D. P. H. HASSELMAN, *J. Mater. Sci.* **61** (1981) 495.
131. G. ZIEGLER, *Z. Werkstofftech.* **16** (1985) 12.
132. *Idem, ibid.* **16** (1985) 81.
133. G. ZIEGLER and D. P. H. HASSELMAN, *Ceramurg. Int.* **5** (1979) 126.
134. G. ZIEGLER and H. KNOCH, *Special Ceram.* **7** (1981) 145.
135. G. ZIEGLER, in Proceedings of the International Symposium on Ceramic Components for Engines, edited by S. Somiya, E. Kanai and K. Ando (KTK Scientific, Tokyo, 1983) pp. 236–48.
136. G. ZIEGLER, *Ber. Dt. Keram. Ges.* **55** (1978) 397.
137. D. R. MESSIER and P. WONG, *J. Am. Ceram. Soc.* **56** (1973) 480.
138. H. M. JENNINGS and M. H. RICHMAN, *J. Mater. Sci.* **11** (1976) 2087.
139. A. ATKINSON, A. J. MOULSON and E. W. ROBERTS, *J. Am. Ceram. Soc.* **59** (1976) 285.
140. A. ATKINSON, P. J. LEATT, A. J. MOULSON and E. W. ROBERTS, *J. Mater. Sci.* **9** (1974) 981.
141. D. CAMPOS-LORITZ and F. L. RILEY, *Sci. Ceram.* **9** (1977) 38.
142. P. LONGLAND and A. J. MOULSON, *J. Mater. Sci.* **13** (1978) 2279.
143. M. W. LINDLEY, D. P. ELIAS, B. F. JONES and K. C. PITMAN, *ibid.* **14** (1979) 70.
144. A. G. EVANS and J. V. SHARP, in "Electron Microscopy and Structure of Materials", edited by G. Thomas, R. M. Fulrath and R. M. Fisher (University of California Press, 1972) pp. 1141–54.
145. S. C. DANFORTH and M. H. RICHMAN, *Metallogr.* **9** (1976) 321.
146. M. MITOMO, *J. Mater. Sci.* **12** (1977) 273.
147. W. M. DAWSON, P. ARUNDALE and A. J. MOULSON, *Sci. Ceram.* **9** (1977) 111.
148. J. HEINRICH and G. STREB, *J. Mater. Sci.* **14** (1979) 2083.
149. J. HEINRICH, Thesis, TU Berlin (1979).
150. J. HEINRICH, *Ber. Dt. Keram. Ges.* **55** (1978) 238.
151. B. F. JONES and M. W. LINDLEY, *Powder Met. Int.* **8** (1976) 32.
152. J. HEINRICH and H. HAUSNER, in "Energy and Ceramics", Proceedings of the 4th International Meeting on Modern Ceramics Technologies, edited by P. Vincenzini, (Elsevier, Amsterdam, Oxford, New York, 1980) pp. 780–92.
153. H. J. KLEEBE and G. ZIEGLER, *Sci. Ceram.* **13** (1985) 97.
154. S. M. BOYER and A. J. MOULSON, *J. Mater. Sci.* **13** (1978) 1637.
155. R. B. GUTHRIE and F. L. RILEY, *ibid.* **9** (1974) 1363.
156. D. J. GODFREY, *Proc. Brit. Ceram. Soc.* **25** (1975) 325.
157. A. MARCKS, Thesis, TU Berlin (1980).
158. J. A. MANGELS, *Am. Ceram. Soc. Bull.* **60** (1981) 613.
159. R. W. DAVIDGE and A. G. EVANS, *Mat. Sci. Eng.* **6** (1970) 381.
160. A. G. EVANS, in "Fracture Mechanics of Ceramics", edited by R. C. Bradt *et al.* (Plenum, New York, 1974) p. 17.
161. B. J. DALGLEISH and P. L. PRATT, *Proc. Brit. Ceram. Soc.* **25** (1975) 295.
162. A. G. EVANS and R. W. DAVIDGE, *J. Mater. Sci.* **5** (1970) 314.
163. J. HEINRICH and D. MUNZ, *Am. Ceram. Soc. Bull.* **59** (1980) 1221.
164. R. W. RICE, *J. Mater. Sci.* **12** (1977) 627.
165. R. W. DAVIDGE, in "Nitrogen Ceramics", edited by F. L. Riley (Noordhoff-Leyden, 1977) pp. 541–59.
166. J. HEINRICH and W. BUNK, *Interceram.* **5** (1981) 489.
167. F. PORZ, "Reaktionsgesintertes Siliciumnitrid: Charakterisierung, Oxidation und mechanische Eigenschaften" (KFK, Bericht 3375, 1982).
168. G. GRATHWOHL and F. THÜMMLER, *J. Mater. Sci.* **13** (1978) 1177.
169. F. THÜMMLER, G. GRATHWOHL and F. PORZ, in "Keramische Komponenten für Fahrzeug-Gasturbinen", Vol.

III, edited by W. Bunk, M. Böhmer and H. Kissler (Springer-Verlag, Berlin, 1984) pp. 449–85.
170. G. ZIEGLER, *Sci. Ceram.* **11** (1981) 503.
171. F. PORZ, G. GRATHWOHL and F. THÜMMLER, *Proc. Brit. Ceram. Soc.* **31** (1981) 157.
172. J. V. SHARP, *J. Mater. Sci.* **8** (1973) 1755.
173. J. E. SIEBELS, in "Ceramics for High-Performance Applications", Vol. III, edited by E. M. Lenoe, R. N. Katz and J. J. Burke (Plenum, New York, 1979) p. 793.
174. J. M. BIRCH and B. WILSHIRE, *J. Mater. Sci.* **13** (1978) 2627.
175. G. GRATHWOHL and F. THÜMMLER, *Ceramurg. Int.* **6** (1980) 43.
176. J. HEINRICH, D. MUNZ and G. ZIEGLER, *Powder Met. Int.* **14** (1982) 153.
177. D. BRUCKLACHER and W. DIENST, *J. Nucl. Mater.* **42** (1972) 285.
178. G. ZIEGLER and R. ZIEGLER, *Special Ceram.* 7 (1981) 133.
179. *Idem, Microstruct. Sci.* **9** (1981) 92.
180. G. ZIEGLER and J. HEINRICH, *Ceramurg. Int.* **6** (1980) 25.
181. G. ZIEGLER, in "Engineering with Ceramics", edited by R. W. Davidge (British Ceramic Society, Shelton, Stoke-on-Trent, 1982) pp. 213–25.

Received 2 July
and accepted 9 September 1986